Supporting Information

Fluorescence Modulation of Pyridinium Betaines: A Mechanofluorochromic Investigation

Peter W. McDonald, Jingjing Xu, Dale R. Lonsdale, Isabelle Jones, Benjamin Poggi, Rosalind P. Cox, Stéphane Aloise, Andrew D. Scully, Clémence Allain, Laurence Bodelot, Stephen A. Moggach, Toby D. M. Bell, Rémi Métivier, Sebastian G. B. Furness, Lars Goerigk, and Chris Ritchie*

Dr. P. W. McDonald, Dr. R. P. Cox, Assoc. Prof. T. D. M. Bell, Dr. C. Ritchie
School of Chemistry, Monash University, Wellington Road, 3800, Australia
*E-mail: chris.ritchie@monash.edu

Dr. J. Xu
College of Chemistry and Materials Science, Shanghai Normal University, Shanghai 200234, China

Dr. D. R. Lonsdale, Assoc. Prof. L. Goerigk
School of Chemistry, The University of Melbourne, 3010, Australia

Dr. I. Jones, Prof. S. A. Moggach
School of Molecular Sciences, University of Western Australia, 6009, Australia

Dr. B. Poggi, Dr. C. Allain, Dr. R. Métivier
Université Paris-Saclay, ENS Paris-Saclay, CNRS, PPSM, 91190, Gifsur-Yvette, France

Dr. S. Aloise
Université de Lille, CNRS, UMR 8516 – LASIRE – Laboratoire de Spectroscopie pour les Interactions, la réactivité et l'Environnement, Lille F-59000, France.

Dr. A. D. Scully
CSIRO Manufacturing, Research Way, Clayton, Victoria, 3168, Australia

Dr. L. Bodelot
LMS, CNRS, École Polytechnique, Institut Polytechnique de Paris, Route de Saclay, 91128, Palaiseau Cedex, France

Dr. S. G. B. Furness
School of Biomedical Sciences, Faculty of Medicine, The University of Queensland, St Lucia, 4067, Australia

Table of Contents

S1: Experimental section

Chemicals:

Acetonitrile (Merck gradient grade), 4-amino-2-methylpyridine (Sigma-Aldrich 97%), 4-aminopyridine (Sigma-Aldrich 98%), bromobenzene (Sigma-Aldrich reagent plus), chloroform (Merck ACS grade), dichloromethane (Merck), diethyl ether (Merck ACS grade), ethyl acetate (Ajax), n-hexane (Merck gradient grade), magnesium sulphate anhydrous (Merck), methanol (Ajax), octafluorocyclopentene (Tokyo Chemical Industry), tetrahydrofuran (Ajax), toluene (Merck gradient grade). All reagents were used as received unless otherwise stated. Bromobenzene was dried using 3 Å sieves.

Synthesis and Characterisation:

Chemicals were used as purchased without further purification. Solvents were degassed and dried over 3 Å molecular sieves where required (noted in individual syntheses), using standard laboratory procedures. Reactions were carried out under a nitrogen atmosphere where noted.

Synthesis of 1: The precursor N,N-diphenylpyridin-4-amine was prepared using a procedure adapted from literature.[1]

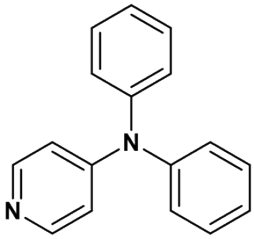

A solution of 4-aminopyridine (1.00 g, 10.63 mmol), CuI (300 mg, 1.57 mmol), K_2CO_3 (2.80 g, 20.26 mmol), and 18-crown-6 (360 mg, 1.36 mmol) in dry bromobenzene (25 mL) was stirred under a nitrogen atmosphere at 150 °C for 64 h. The reaction mixture was allowed to cool to r.t. and worked up with saturated NH_4Cl solution (~140 mL) and extracted with diethyl ether (3 × 50 mL). The combined organic phases were dried over $MgSO_4$, concentrated *in vacuo* and the resulting crude was purified by silica gel flash chromatography (R_f 0.36 in 9:1, petroleum

benzine/EtOAc; petroleum benzine/EtOAc, gradient 0-30% ethyl acetate, product elutes in 20%) to afford the product as a colourless powder (1.925 g, 74%):

mp 116.1-117.1 °C; ^{1}H NMR (600 MHz, $CDCl_3$, δ): 8.23 (d, *J* = 4.7 Hz, 2H, Ar H), 7.41 – 7.30 (m, 4H, Ar H), 7.23 – 7.15 (m, 6H, Ar H), 6.74 (d, *J* = 4.7 Hz, 2H, Ar H); ^{13}C NMR (151 MHz, $CDCl_3$, δ): 154.01, 149.78, 145.19, 129.95, 126.80, 125.81, 112.76; FT-IR (neat): υ_{max} 3087, 3026, 2650, 2477, 2372, 2323, 2112, 1874, 1659, 1628, 1574, 1546, 1482, 1451, 1425, 1336, 1304, 1265, 1238, 1217, 1188, 1167, 1074, 1025, 987, 942, 904, 837, 811, 775, 758, 736, 720, 706 cm^{-1}; HRMS (ESI-TOF) *m/z* [(M + H)$^{+}$] calcd. for $C_{17}H_{15}N_2$, 247.1230; found 247.1230. Anal. calcd for $C_{17}H_{14}N_2$: C 82.90, H 5.73, N 11.37; found: C 82.91, H 5.81, N 11.11.[2]

Synthesis of 1a: 2-(4-(diphenylamino)XXXyridine-1-ium-1-yl)-4,4,5,5-tetrafluoro-3-oxocyclopent-1-en-1-olate.

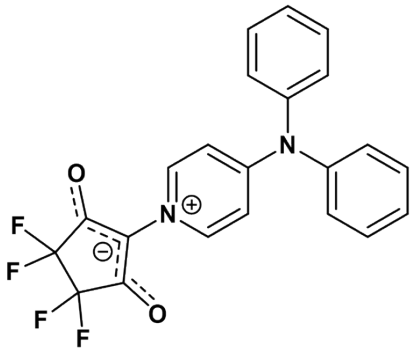

To a stirred solution of N,N-diphenylpyridin-4-amine (500 mg, 2.03 mmol) in THF (4 mL) at 0 °C was added octafluorocyclopentene (4.8 mL of a 0.745 M solution in THF, 3.58 mmol). After stirring at 0 °C for 1 h, water (1 mL) was added dropwise and the resulting solution was allowed to warm to r.t. and stirred overnight. The reaction mixture was quenched with water (~15 mL) and solid Na_2CO_3 and extracted with EtOAc (4 × 10 mL). The combined organic phases were washed with brine (2 x 20mL), dried over $MgSO_4$, concentrated *in vacuo* and the resulting crude was purified by flash chromatography (R_f 0.28 in 1:1, n-hexane/EtOAc; n-hexane/EtOAc, gradient 1:1 to 100% EtOAc) to afford the product as a pale yellow solid (710 mg, 84%):

mp 296.8 – 297.7 °C; ^{1}H NMR (400 MHz, $CDCl_3$, δ): 8.78 (d, *J* = 7.9 Hz, 2H, Ar H), 7.60 – 7.48 (m, 4H, Ar H), 7.49 – 7.39 (m, 2H, Ar H), 7.32 – 7.26 (m, 4H, Ar H), 6.86 (d, *J* = 8.0 Hz, 2H, Ar H); ^{13}C NMR (151 MHz, $CDCl_3$, δ): 173.83, 155.91, 141.86, 140.73, 131.09, 129.19, 126.92, 114.89,

111.48, 110.69, 109.74, 107.99; ^{19}F NMR (376 MHz, $CDCl_3$, δ): -127.02; FT-IR (neat): υ_{max} 3083, 3055, 2961, 2924, 2854, 2606, 2423, 2370, 2113, 1736, 1708, 1669, 1638, 1613, 1595, 1513, 1489, 1455, 1426, 1394, 1335, 1319, 1284, 1260, 1214, 1186, 1166, 1111, 1091, 1059, 1028, 1015, 1005, 959, 947, 934, 911, 849, 834, 775, 755, 720, 703, 691, 660 cm^{-1}; ; UV-Vis (THF): λ_{max} (ε) = 353 nm (25900 L mol^{-1} cm^{-1}); Fl (THF): λ_{max} = 612 nm; HRMS (ESI-TOF) *m/z* [(M + H)$^+$] calcd. for $C_{22}H_{15}F_4N_2O_2$, 415.1070; found 415.1071. Anal. calcd for $C_{22}H_{14}F_4N_2O_2$: C 63.77, H 3.41, N 6.76; found: C 63.26, H 3.20, N 7.19.

Synthesis of 2: 2-methyl-N,N-diphenylpyridin-4-amine was prepared using a procedure adapted from literature.[1]

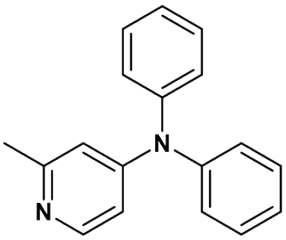

A solution of 4-amino-2-methylpyridine (934 mg, 8.64 mmol), CuI (264 mg, 1.39 mmol), K_2CO_3 (2.24 g, 16.2 mmol), and 18-crown-6 (284 mg, 1.07 mmol) in dry bromobenzene (20 mL) was stirred under a nitrogen atmosphere at 150 °C for 48 h. The reaction mixture was allowed to cool to r.t. and worked up with saturated NH_4Cl solution (50 mL) and extracted with diethyl ether (2 × 60 mL). The combined organic phases were washed with brine (3 × 40 mL), dried over $MgSO_4$, concentrated *in vacuo* (with remaining bromobenzene taken off at 50 °C and 15 mbar). The resulting crude was purified by flash chromatography (R_f 0.36 in EtOAc; EtOAc/MeOH, gradient 100% EtOAc to 8% MeOH) to afford the product as a light brown powder (697 mg, 31%):

mp 132.4-133.6 °C; ^{1}H NMR (600 MHz, $CDCl_3$, δ): 8.13 (d, *J* = 5.9 Hz, 1H, Ar H), 7.39 – 7.31 (m, 4H, Ar H), 7.22 – 7.15 (m, 6H, Ar H), 6.61 (d, *J* = 2.4 Hz, 1H, Ar H), 6.57 (dd, *J* = 5.9, 2.4 Hz, 1H, Ar H), 2.39 (s, 3H, CH_3); ^{13}C NMR (151 MHz, $CDCl_3$, δ): 158.75, 154.45, 149.31, 145.52, 129.87, 126.81, 125.58, 112.14, 110.71, 24.57; FT-IR (neat): υ_{max} 3055, 3033, 3009, 2924, 2854, 2374, 2345, 2113, 1871, 1720, 1638, 1603, 1580, 1552, 1480, 1450, 1421, 1377, 1341, 1310, 1294, 1267, 1236, 1219, 1180, 1171, 1155, 1108, 1075, 1025, 989, 967, 904, 862, 835, 818, 757, 731, 705 cm^{-1};

HRMS (ESI-TOF) *m/z* [(M + H)$^+$] calcd. for $C_{18}H_{17}N_2$, 261.1386; found 261.1387. Anal. calcd for $C_{18}H_{16}N_2$: C 83.04, H 6.19, N 10.76; found: C 83.03, H 6.13, N 10.59.

Synthesis of 2a: 2-(4-(diphenylamino)-2-methylpyridin-1-ium-1-yl)-4,4,5,5-tetrafluoro-3-oxocyclopent-1-en-1-olate.

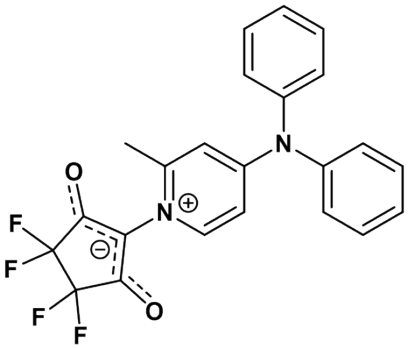

To a stirred solution of 2-methyl-N,N-diphenylpyridin-4-amine (329 mg, 1.26 mmol) in THF (2 mL) at 0 °C was added octafluorocyclopentene (2.54 mL of a 0.745 M solution in THF, 1.9 mmol). After stirring at 0 °C for 30 min, water (0.3 mL) was added dropwise and the resulting solution allowed to warm to r.t. and stirred overnight. The reaction mixture was quenched with water (3 mL) and solid Na_2CO_3 and extracted with EtOAc (3 × 10 mL). The combined organic phases were washed with brine (3 × 20 mL), dried over $MgSO_4$, concentrated *in vacuo* and the resulting crude was purified by flash chromatography (R_f 0.75 in EtOAc; n-hexane/EtOAc, gradient 100% n-hexane to 30% EtOAc) to afford the product as a pale yellow solid (200 mg, 54 %):

mp 215.0-221.2 °C; ^{1}H NMR (400 MHz; $CDCl_3$, δ): 7.69 (d, *J* = 7.4 Hz, 1H, Ar H), 7.58 – 7.48 (m, 4H, Ar H), 7.48 – 7.38 (m, 2H, Ar H), 7.34 – 7.24 (m, 4H, Ar H), 6.70 (dd, *J* = 7.4, 2.9 Hz, 1H, Ar H), 6.65 (d, *J* = 2.9 Hz, 1H, Ar H), 2.41 (s, 3H, CH_3); (151 MHz; $CDCl_3$, δ): 157.48, 154.82, 145.06, 141.91, 131.08, 129.15, 127.04, 111.26, 109.71, 20.13; ^{19}F NMR (376 MHz; $CDCl_3$, δ): -126.41 – -126.46 (m), -127.15 (s), -127.45 (s), -128.12 – -128.32 (m); UV-Vis (THF): λ_{max} (ε) = 326 nm (20300 L mol^{-1} cm^{-1}); Fl (THF): λ_{max} = 602 nm; FT-IR (neat): υ_{max} 3074, 3015, 2961, 2924, 2854, 2004, 1906, 1820, 1718, 1625, 1593, 1543, 1514, 1489, 1458, 1422, 1388, 1378, 1319, 1306, 1289, 1260, 1224, 1182, 1169, 1138, 1109, 1078, 1060, 1011, 851, 803, 766, 707, 696 cm^{-1}; HRMS (ESI-TOF) *m/z* [(M + H)$^+$] calcd. for $C_{24}H_{17}F_4N_2O_4$, 429.1226; found 429.1228. Anal. calcd for $C_{24}H_{16}F_4N_2O_4$: C 64.49, H 3.76, N 6.54; found: C 64.43, H 3.73, N 6.51.

FT-IR Spectroscopy:

FT-IR spectroscopy was performed on an Agilent Cary 630 FTIR spectrometer. Samples were used neat. Signals are listed as wavenumbers (ν, cm^{-1}).

Elemental Analysis:

Elemental analysis was conducted by Dr Alasdair McKay using a Perkin Elmer 2400 Series II CHN Analyser. The detector was calibrated using Acetanilide on the day of use and each sample was collected in duplicate.

NMR Spectroscopy:

^{1}H, ^{13}C and ^{19}F NMR spectra were recorded at 298 K in chloroform-d_1, unless otherwise stated, on either a Bruker Avance III or Bruker Avance III nanobay NMR spectrometer equipped with a 9.4 T magnet and 5 mm BBFO probe, operating at 400 MHz (^{1}H), 377 MHz (^{19}F) and 101 MHz (^{13}C) or a Bruker Avance III NMR spectrometer equipped with a 14.1 T magnet and TCI cryoprobe, operating at 600 MHz (^{1}H) and 151 MHz (^{13}C). Chemical shifts (δ) are reported in ppm and were referenced to the residual solvent signals (^{1}H, ^{13}C). Bruker software, TopSpin 3.6.1 and Mnova 14.2.3 were used for data acquisition and processing.

Ambient Pressure Single-Crystal X-ray Diffraction:

Low-temperature (123 K) X-ray intensity data for **1** and **2** were collected using a Rigaku XtaLAB Synergy diffractometer fitted with a Hypix6000HE hybrid photon counting detector and CuKα (l = 1.54184 Å) radiation. Data were processed, using the proprietary diffractometer software package CrysAlis Pro v1.171.39.46.[3] The structure was solved by conventional methods and refined on F2 using full-matrix least-squares using the Olex2[4] (1.3.0) software suite. Non-hydrogen atoms were refined with anisotropic displacement parameters.

Single crystals of the as-synthesised **1a** and **2a** samples were collected at ambient conditions on a Rigaku Oxford Diffraction XtaLAB Synergy S diffractometer,[5] utilising Cu Kα radiation (λ = 1.54178 Å). Diffraction data were integrated, and absorption correction was applied using the CrysAlis Pro software. Crystal structures were solved using SHELXT[6] intrinsic phasing and refined against $|F^2|$ using ShelXL[7] through the Olex2 interface. All geometric and thermal parameters were refined freely. For **2a** a solvent mask was calculated in Olex2 and used to model 1/3rd of a DCM molecule per Asymmetric Unit.

High-Pressure Single-Crystal X-ray Diffraction:

The same single crystals collected under ambient pressure conditions were loaded into a Merrill-Bassett diamond anvil cell (DAC)[8] with a 40° half-opening angle, comprised of two 600μm culet Boehlar Almax diamond anvils seated on tungsten carbide backing discs.[9] The sample crystals and a single ruby crystal were suspended in MiTeGen LVCO-5 Cryo Oil™ as the hydrostatic media within a pre-indented tungsten gasket loaded onto the DAC. CryoOil was selected as the pressure transmitting medium to minimise interaction with the framework, particularly in PM1-86 which contained pore-bound DCM solvent. The sample chamber pressures were measured by the ruby fluorescence method[10] on an OceanOptics spectrometer.

The diffraction data were collected using Mo Kα radiation (λ = 0.7107 Å) on a Rigaku Oxford Diffraction XtaLAB Synergy S diffractometer[1] equipped with a Hypix 6000HE detector. The pressure was increased incrementally up to 2.4 GPa and allowed to equilibrate overnight between each data collection. The data collection strategy was optimised by CrysAlis Pro[2] in a pre-experiment across a ϕ scan range from -10 – 10° and 170 – 190°. A cell opening angle cut-off mask was set at 38° to remove reflections with poor correlations from partially shaded areas. Reflections from the gasket were removed from the diffraction data before integration. A multi-scan absorption correction was applied using SADABS.[11]

The crystal structures were solved using the atomic coordinates refined from the ambient pressure structures. Structural refinements were carried out in the Olex2 against $|F^2|$ using SHELXL. Phenyl and pyridine rings were constrained using rigid fragments. The 5-membered enolate ring was constrained by a rigid fragment produced from the ambient structure. Hydrogen atoms were refined geometrically and constrained to ride on their host atoms. All

torsion angles between rings were allowed to refine freely. Disordered DCM in **2a** was modelled using solvent mask utility in Olex2. Disordered fluorine atoms were modelled in two parts and refined isotropically.

Powder X-ray Diffraction:

Powder X-ray diffraction (PXRD) patterns were measured using a Bruker D8 Advance Eco Diffractometer with Cu Kα radiation (λ = 1.54050 Å), operated in the 2θ range from 5° to 55°. The diffractometer was equipped with a 1000 W Cu-anode X-ray source with Ni Kβ filter, vertical θ - 2θ goniometer, motorised divergence slits, and a LynxEye XE 1D energy discriminative strip detector. The Bruker Diffrac suite was used to control and process the data. Samples were mechanically ground by hand in an agate mortar of inner diameter 50 mm using a 17 mm diameter agate pestle for approximately 10 minutes. Due to the preparation method, the particle size distribution was uncontrolled.

Electron Diffraction:

Electron diffraction measurements were collected on a Rigaku XtaLAB Synergy-ED diffractometer comprising a JEOL 200kV electron source and equipped with a Rigaku Hy-Pix ED detector. The diffractometer was controlled using CrysAlis Pro software suite for ED, which also handles data reduction, scaling and structure solution. The samples consisted of irregular grains of random size that were previously ground in a mortar and pestle. Six data sets were collected on grains with diameter less than two micrometres. Samples were transferred to a 3 mm grid. Data sets were measured at 294 K with a wavelength of 0.0251 Å and a crystal to detector distance of 770 mm. Each data set took 6-9 minutes for collection. Structures were solved and refined using the standard SHELX programs within either the AutoChem or Olex2 interfaces. Accurate electron scattering factors were automatically added to the .ins files for solution and refinement. The merged structure was solved with SHELXT intrinsic phasing and refined against $|F^2|$ using SHELXL. Each grain provided data sufficient to solve the structure, however with low completeness and limited resolution. Merging five of the six data sets gave 96.2% completeness at 0.92 Å resolution and greater redundancy. A comparison of data processing statistics is given

in Table S12. The SHELX rigid-bond restraint (RIGU) was used with the default esds (0.004). Measurements were collected by Dr. Lee M. Daniels. Rigaku Americas Corporation.

UV-Vis Absorption Spectroscopy:

Solution-state absorbance spectra were collected on an Agilent Technologies Cary 60 UV-Vis spectrophotometer using Agilent Technologies standard quartz cuvettes of 1 cm pathlength. Baseline corrections were applied over the entire collected wavelength range.

Steady-state and Time-resolved Fluorescence Spectroscopy:

Emission and excitation spectra were collected using an Agilent Technologies Cary Eclipse Fluorescence Spectrometer with an Agilent Cary Eclipse Solid Sample Holder. Samples were mounted on a silica disk. Gated phosphorescence spectral measurements were collected in phosphorescence mode using a total decay time of 1 ms, a single excitation flash at either 300 (**1** and **2**) or 350 nm (**1a** and **2a**). The given decay time of the flash is a maximum of 0.1 ms. Therefore, a 0.1 ms delay time was set to avoid any excitation interference. Gate times between 0.1 and 0.5 ms were used. Excitation and emission slit widths were set to 10 nm. Data averaging times were set to either 0.01 or 0.1 s and data intervals either 1, 2 or 4 nm. Phosphorescence decays were fit to two exponentials using the Cary lifetime software package.

Photoluminescence quantum yield **(PLQY)** measurements were conducted using an Edinburgh Instruments FLSP920 luminescence spectrometer with a CW Xe lamp as the excitation source (excitation wavelength 350 nm), and with the powder sample sandwiched between two quartz plates and mounted in an integrating sphere.

Time-resolved fluorescence decay histograms were obtained using the method of time-correlated single-photon counting (TCSPC), with a confocal microscope on a previously described custom-built set-up.[12] Excitation was from a picosecond pulsed supercontinuum fiber laser (Fianium, SC 400-4-pp) providing ~40 ps pulses across the visible and near-infrared at 10 MHz repetition rate (16 ps resolution). The excitation wavelength was achieved using a 700 nm short-pass filter and 40 nm band pass filter centered at 420 nm (Chroma). The light was then passed

through a focusing lens through a 10 µm pinhole (Thorlabs) and then collimated. The excitation light was then directed through an inverted Olympus IX71 microscope onto the sample using a 20x N.A. air objective (Olympus). Emission from the sample was collected through the same objective, separated from the excitation light by a dichroic mirror (Chroma), passed through a 490 nm long-pass filter (Chroma), and then focused onto a fast responsive avalanche photodiode detector (APD, PicoQuant, t-SPAD). Photon emission times were recorded on a photon counting module (Picoquant, PicoHarp 300) with a start signal provided by a sync out from the excitation laser and a stop signal from the APD detector. No pinhole was used on the emission side. An instrument response function (IRF) recorded from light scattered by a blank coverslip) had a full-width half maximum of ~700-800 ps. Fluorescence decay times were obtained by fitting the data with exponential decay functions convolved with the IRF using an iterative least-squares routine based on the Levenberg-Marquardt algorithm. Goodness-of-fit was determined from the chi-squared (χ^2) fitting parameter and by inspection of the distribution of the residuals. Decay curves and fit functions are given in the supporting information below.

Thermogravimetric Analysis:

TGA was conducted on a Mettler Toledo TGA thermogravimetric analyser, heating from 25 – 800 °C at a ramp rate of 10 °C min^{-1} under a 30 mL min^{-1} flow of nitrogen.

Differential Scanning Calorimetry:

DSC experiments were performed on a TA instruments Q100 thermal analyser (V9.9 Build 303) with a standard cell at a ramp rate of 10 °C min^{-1}. Three complete heating and cooling cycles were performed, with a 1-minute isothermal between each cycle. Aluminum pans were crimped.

Mass Spectrometry:

MS experiments were performed by the School of Chemistry at Monash University, Clayton on an Agilent Q-TOF 6540 mass spectrometer, using the electrospray technique and controlled via the MassHunter software package.

CrystalExplorer:

Finalised CIFs were inputted to the CrystalExplorer 17.5 program to calculate Hirshfeld surfaces and fingerprint plots using high resolution.[13] Interaction energies were calculated about a centrally selected molecule at the B3LYP/6-31G(d,p) level, scaled with benchmarked energy models.[14] A cluster of molecules within a radius of 3.8 Å was generated about the central molecule and all fragments were completed before the calculation of energies.

Computational Methods:

All density functional theory (DFT) and time-dependent DFT (TD-DFT) calculations were carried out with Gaussian 16 Rev.B01.[15] The ωB97X[16] functional was used in all cases, as it is a suitable compromise between accuracy and computational efficiency and the best hybrid functional to reasonably describe both local and charge-transfer transitions.[17] The Ahlrichs-type split-valence triple-ζ atomic-orbital basis set with one set of polarisation functions def2-TZVP[18] was used in all calculations. Self-consistent field and geometry convergence criteria were set to Gaussian's default.

Compression and Shearing Force Experiments:

Detailed methods are provided in section S13 in the supporting information.

Confocal Microscopy:

Data was collected using a Leica DMI 6000 SP8 SMD MP confocal microscope and analysed with the FLIM-fit software package. The setup contains a multiphoton laser source with 80 MHz synced pulse window (12.5 ns) and pulse width of 120 ps. An excitation source of 720 nm was used. Two channels were used with simultaneous dual emission collection mode, channel 1 with a 401-450 nm band pass and channel two with a 480-530 nm band pass. Pixel size is 114 nm x 114 nm and pixel dwell time is 0.7875 µs. Four line accumulations at a scan speed of 400 Hz (over 2048 x 2048) were undertaken to ensure enough photons for fitting to give a total dwell time of 3.15 µs. Each sample was measured in square regions of ~232.37 x 232.37 µm, which corresponds to 2048 x 2048 pixels.

S2: Crystallographic details

Table S1. Crystallographic details for compounds **1** and **2**.

	1	**2**
Empirical Formula	$C_{17}H_{14}N_2$	$C_{18}H_{16}N_2$
Formula Weight (g mol^{-1})	246.31	260.34
Crystal System	Orthorhombic	Monoclinic
Space Group	*Pbca*	$P2_1/n$
a (Å)	7.1760(1)	8.2492(1)
b (Å)	14.9090(2)	10.6153(1)
c (Å)	24.0607(3)	15.8197(2)
α (°)	90	90
β (°)	90	93.348(1)
γ (°)	90	90
Volume (Å^3)	2574.18(6)	1382.93(3)
Z	8	4
Z’	1	1
R_1 (%)	3.54	3.70
wR_2 (%)	9.10	9.74
R_{int} (%)	2.18	2.17

Table S2. Ambient SC-XRD and ED details for compounds **1a**.

	1a 294 K SC-XRD	**1a 294 K ED**
Empirical Formula	$C_{22}H_{14}N_2O_2F_4$	$C_{22}H_{14}N_2O_2F_4$
Formula Weight (g mol^{-1})	414.35	414.35
Crystal System	Monoclinic	Monoclinic
Space Group	$P2_1/n$	$P2_1/n$
a (Å)	15.2502(2)	15.6(3)
b (Å)	7.2351(1)	7.32(12)
c (Å)	17.1401(2)	17.46(16)
α (°)	90	90

β (°)	98.874(1)	99.1(4)
γ (°)	90	90
Volume (Å^3)	1868.54(4)	1969(53)
Z	4	4
Z’	1	1
R_1 (%)	5.62	15.46
wR_2 (%)	16.60	38.09
R_{int} (%)	3.96	22.18

Table S3. Ambient SC-XRD details for compounds **2a**.

	2a 296 K DCM SC-XRD	**2a 292 K Acetone SC-XRD**
Empirical Formula	$C_{23.33}H_{16.66}Cl_{0.66}N_2O_2F_4$	$C_{24.5}H_{19}N_2O_{2.5}F_4$
Formula Weight (g mol^{-1})	456.40	457.42
Crystal System	Monoclinic	Monoclinic
Space Group	*C*2/*c*	*C*2/*c*
a (Å)	23.3194(3)	23.4180(5)
b (Å)	10.7747(1)	10.7857(2)
c (Å)	18.0646(2)	18.1600(4)
α (°)	90	90
β (°)	108.968(1)	109.368(3)
γ (°)	90	90
Volume (Å^3)	4292.44(9)	4327.27(17)
Z	8	8
Z’	1	1
R_1 (%)	4.81	6.02
wR_2 (%)	13.61	18.10
R_{int} (%)	2.53	3.55

Optimised gas-phase structures

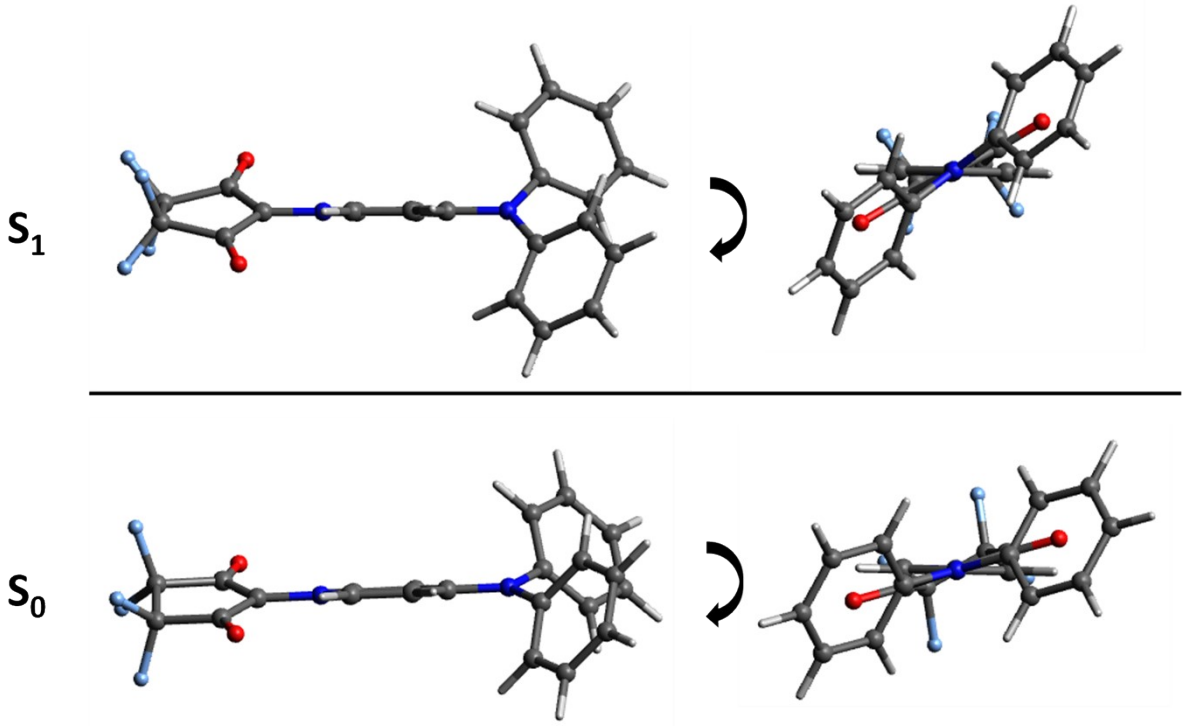

Figure S1. (TD)-ωB97X/def2-TZVP S_0 and S_1 optimised structures for **1a**.

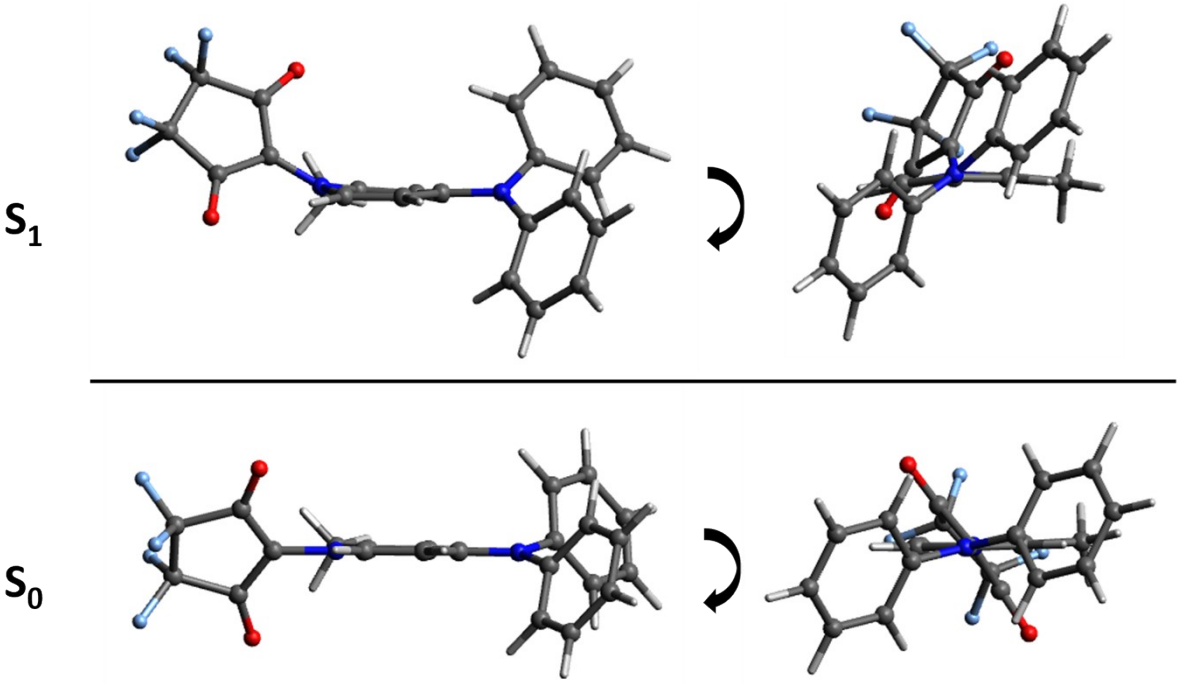

Figure S2. (TD)-ωB97X/def2-TZVP S_0 and S_1 optimised structures for **2a**.

S3: Hirshfeld surfaces, fingerprint plots and interaction energies

Fingerprint plots show that the closer to (0,0) the interactions get, the sharper the peaks become, as these are stronger/closer interactions. The interactions between the labelled elements, both inside and outside the Hirshfeld surface **(HS)**, make up a certain percentage of the surface area on the **HS**. These are indicated by the red and blue fragment patches on the surface and the section highlighted in blue on the fingerprint plot.

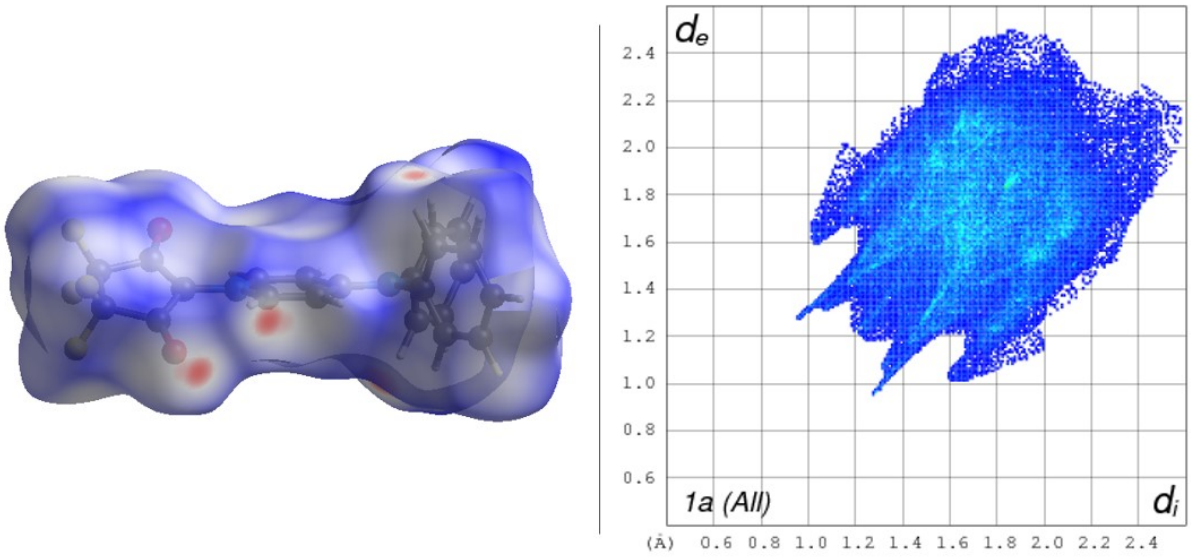

Figure S3. Hirshfeld surface and fingerprint plot showing all interactions for **1a**.

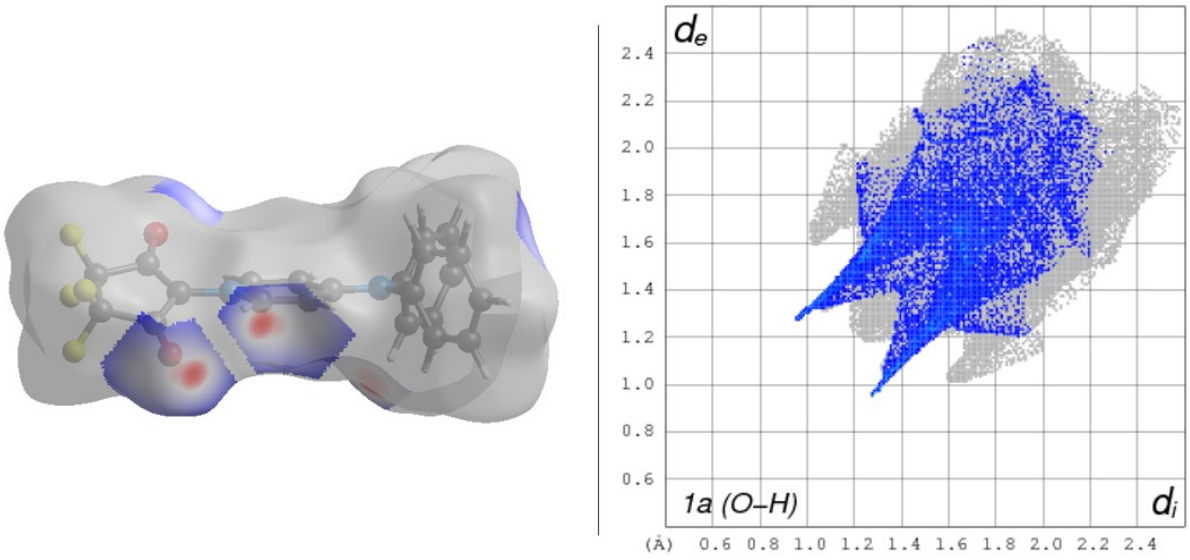

Figure S4. Hirshfeld surface and fingerprint plot for **1a**, showing 14.1% of the surface area is due to O --- H interactions.

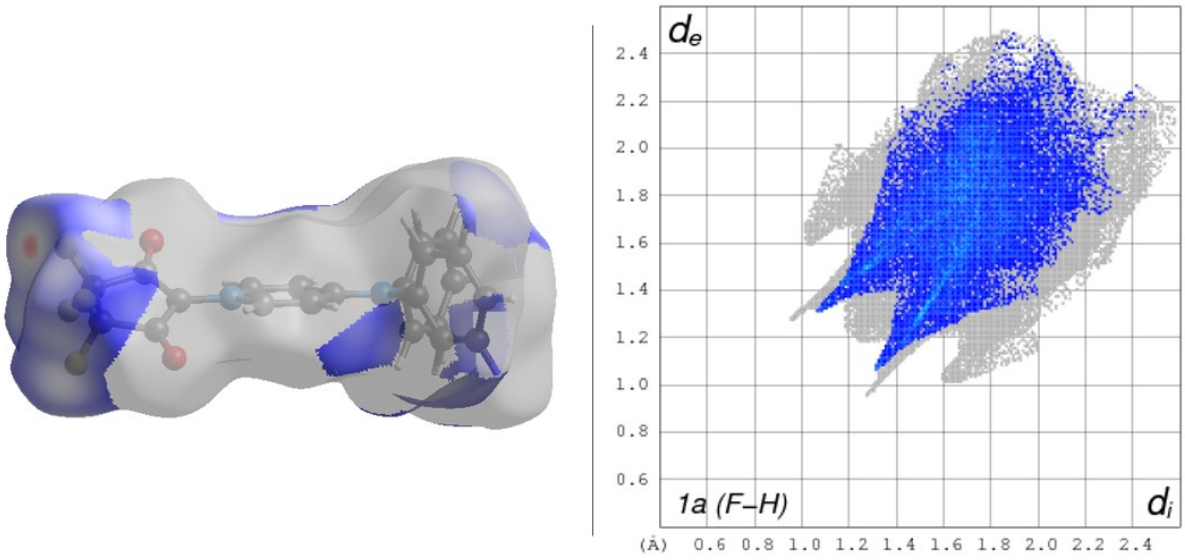

Figure S5. Hirshfeld surface and fingerprint plot for **1a**, showing 27.8% of the surface area is due to F --- H interactions.

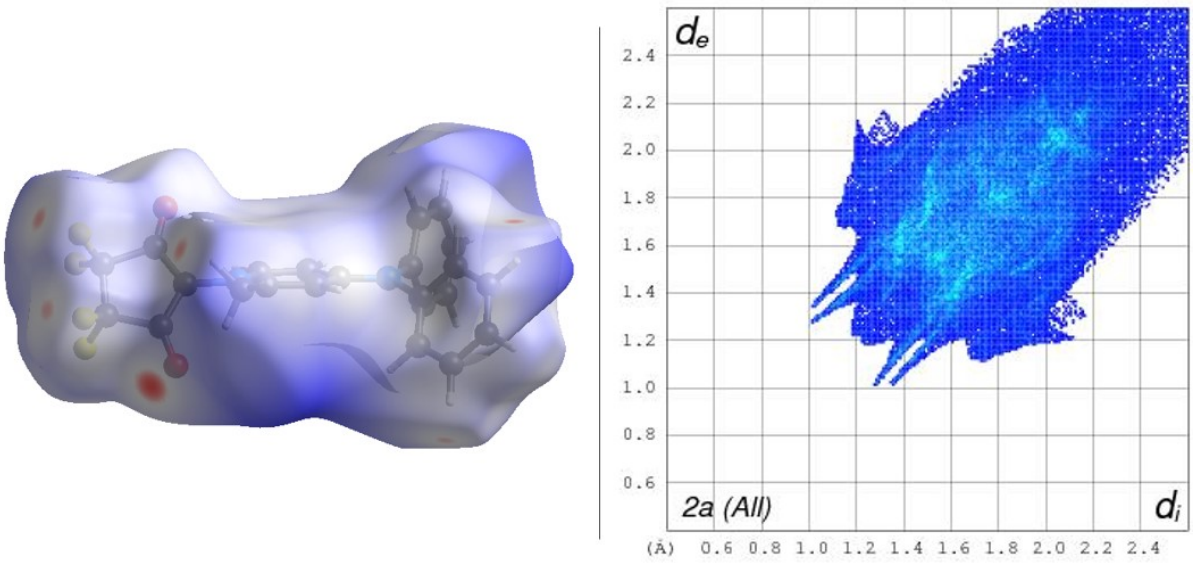

Figure S6. Hirshfeld surface and fingerprint plot showing all interactions for **2a**.

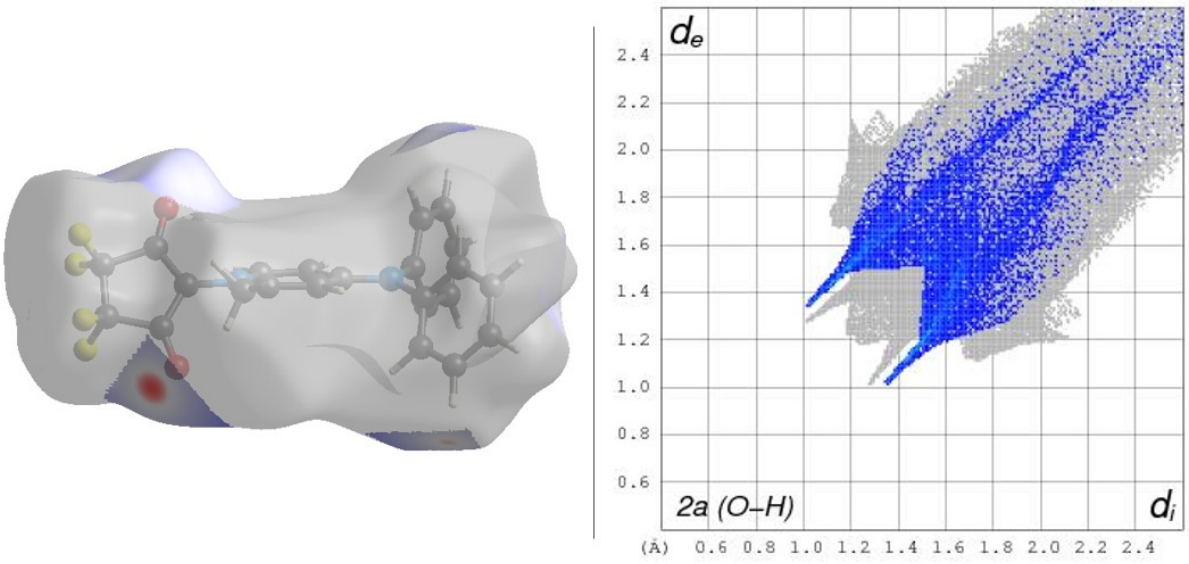

Figure S7. Hirshfeld surface and fingerprint plot for **2a**, showing 12.3% of the surface area is due to O --- H interactions.

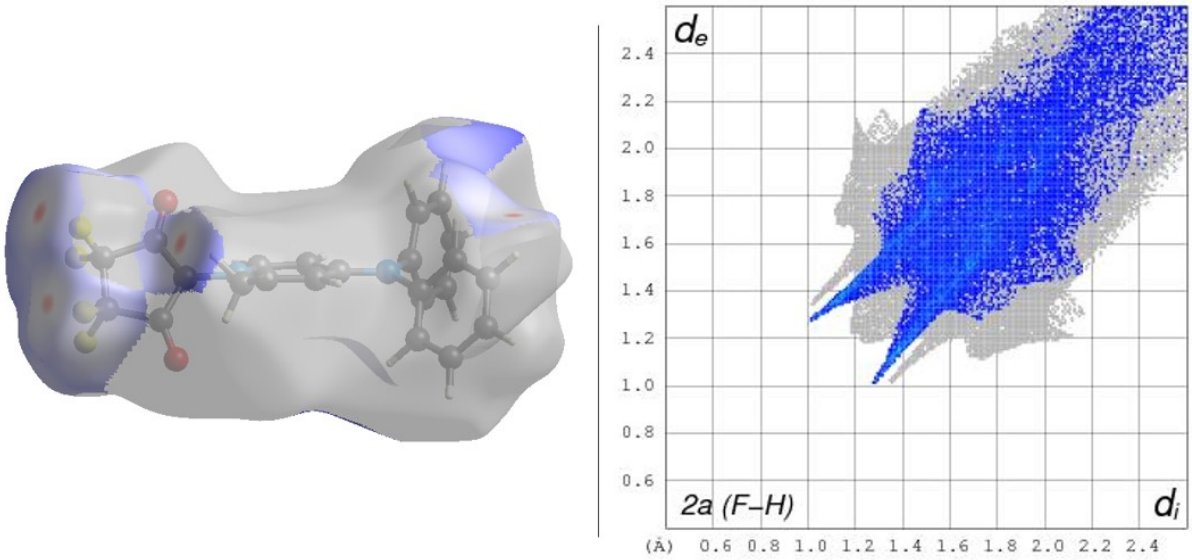

Figure S8. Hirshfeld surface and fingerprint plot for **2a**, showing 25.1% of the surface area is due to F --- H interactions.

S4: High-pressure crystallography studies

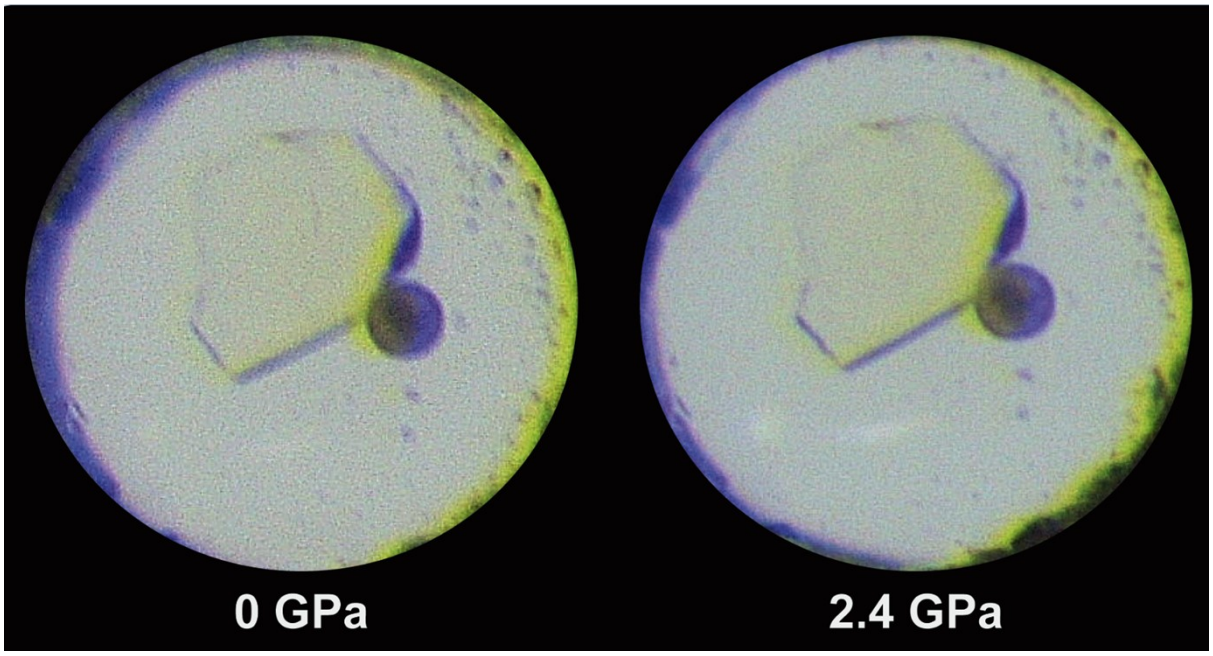

Figure S9. Optical images of **1a** suspended in MiTeGen LVCO-5 Cryo Oil^{TM} as the hydrostatic media at 0 GPa and 2.4 GPa in a DAC.

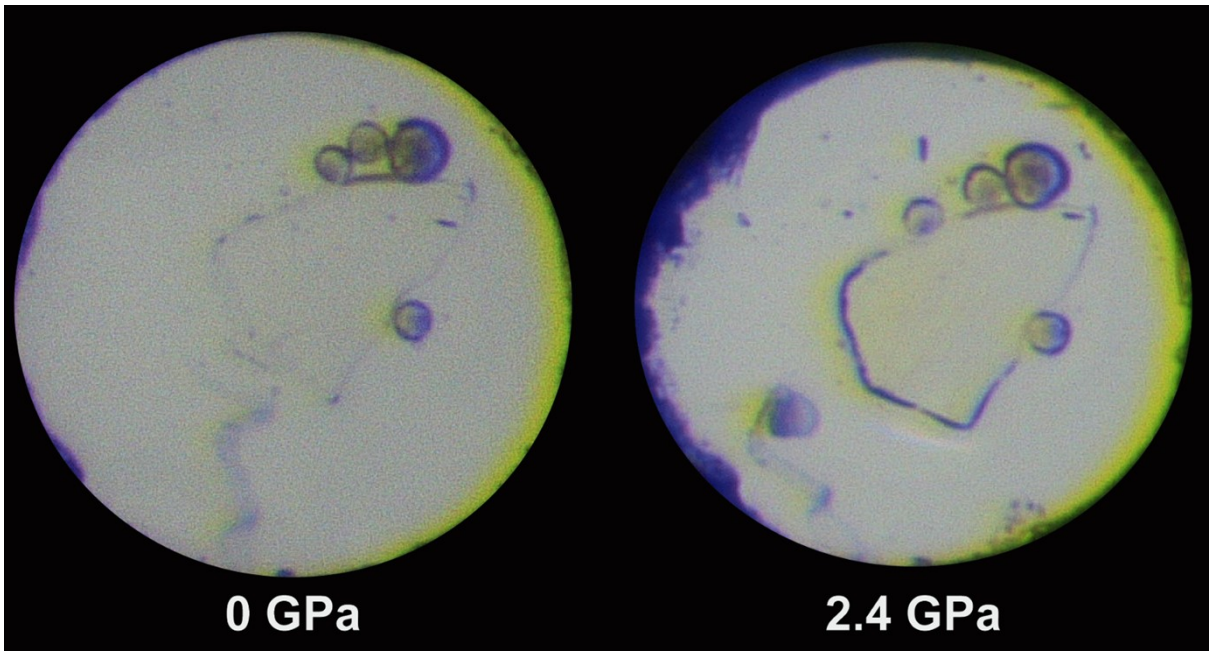

Figure S10. Optical images of **2a** suspended in MiTeGen LVCO-5 Cryo Oil^{TM} as the hydrostatic media at 0 GPa and 2.4 GPa in a DAC.

Table S4. Unit cell parameters under different isotropic pressure for **1a**.

Pressure **GPa**	Crystal system	Space group	Colour	Unit volume	a **Å**	b **Å**	c **Å**
Ambient	Monoclinic	$P2_1/n$	Clear, colourless	1868.54(4)	15.2502(2)	7.23510(10)	17.1401(2)
0.14	Monoclinic	$P2_1/n$	Clear, colourless	1832.9(5)	15.078(3)	7.1968(9)	17.0916(18)
0.3	Monoclinic	$P2_1/n$	Clear, colourless	1803.4(5)	14.947(3)	7.1595(9)	17.056(2)
0.45	Monoclinic	$P2_1/n$	Clear, colourless	1786.9(4)	14.898(3)	7.1340(7)	17.0206(16)
0.6	Monoclinic	$P2_1/n$	Clear, colourless	1746.1(6)	14.709(4)	7.0732(10)	16.998(2)
1.2	Monoclinic	$P2_1/n$	Clear, colourless	1718.9(4)	14.3730(3)	7.1198(8)	16.9803(16)
2.4	Monoclinic	$P2_1/n$	Clear, colourless	1626.4(6)	13.977(4)	7.0687(9)	16.677(2)
2.9	Monoclinic	$P2_1/n$	Clear, colourless	1592.6	13.899(5)	6.9946(14)	16.635(3)

Table S5. Unit cell angles for **1a**.

Pressure **GPa**	α	β	γ
0	90	98.8740(10)	90
0.14	90	98.785(14)	90
0.3	90	98.856(16)	90
0.45	90	98.964(13)	90
0.6	90	99.113(7)	90
1.2	90	98.425(11)	90
2.4	90	99.204(20)	90
2.9	90	100.01(2)	90

Table S6. Unit cell parameters under different isotropic pressure for **2a**.

Pressure **GPa**	Crystal system	Space group	Colour	Unit volume	a **Å**	b **Å**	c **Å**
Ambient	Monoclinic	$C2/c$	Clear, colourless	4292.44(9)	23.3194(3)	10.7747(10)	18.0646(2)
0.14	Monoclinic	$C2/c$	Clear, colourless	4181(3)	23.133(8)	10.672(2)	17.881(8)
0.3	Monoclinic	$C2/c$	Clear, colourless	4002(2)	22.939(7)	10.4739(18)	17.590(7)
1.2	Monoclinic	$C2/c$	Clear, colourless	3951(2)	22.717(6)	10.4456(12)	17.530(7)
2.4	Monoclinic	$C2/c$	Clear, colourless	3664(14)	22.082(4)	10.198(2)	16.997(3)

Table S7. Unit cell angles for **2a**.

Pressure **GPa**	α	β	γ
Ambient	90	108.9680(10)	90
0.14	90	108.72(5)	90
0.3	90	108.73(4)	90
1.2	90	108.21(4)	90
2.4	90	106.81(3)	90

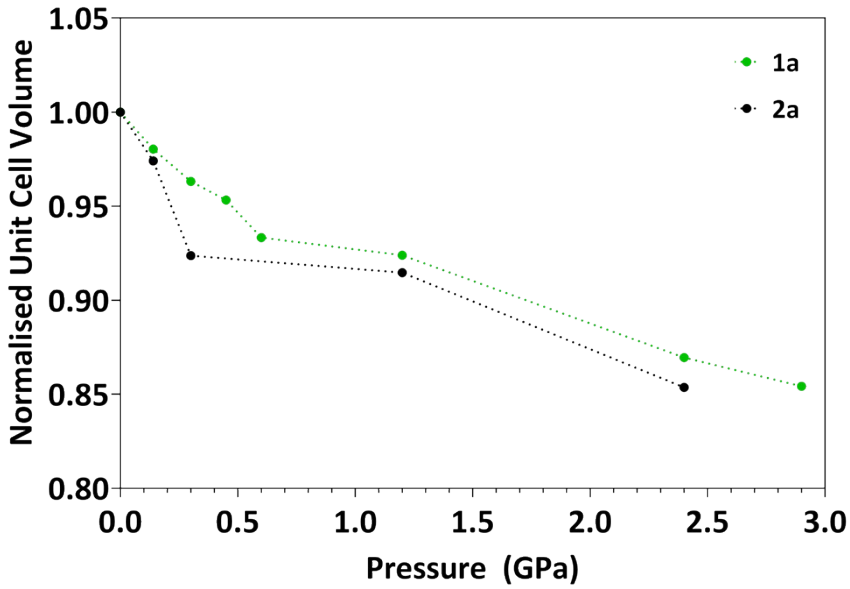

Figure S11. Cell volume reduction comparison as a function of increasing isotropic pressure for **1a** (green) and **2a** (black).

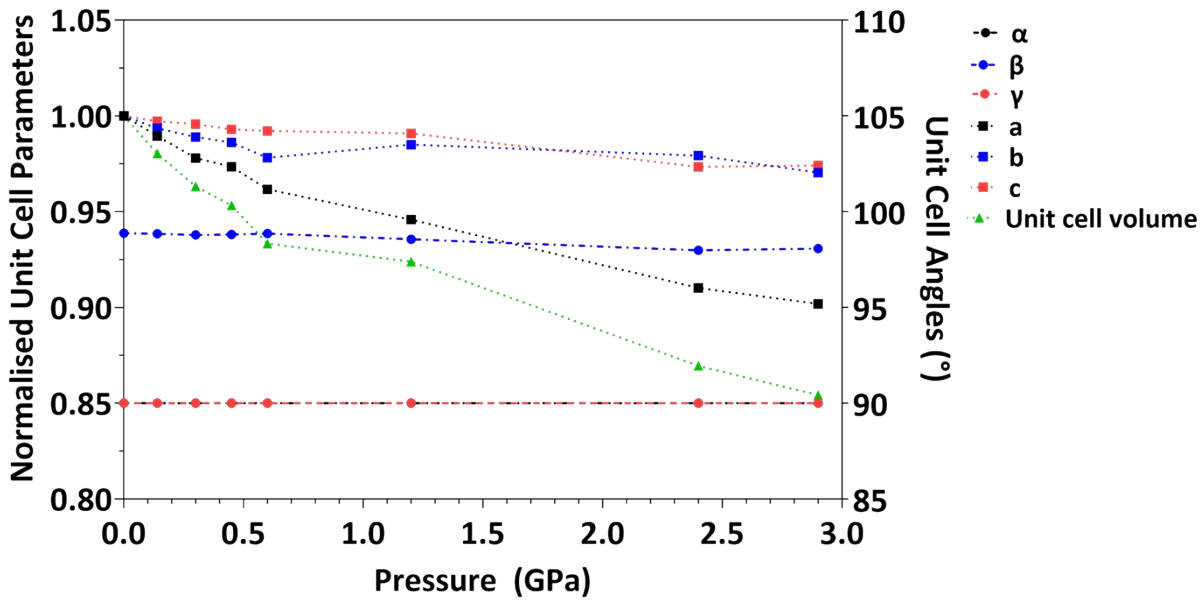

Figure S12. Unit cell changes with increasing isotropic pressure for **1a**.

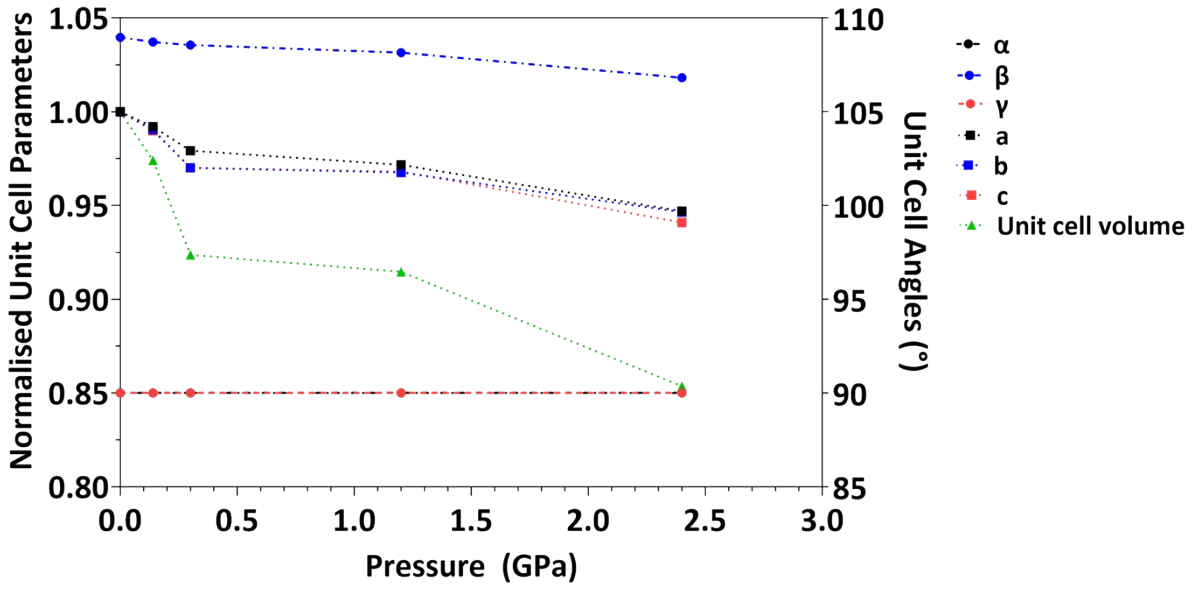

Figure S13. Unit cell changes with increasing isotropic pressure for **2a**.

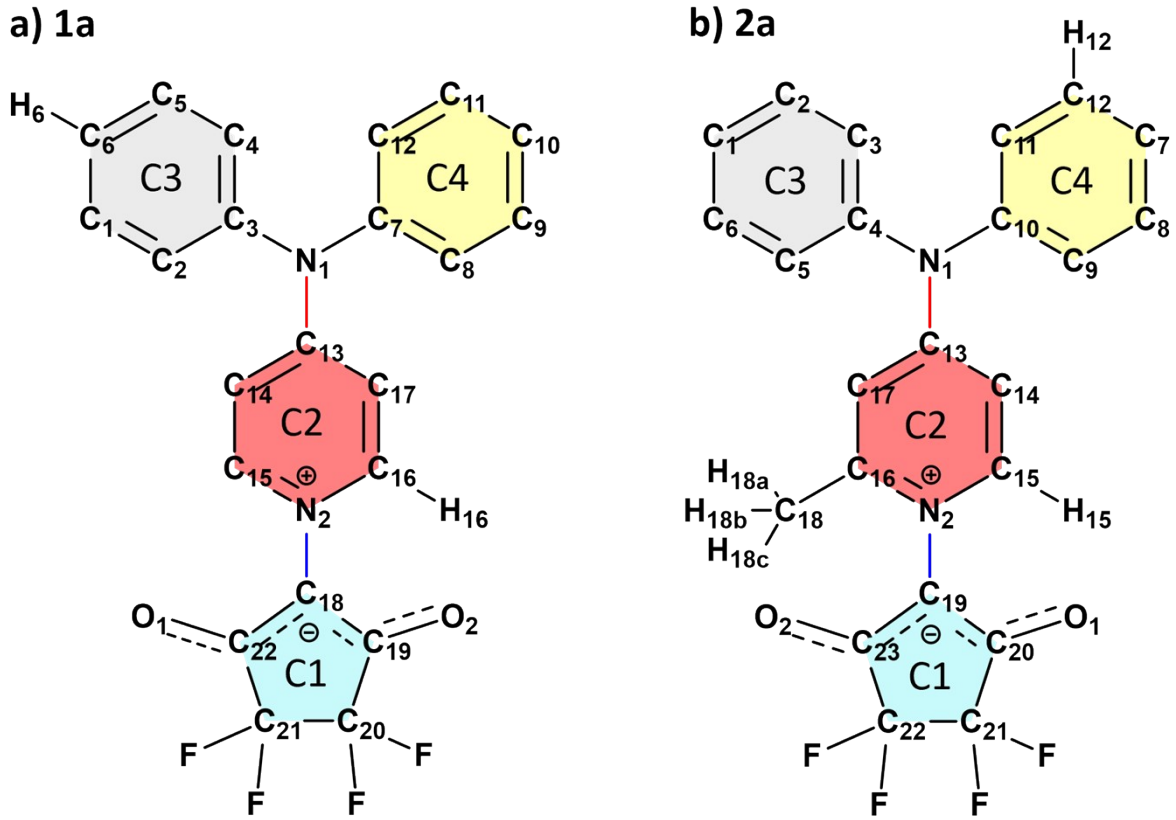

Figure S14. Full atom labels and ring planes (**C1** – light blue; **C2** – red; **C3** – grey and **C4** – yellow) used to define distances and torsion angles for a) **1a** and b) **2a**.

Table S8. Edge-on dimer bond lengths and interaction energies for **1a** at varying isotropic pressure.

Pressure **GPa**	O_2-H_{16} Distance **Å**	Dimer Energy **kJ·mol^{-1}**
Ambient	2.47	78.8
0.14	2.46	77.1
0.3	2.47	76.5
0.45	2.47	76.6
0.6	2.47	75.3
1.2	2.47	74.0
2.4	2.53	73.5
2.9	2.52	73.4

Table S9. Key bond lengths and interaction energies for **1a** at varying isotropic pressure.

Pressure **GPa**	C3-C3 Centroid **Å**	H_6-C4 Distance **Å**	Torsion Angle C_{15}-N_2-C_{18}-C_{22} **°**	Torsion Angle C_{16}-N_2-C_{18}-C_{19} **°**	Torsion Angle C_7-N_1-C_{13}-C_{17} **°**	Torsion Angle C_3-N_1-C_{13}-C_{14} **°**	PQPE Energy **kJ·mol^{-1}**
Ambient	4.07	2.70	-30.7(2)	-33.3(2)	-3.8(2)	-7.0(2)	35.9
0.14	4.04	2.67	-36.7(5)	-26.1(6)	-3.3(8)	-8.6(8)	38.4
0.3	4.02	2.63	-36.2(4)	-27.0(5)	-3.3(7)	-8.1(7)	40.6
0.45	4.00	2.61	-35.7(5)	-26.8(6)	-4.3(8)	-7.9(8)	41.6
0.6	3.96	2.55	-35.5(6)	-26.2(6)	-3.9(9)	-9.0(9)	45.1
1.2	3.95	2.54	-35.8(8)	-25.7(9)	-4.0(11)	-10.8(11)	45.8
2.4	3.84	2.40	-36.6(10)	-23.7(10)	-4.9(13)	-11.6(13)	53.5
2.9	3.74	2.35	-35.8(11)	-25.4(12)	-3.1(16)	-11.9(15)	57.4

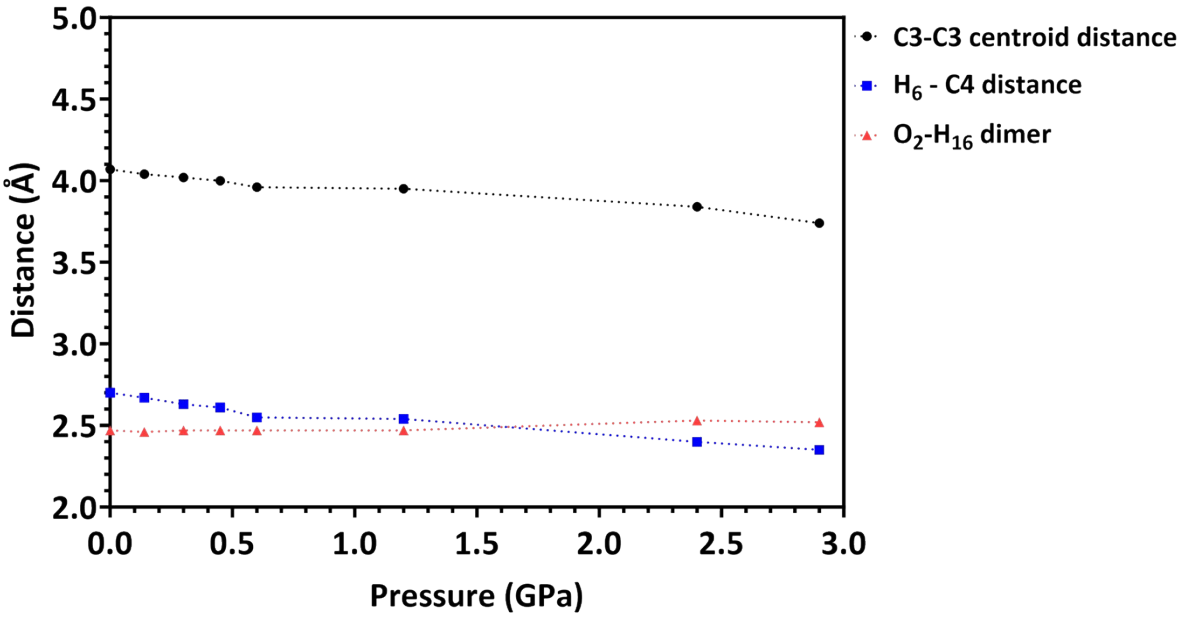

Figure S15. Key intermolecular distances as a function of increasing isotropic pressure for **1a**.

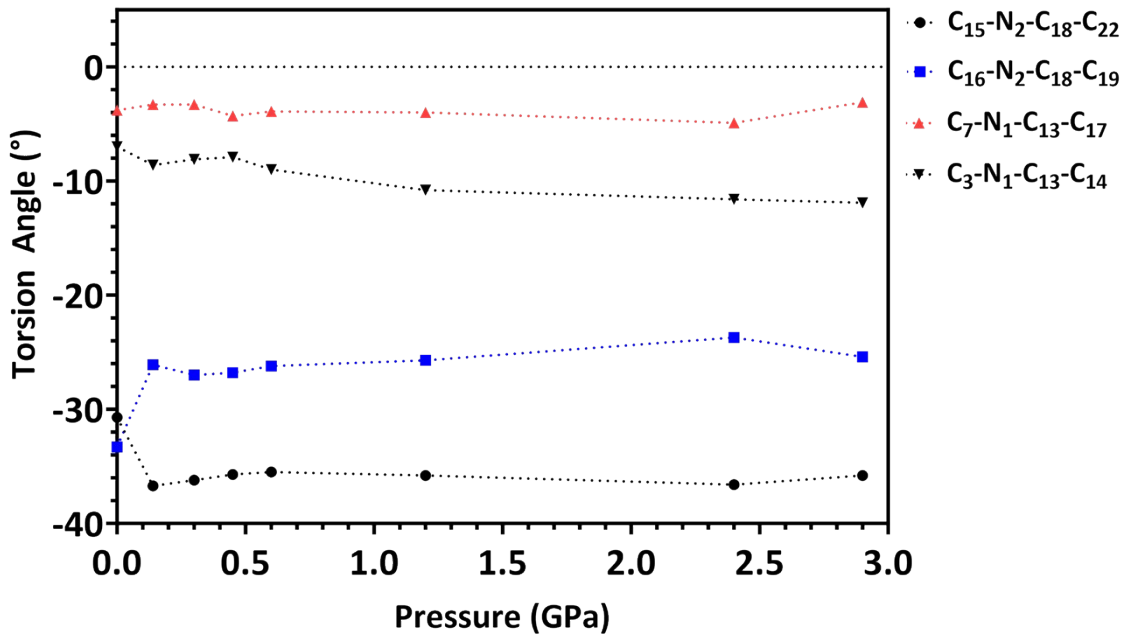

Figure S16. Torsion angles as a function of increasing isotropic pressure for **1a**.

Table S10. Stacked dimer bond lengths and interaction energies for **2a** at varying isotropic pressure.

Pressure **GPa**	O_2-H_{15} Distance **Å**	Dimer Energy **kJ·mol^{-1}**
Ambient	3.03	83.5
0.14	3.03	83.1
0.3	2.99	77.1
1.2	2.94	92.1

Table S11. Key bond lengths and interaction energies for **2a** at varying isotropic pressure.

Pressure **GPa**	C2-C3 Centroid **Å**	H_{18x}-C4 Distance **Å**	H_{12}-C3 Distance **Å**	Torsion Angle C_{15}-N_2-C_{19}-C_{20} °	Torsion Angle C_{16}-N_2-C_{19}-C_{23} °	Torsion Angle C_4-N_1-C_{13}-C_{17} °	Torsion Angle C_{10}-N_1-C_{13}-C_{14} °	PPyE Energy **kJ·mol^{-1}**
Ambient	3.93	2.97	2.99	-54.5(2)	-61.4(2)	16.0(2)	4.7(2)	47.6
0.14	3.88	3.04	2.99	-66.9(9)	-45.1(10)	15.4(14)	3.3(14)	53.4
0.3	3.76	2.85	2.91	-67.9(8)	-43.8(9)	16.4(13)	3.3(13)	58.0
1.2	3.73	2.92	2.89	-69.6(9)	-43.4(10)	16.4(16)	2.4(16)	57.9

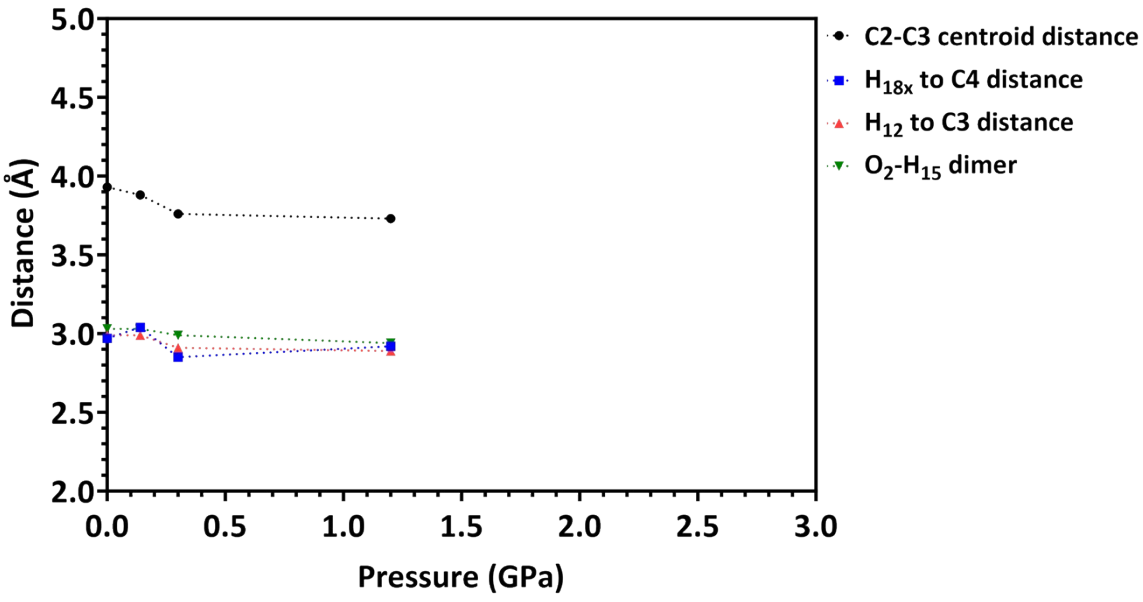

Figure S17. Key intermolecular distances as a function of increasing isotropic pressure for **2a**.

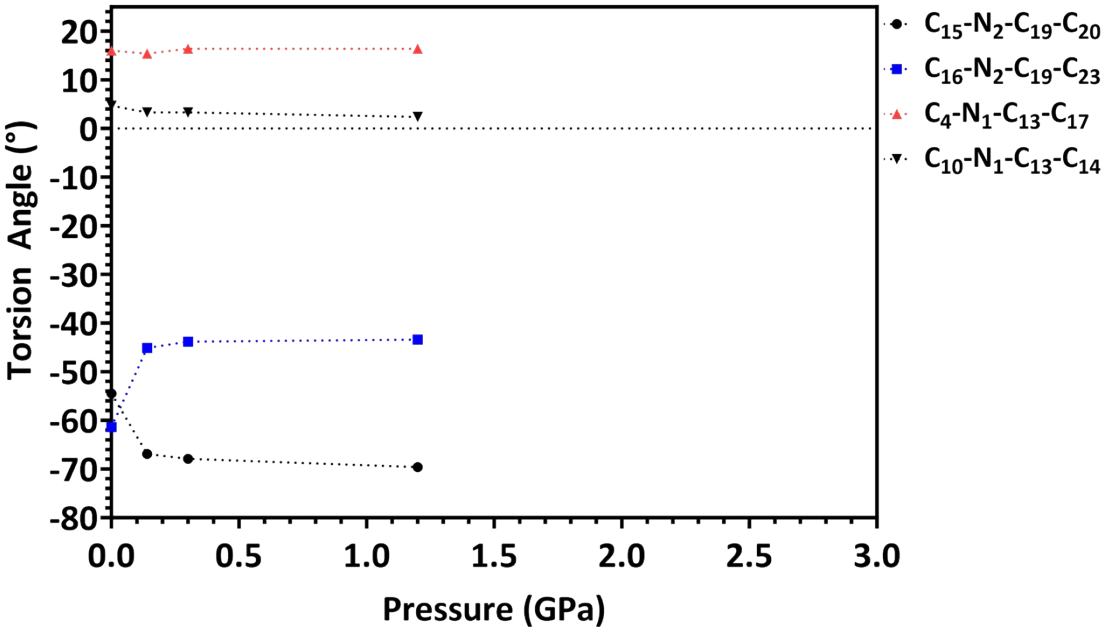

Figure S18. Torsion angles as a function of increasing isotropic pressure for **2a**.

S5: Electron diffraction

Table S12. Electron diffraction data processing statistics for **1a G**.

Data set	Resolution Å	Completeness %	Redundancy	$<F^2/\delta(F^2)>$ (last shell)	R_{int} (last shell) %	R_{pim} (last shell) %	$CC_{1/2}$ (last shell) %
1097	1.0	76.5	2.6	2.67 (0.93)	19.5 (62.4)	14.5 (48.6)	98.0 (31.2)
1098	1.0	76.6	3.0	3.05 (0.48)	19.7 (71.8)	13.7 (50.8)	98.5 (59.8)
1099	0.90	74.1	3.0	5.02 (1.33)	10.7 (54.9)	7.4 (39.1)	98.9 (48.2)
1100	1.0	79.3	3.1	3.69 (1.54)	14.8 (49.0)	10.2 (32.7)	99.0 (79.3)
1101	0.90	58.7	3.1	6.45 (1.44)	8.2 (52.0)	5.5 (36.3)	99.6 (46.5)
1102	0.90	70.3	2.3	1.68 (0.38)	22.6 (71.4)	18.9 (63.6)	98.4 (14.6)
1097-1101	0.90	90.9	9.3	6.50 (1.79)	21.2 (62.5)	6.6 (35.2)	98.3 (42.2)

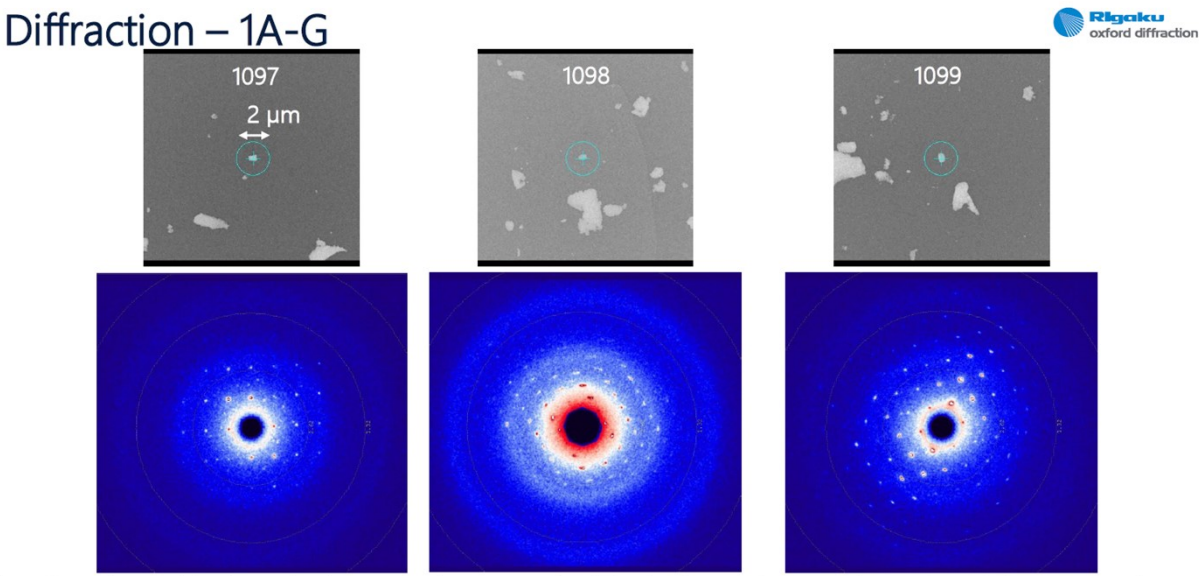

Figure S19. View of three grains used for electron diffraction data collection on **1a G** (top) and representative diffraction images (bottom). The two-micron circle represents the Selected Area (SA) aperture located behind the crystallite. Only the diffraction from the object within the SA aperture reaches the detector.

S6: Powder X-ray diffraction

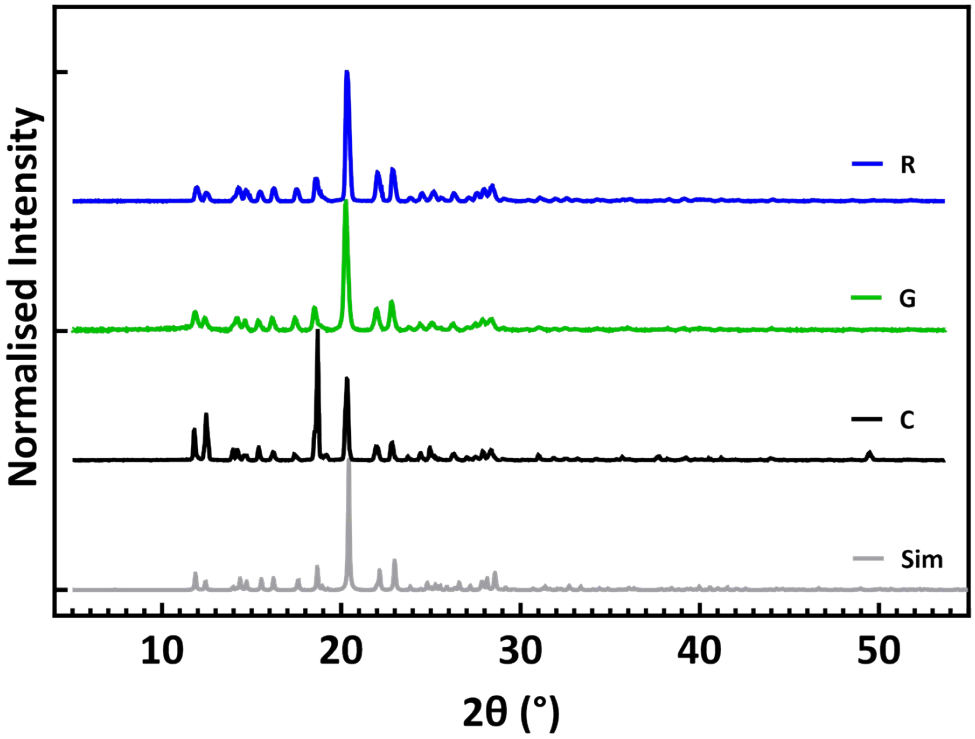

Figure S20. PXRD patterns for **1**.

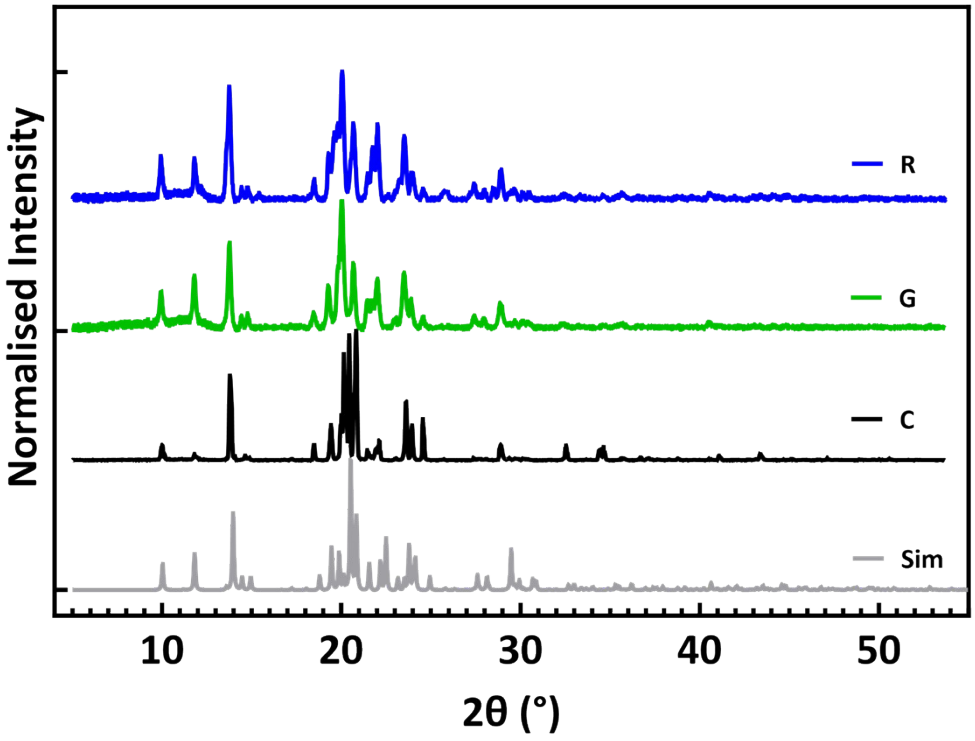

Figure S21. PXRD patterns for **2**.

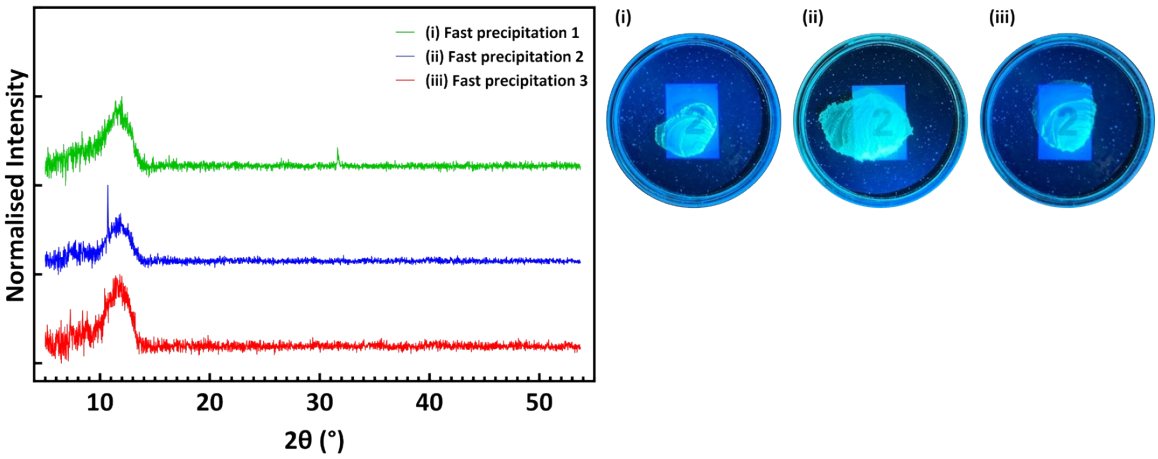

Figure S22. PXRD patterns for **2a** after fast precipitation from acetone.

S7: Solid-state absorption, excitation and emission spectra

C = crystalline powder

G = mechanically ground

R = ground samples reordered from acetone exposure

An = reordered samples annealed at 100 °C for 1 hour

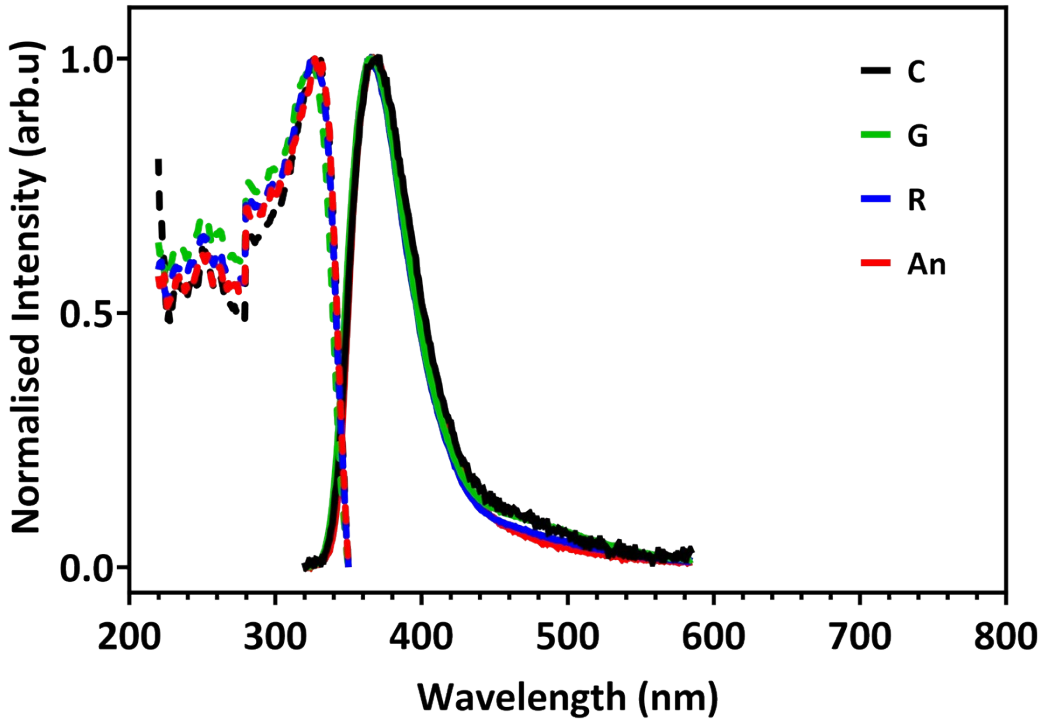

Figure S23. Solid-state excitation and emission spectra for **1**. All emission spectra were obtained with excitation at 300 nm, excitation spectra were recorded with emission detection at 370 nm.

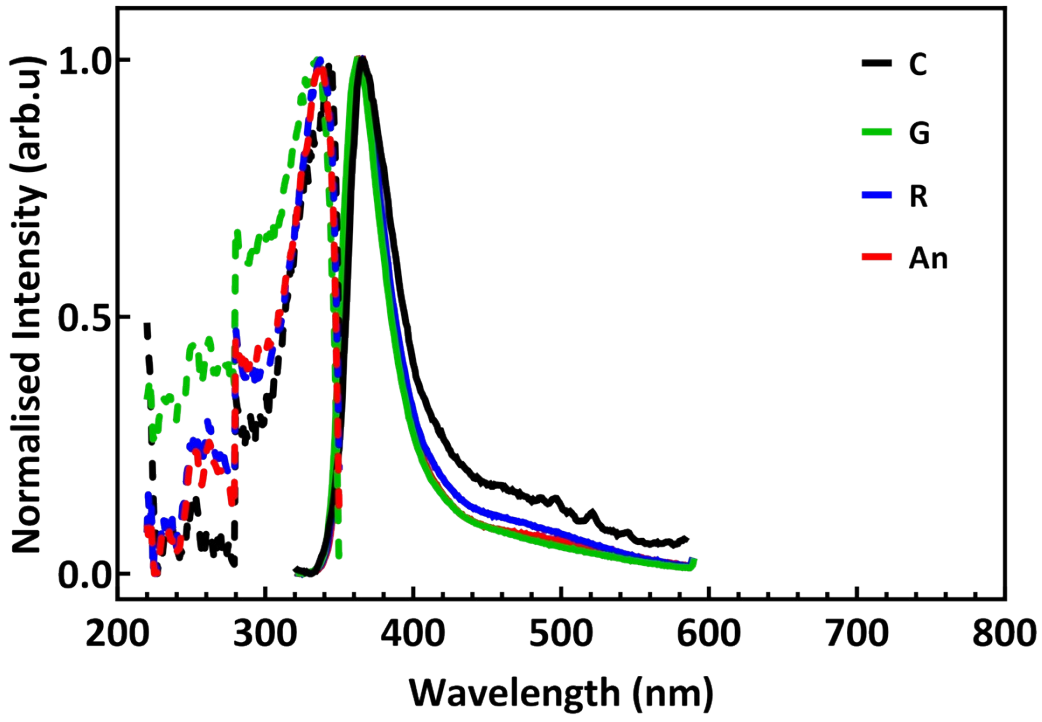

Figure S24. Solid-state excitation and emission spectra for **2**. All emission spectra were obtained with excitation at 300 nm, excitation spectra were recorded with emission detection at 370 nm.

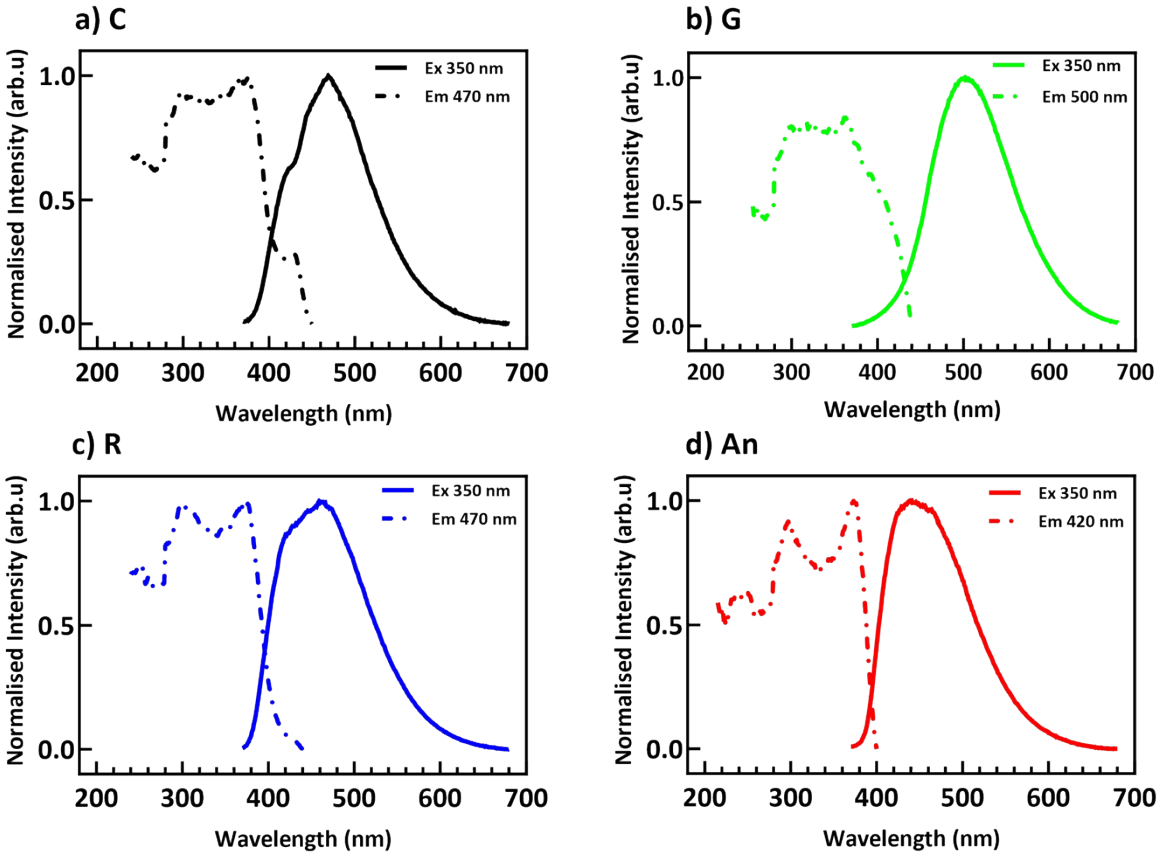

Figure S25. Overlay of excitation and emission spectra in the four forms studied for **1a**. All emission spectra were obtained with excitation at 350 nm, excitation spectra were recorded with emission detection at the maximum emission wavelength (indicated in graph legend) and cut below half the detection wavelength

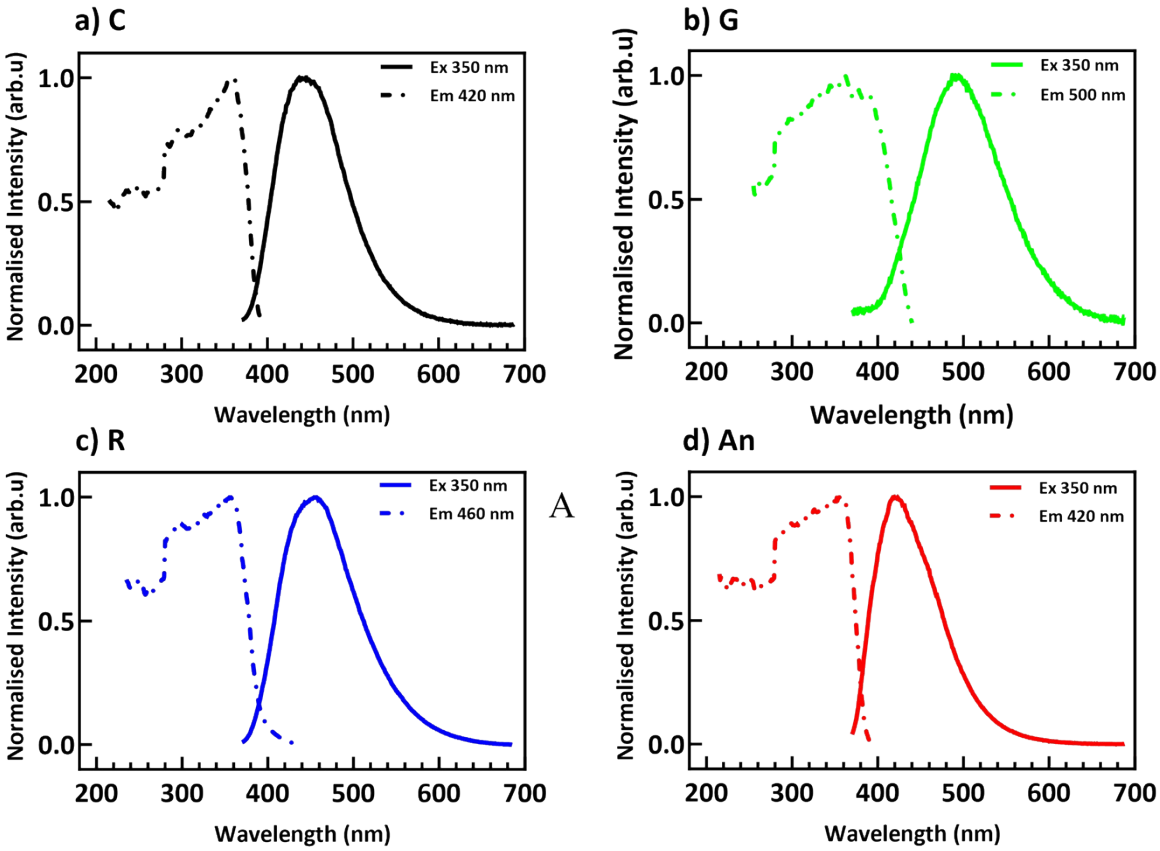

Figure S26. Overlay of excitation and emission spectra in the four forms studied for **2a**. All emission spectra were obtained with excitation at 350 nm, excitation spectra were recorded with emission detection at the maximum emission wavelength (indicated in graph legend) and cut below half the detection wavelength.

S8: Thermogravimetric analysis

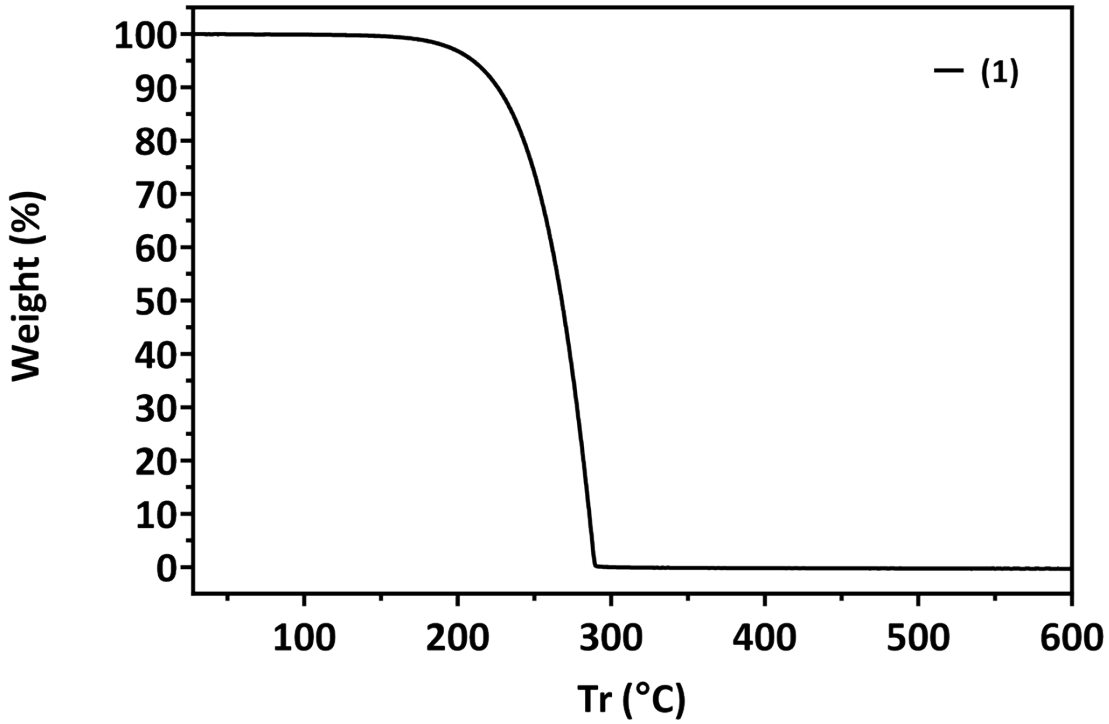

Figure S27. Thermogravimetric analysis for **1** with decomposition onset at 160 °C and complete degradation by 290 °C.

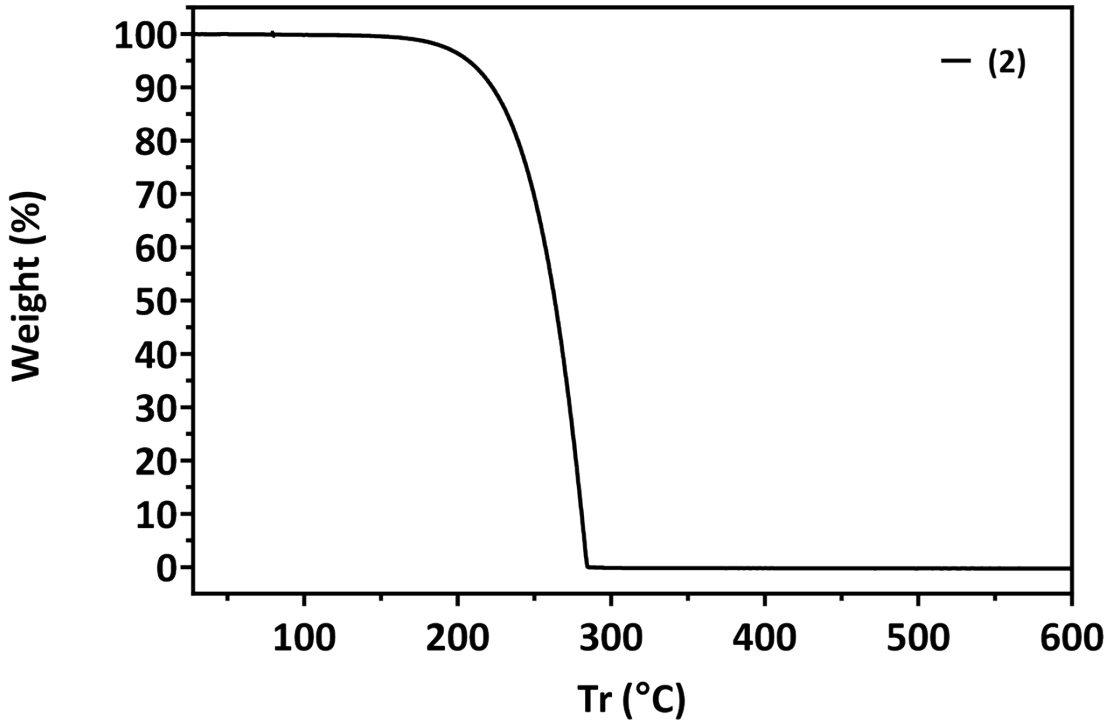

Figure S28. Thermogravimetric analysis for **2** with decomposition onset at 160 °C and complete degradation by 285 °C.

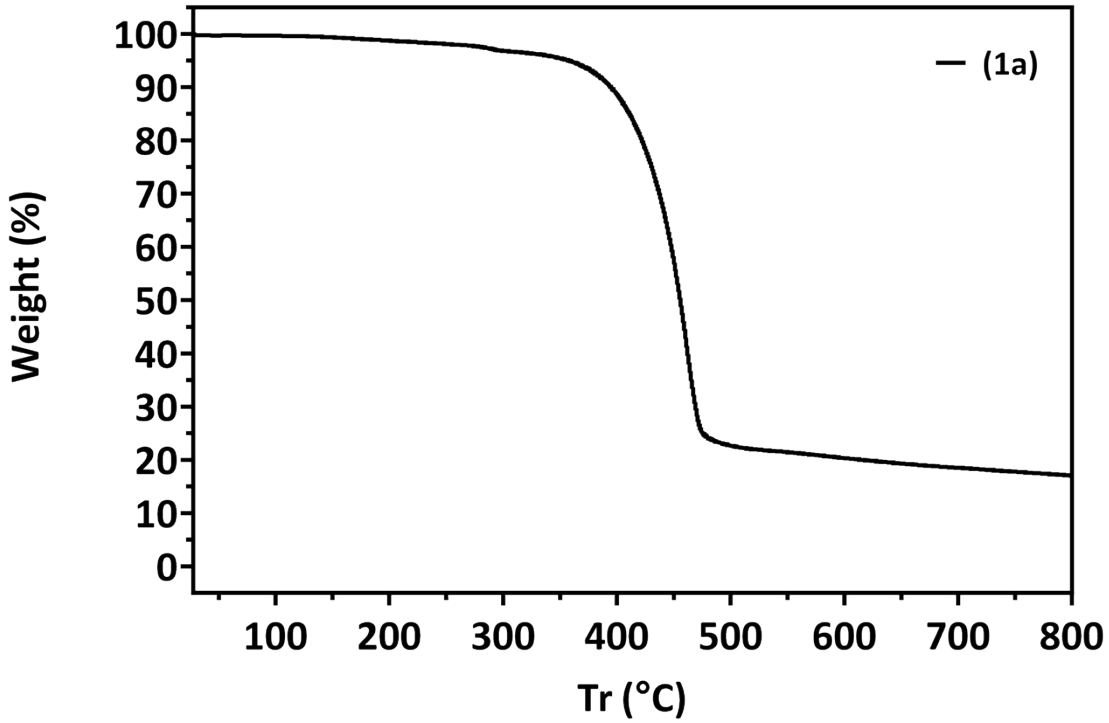

Figure S29. Thermogravimetric analysis of **1a** with decomposition commencing at 280 °C.

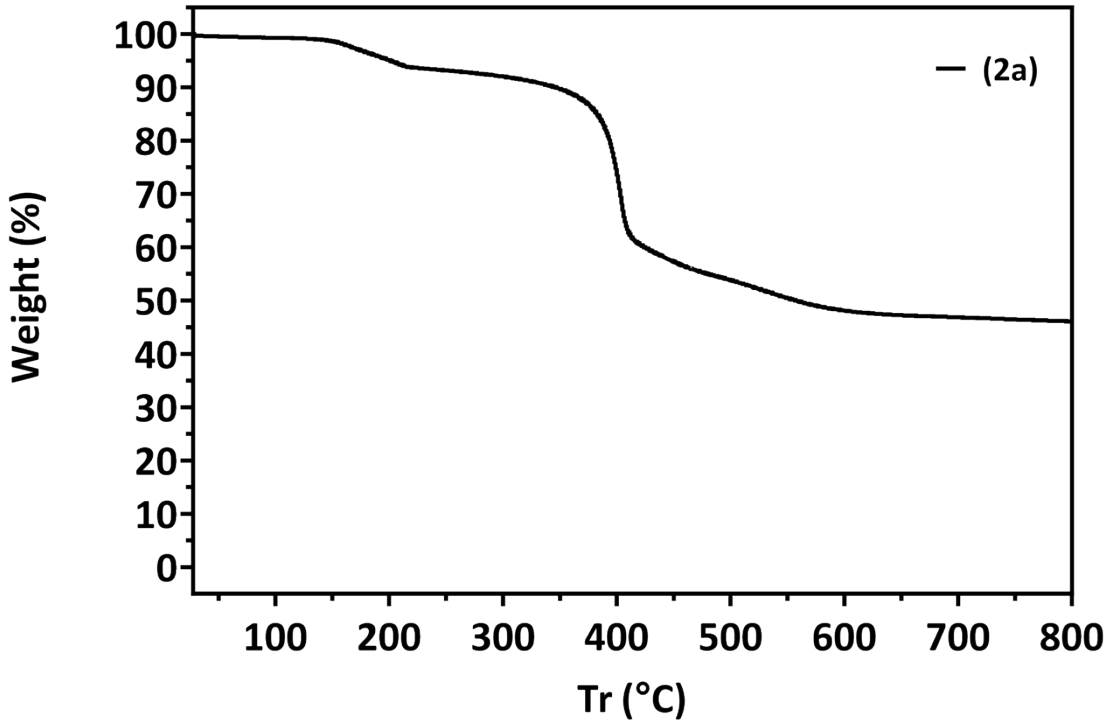

Figure S30. Thermogravimetric analysis of **2a** with mass loss of 6.1% (attributed to solvent loss of 1.5 water molecules per formula unit) from 25-215 °C and decomposition commencing at 280 °C.

S9: Differential scanning calorimetry

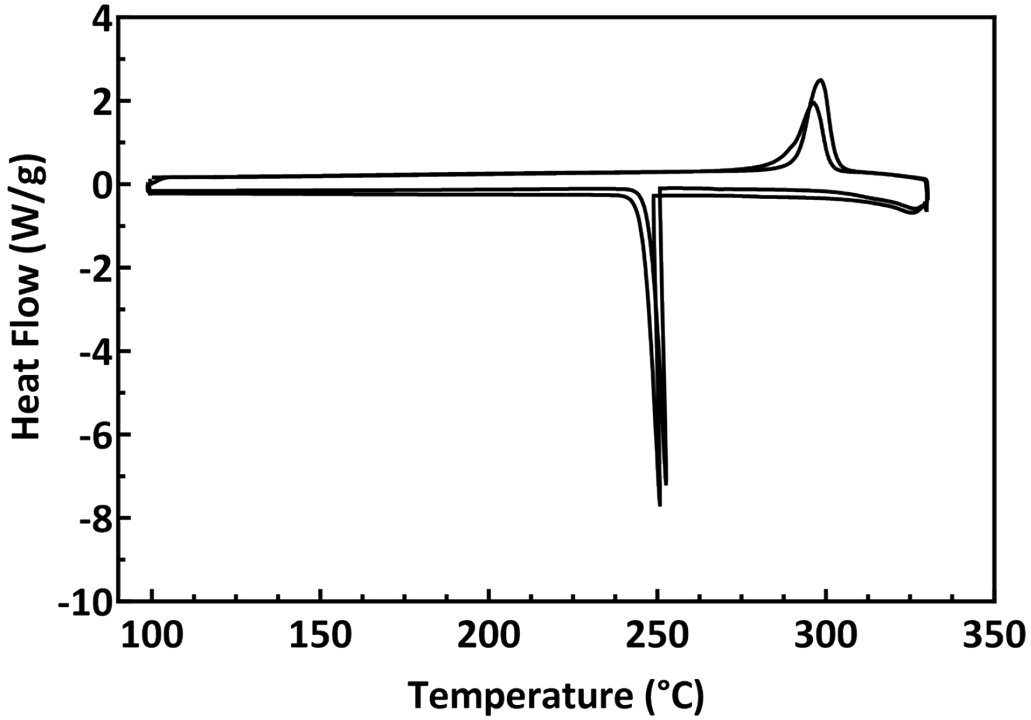

Figure S31. Differential scanning calorimetry scans of **1a**, showing a melting point peak at 298 °C (approximate enthalpy of fusion 100 J/g) and crystallisation peak between 250-260 °C (approximate enthalpy of 95 J/g). Three scan cycles are shown with exo down.

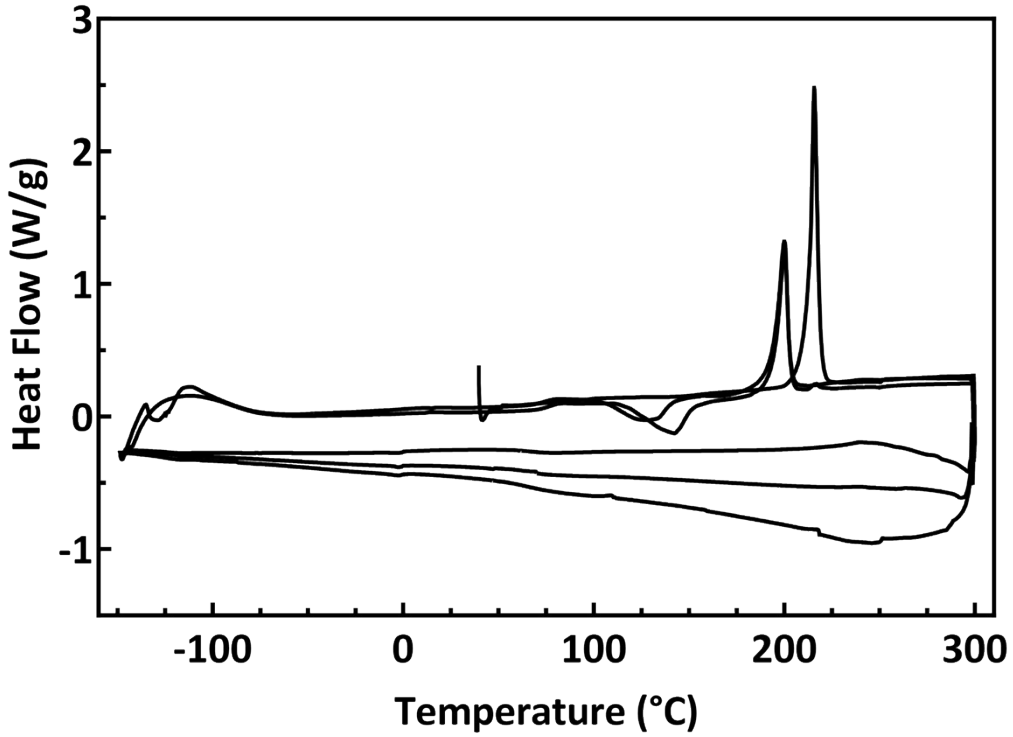

Figure S32. Differential scanning calorimetry scans of **2a**, showing an initial solvated melting point peak at 216 °C (enthalpy of 72.62 J/g), subsequent melting point peaks at 200 °C (approximate enthalpy of fusion 45 J/g) and phase transition peak between 125-145 °C (approximate enthalpy of 30 J/g). Three scan cycles are shown with exo down.

S10: Thermal reorganisation emission spectra

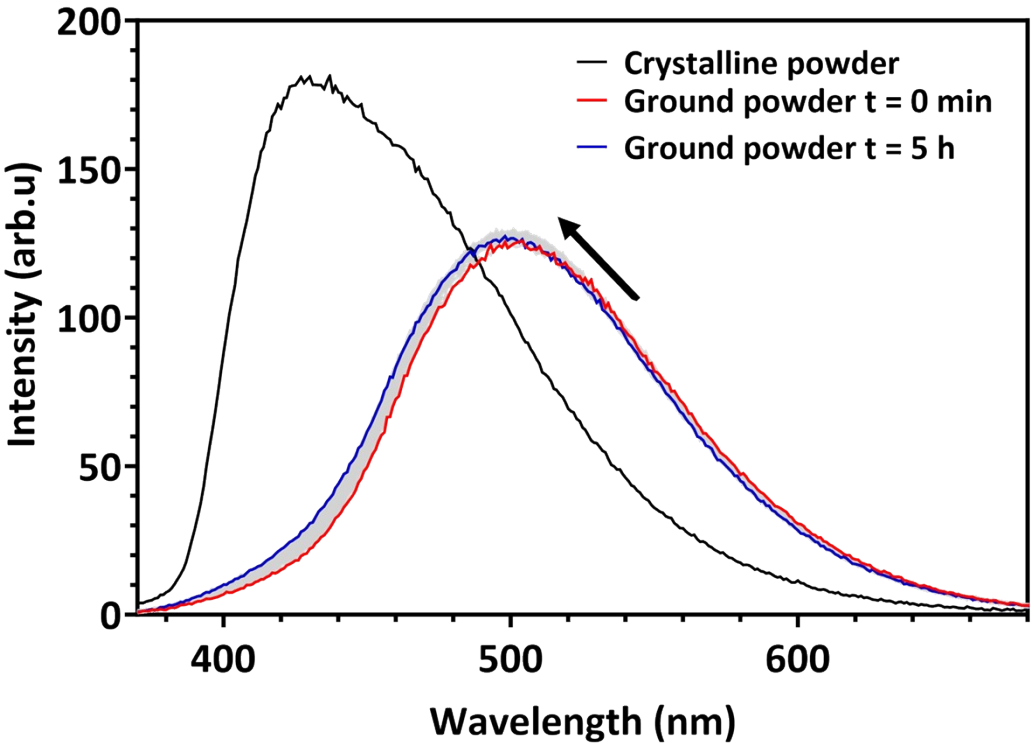

Figure S33. Reorganisation emission spectra for **1a** over 5 hours.

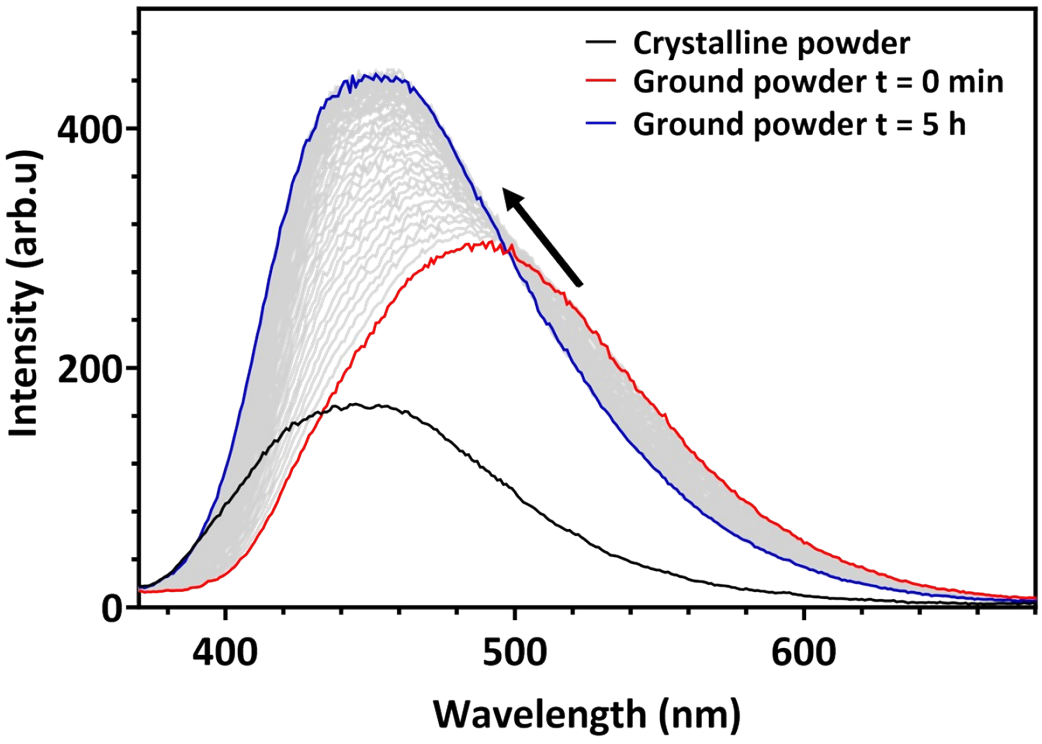

Figure S34. Reorganisation emission spectra for **2a** over 5 hours.

S11: Time-resolved fluorescence measurements (TCSPC)

Photoluminescence decays were fitted to the sum of two exponential terms.

$$I(t) = \sum_{i=1}^{n} p_i exp(-\frac{t}{\tau_i}),$$

where p_i and τ_i are the relative weights and lifetime of the i th component, respectively, and n is the total number of components.

The intensity weighted average lifetime was calculated by

$$\tau_{avg} = \sum_{i=1}^{n} p_i \tau_i^2 / \sum_{i=1}^{n} p_i \tau_i .$$

Table S13. Fluorescence lifetime fitting and photophysical parameters for **1a**.

State	λ_{max} **nm**	τ_1(%) **ns**	τ_2(%) **ns**	τ_{avg} **ns**	ϕ_{fl}	χ^2	k_r **(x10^{-8}) s^{-1}**	k_{nr} **(x10^{-8}) s^{-1}**	τ_{nat} **ns**
C	462	1.27(67)	4.72(33)	3.50	0.71	1.183	2.03	0.83	4.93
G	500	2.46(41)	5.76(59)	5.00	0.51	1.061	1.02	0.98	9.80
R	468	1.66(62)	4.74(38)	3.62	0.63	1.089	1.74	1.02	5.75
An	438	1.38(77)	4.23(23)	2.74	0.57	1.177	2.08	1.57	4.81

Table S14. Fluorescence lifetime fitting and photophysical parameters for **2a**.

State	λ_{max} **nm**	τ_1(%) **ns**	τ_2(%) **ns**	τ_{avg} **ns**	ϕ_{fl}	χ^2	k_r **(x10^{-8}) s^{-1}**	k_{nr} **(x10^{-8}) s^{-1}**	τ_{nat} **ns**
C	437	1.59(67)	4.96(33)	3.63	0.58	1.098	1.60	1.16	6.26
G	492	2.58(46)	6.73(54)	5.71	0.60	1.078	1.05	0.70	9.52
R	454	1.61(78)	5.55(21)	3.51	0.82	1.194	2.34	0.51	4.28
An	418	1.58(68)	4.91(32)	3.56	0.79	1.180	2.22	0.59	4.51

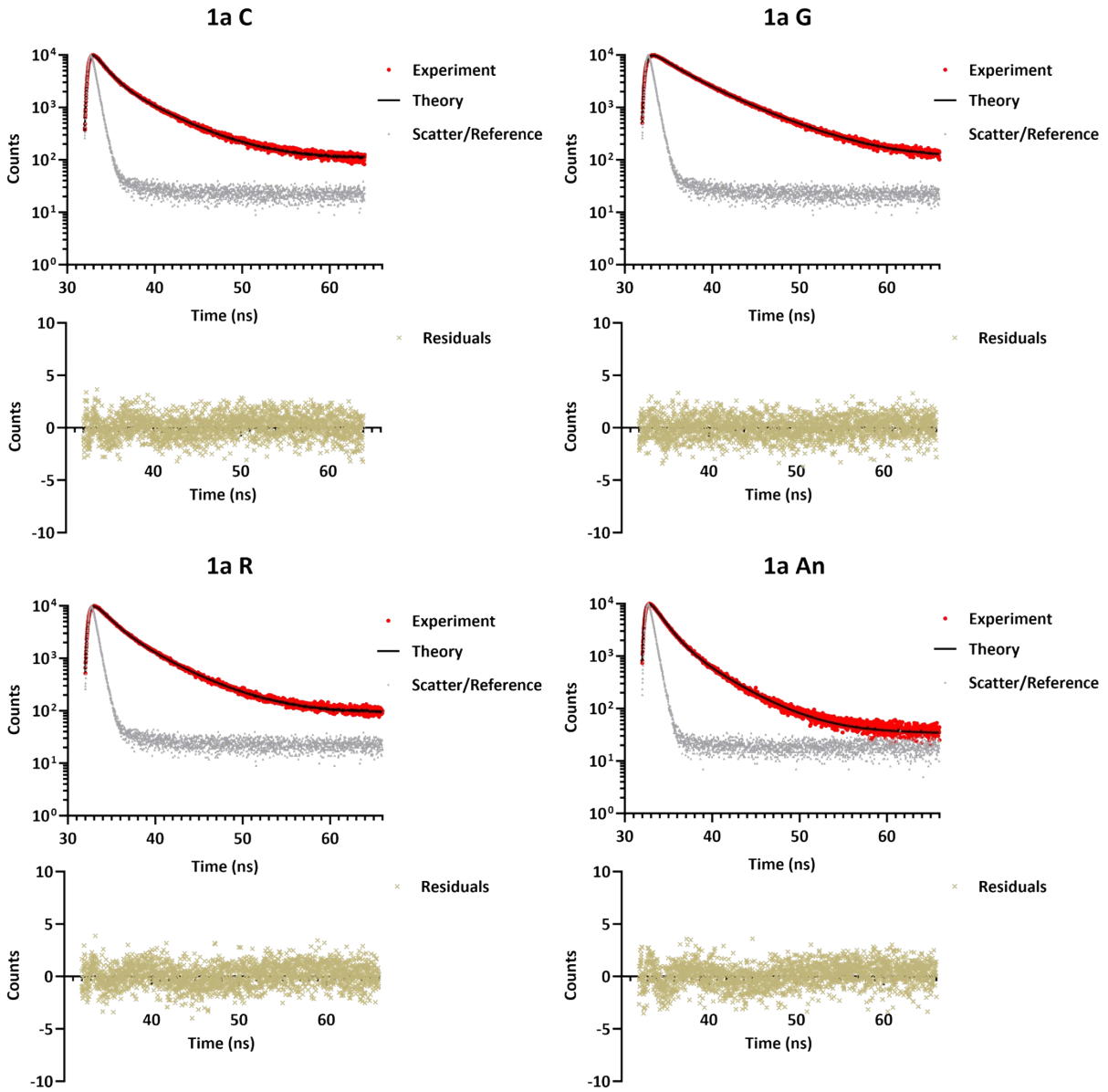

Figure S35. Fluorescence decay curves and fitted exponential functions for **1a**. Residuals are plotted separately below. The excitation wavelength was centered at 420 nm (40 nm band pass) and all emission above 490 nm was collected.

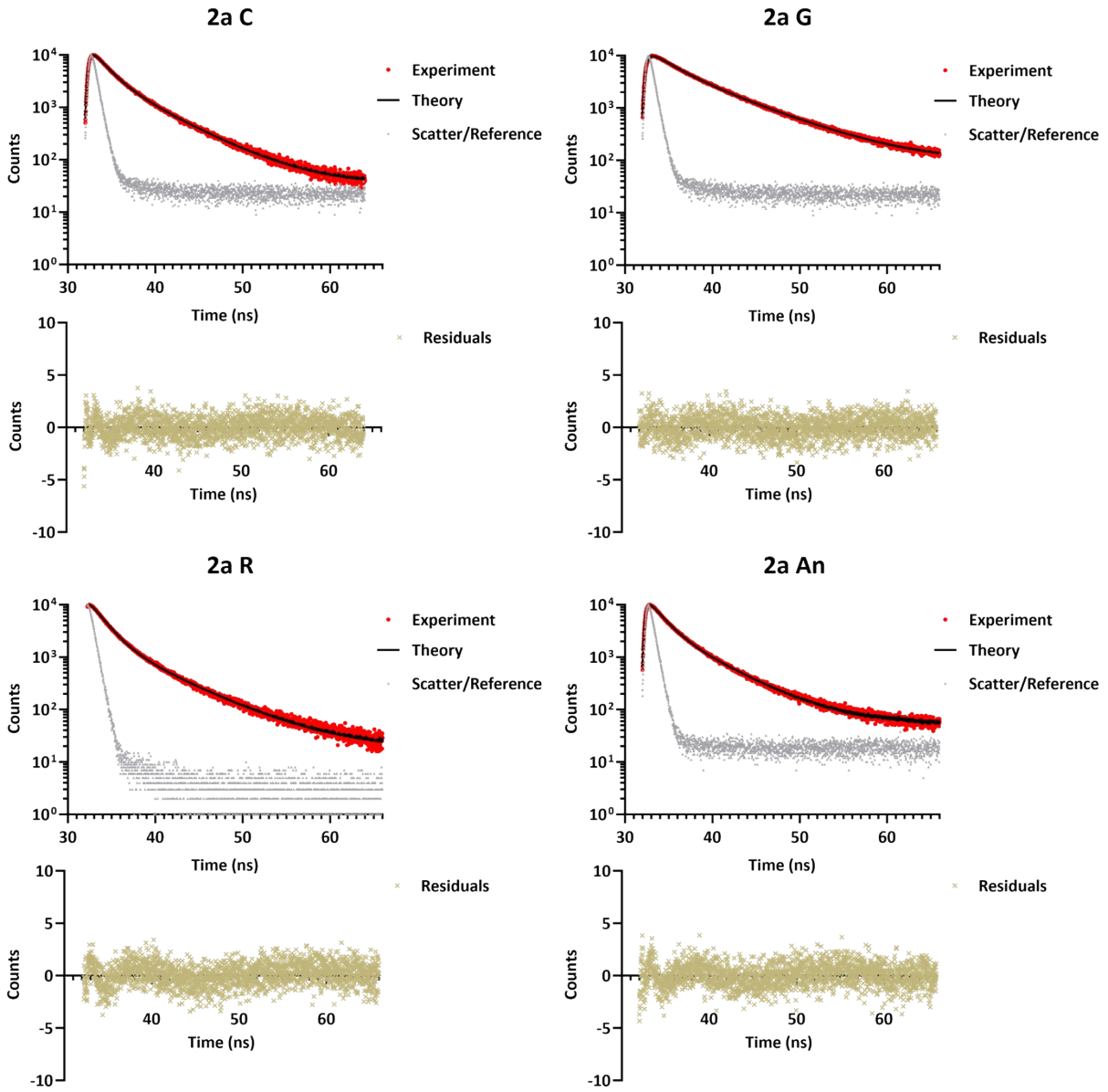

Figure S36. Fluorescence decay curves and fitted exponential functions for **2a**. Residuals are plotted separately below. The excitation wavelength was centered at 420 nm (40 nm band pass) and all emission above 490 nm was collected.

S12: Nuclear magnetic resonance spectra

^{1}H NMR

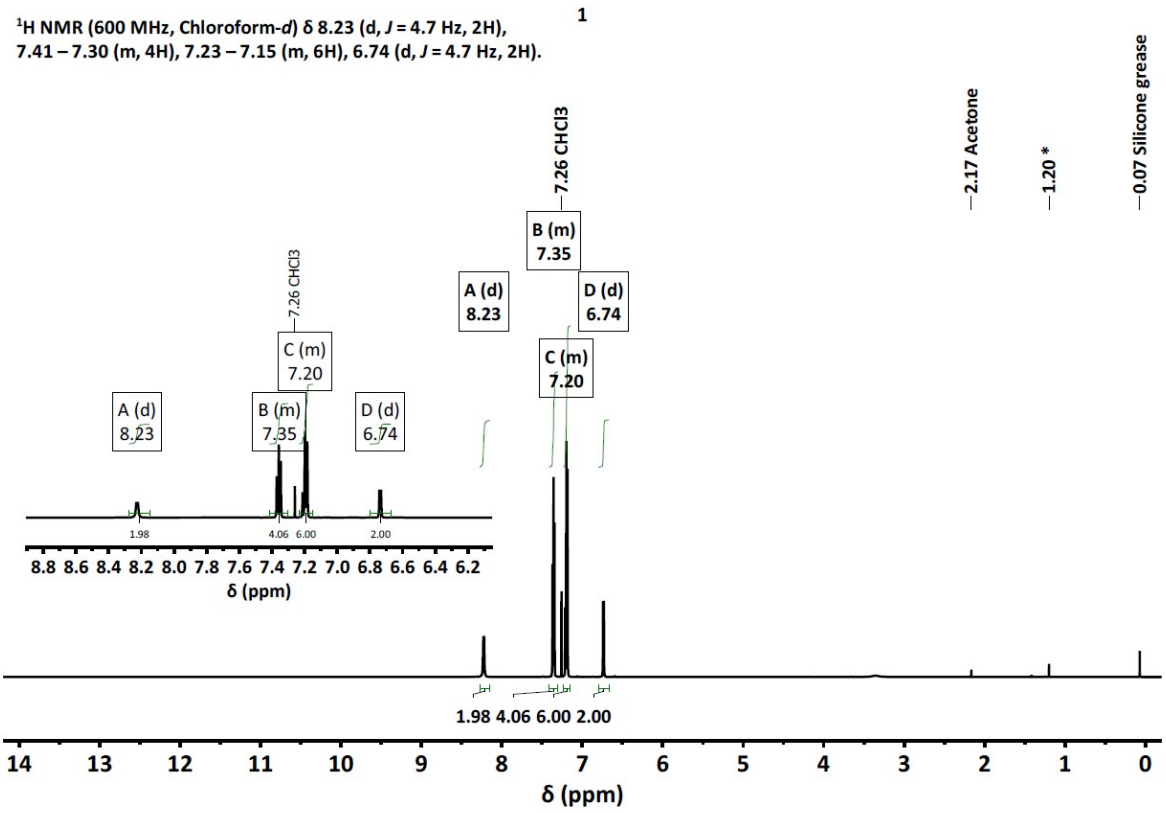

Figure S37. ^{1}H NMR spectrum for **1**.

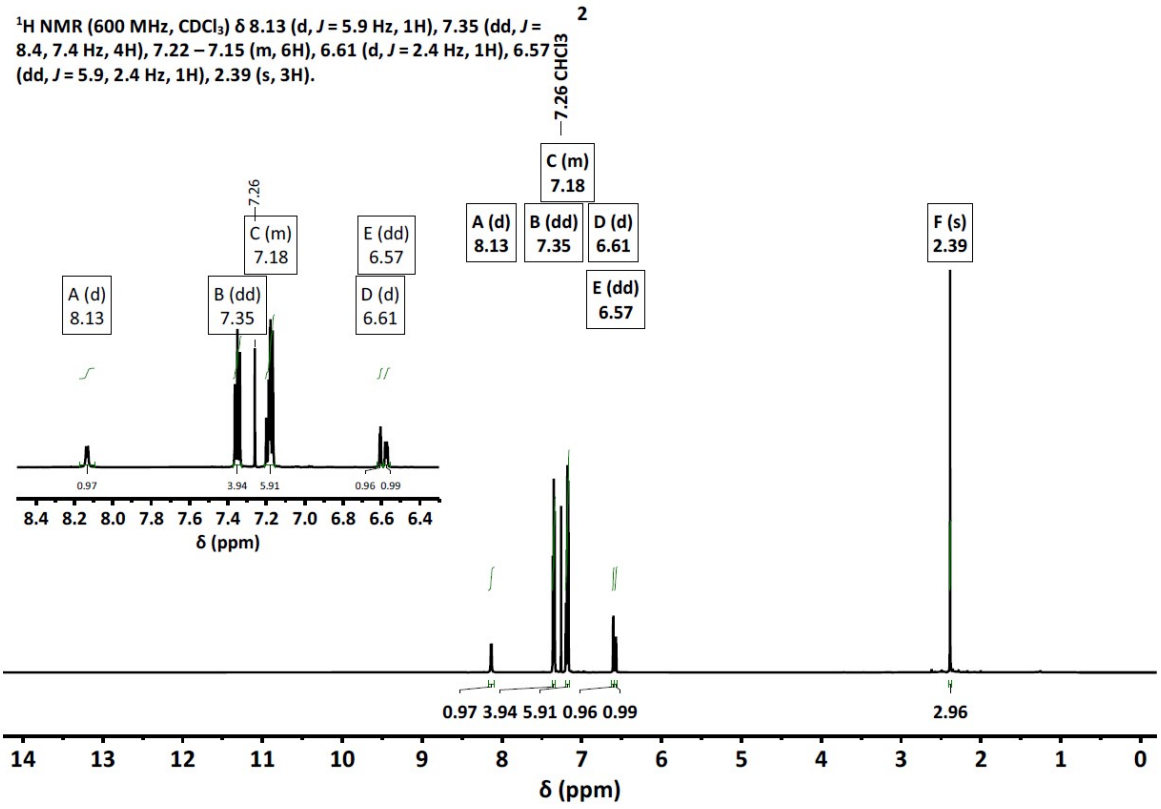

Figure S38. ^{1}H NMR spectrum for **2**.

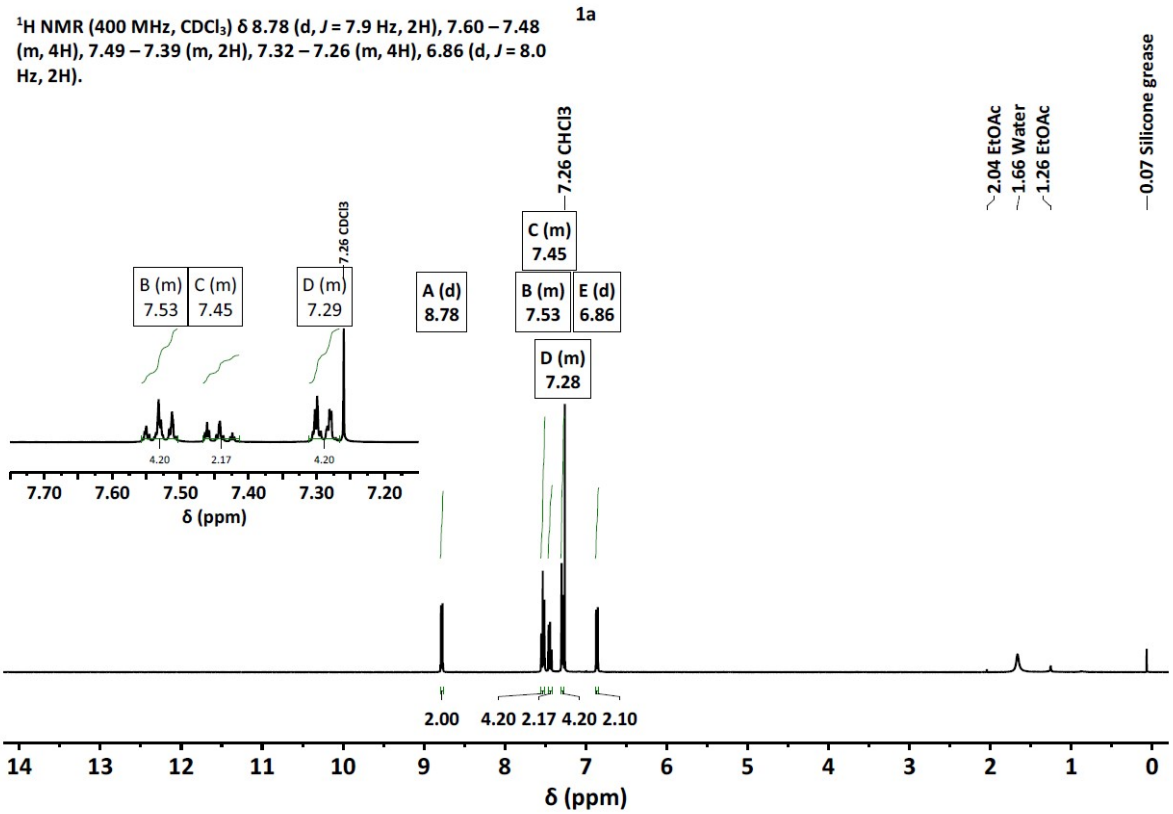

Figure S39. ^{1}H NMR spectrum for **1a**.

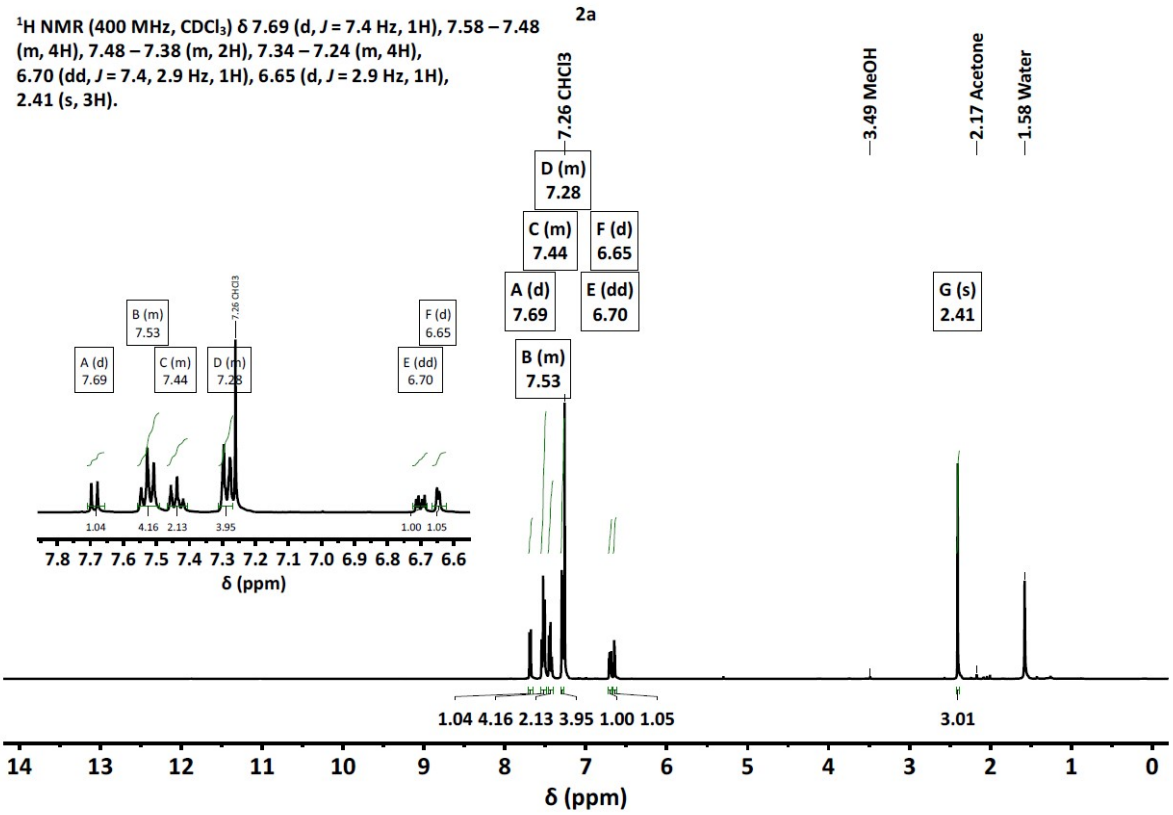

Figure S40. ^{1}H NMR spectrum for **2a**.

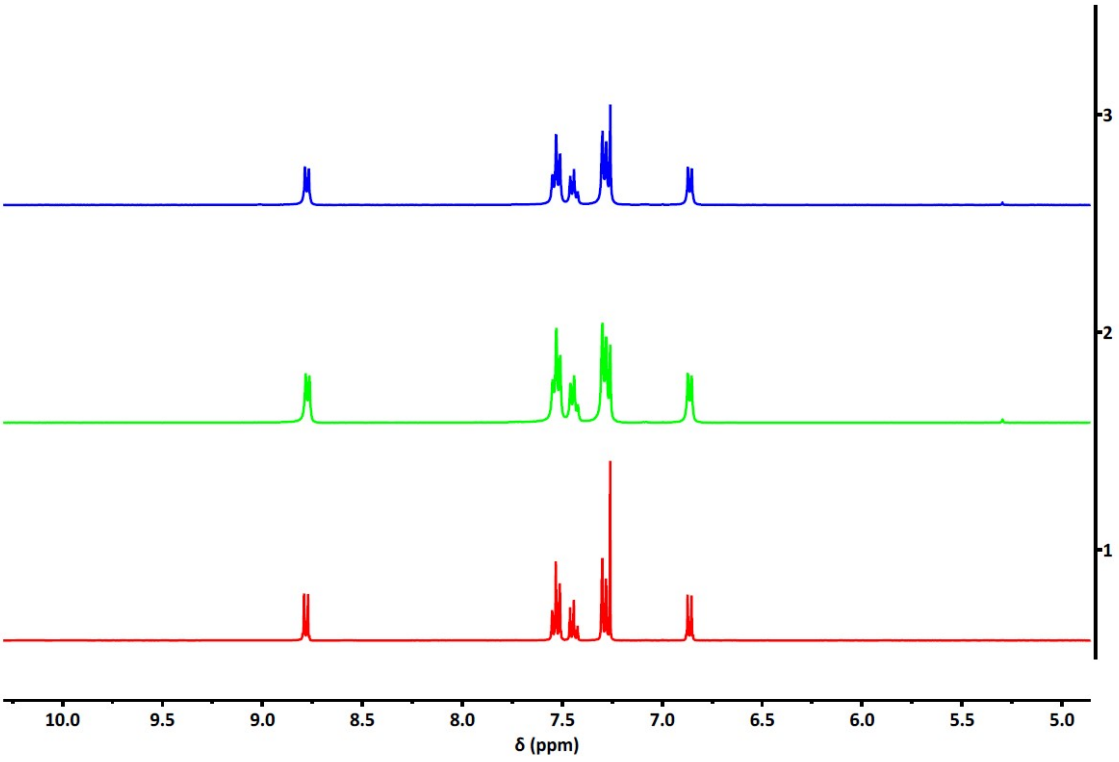

Figure S41. ^{1}H NMR spectra for the **C** (1), **G** (2) and **R** (3) forms of **1a**.

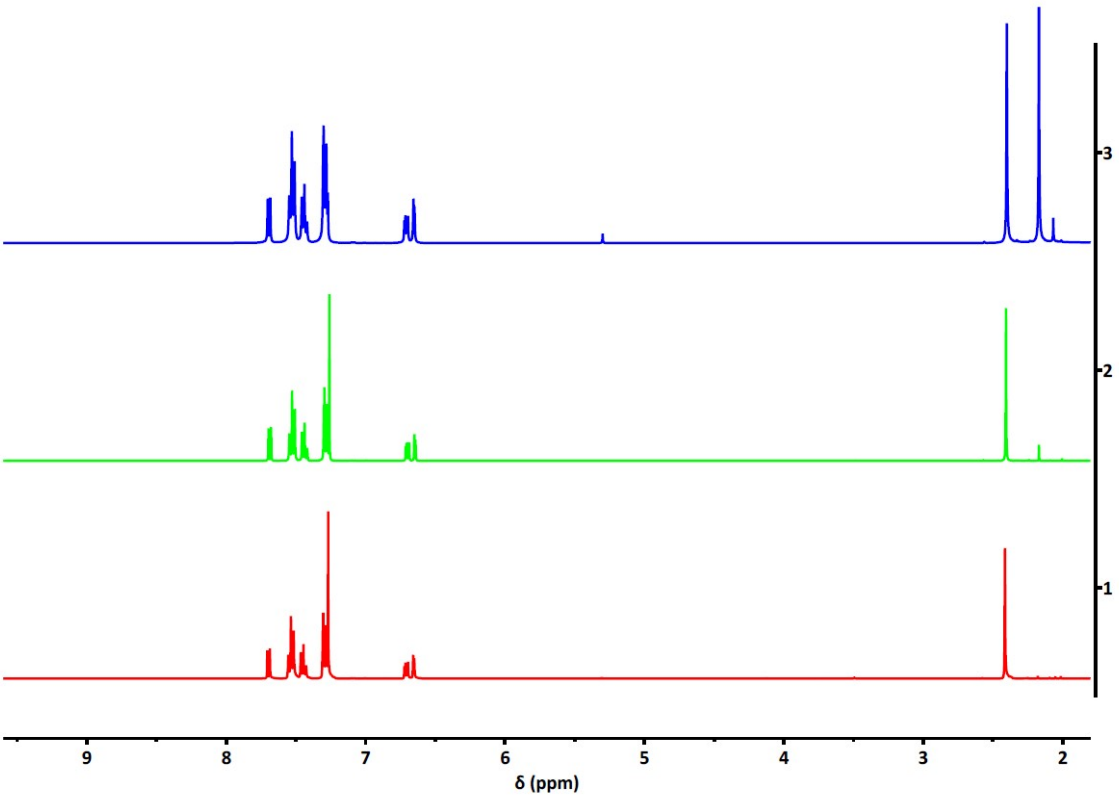

Figure S42. ^{1}H NMR spectra for the **C** (1), **G** (2) and **R** (3) forms of **2a**.

^{19}F NMR

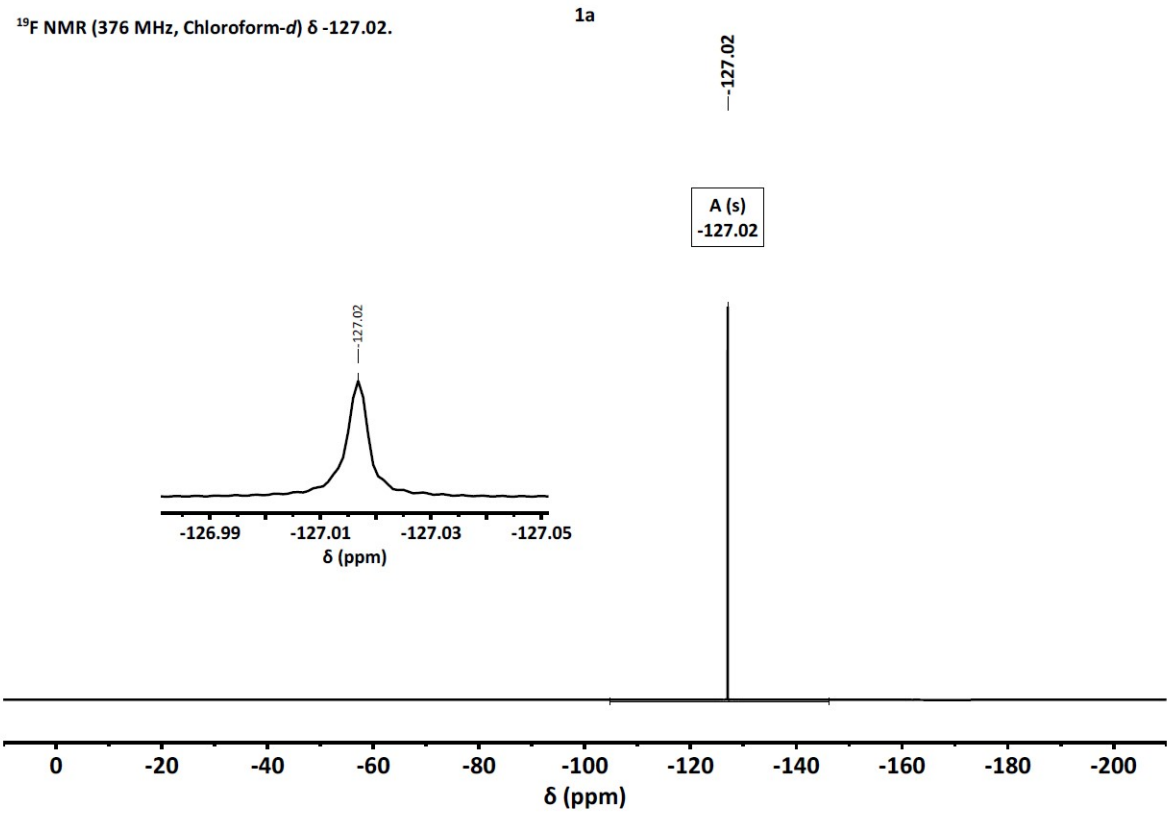

Figure S43. ^{19}F NMR spectrum for 1**a**.

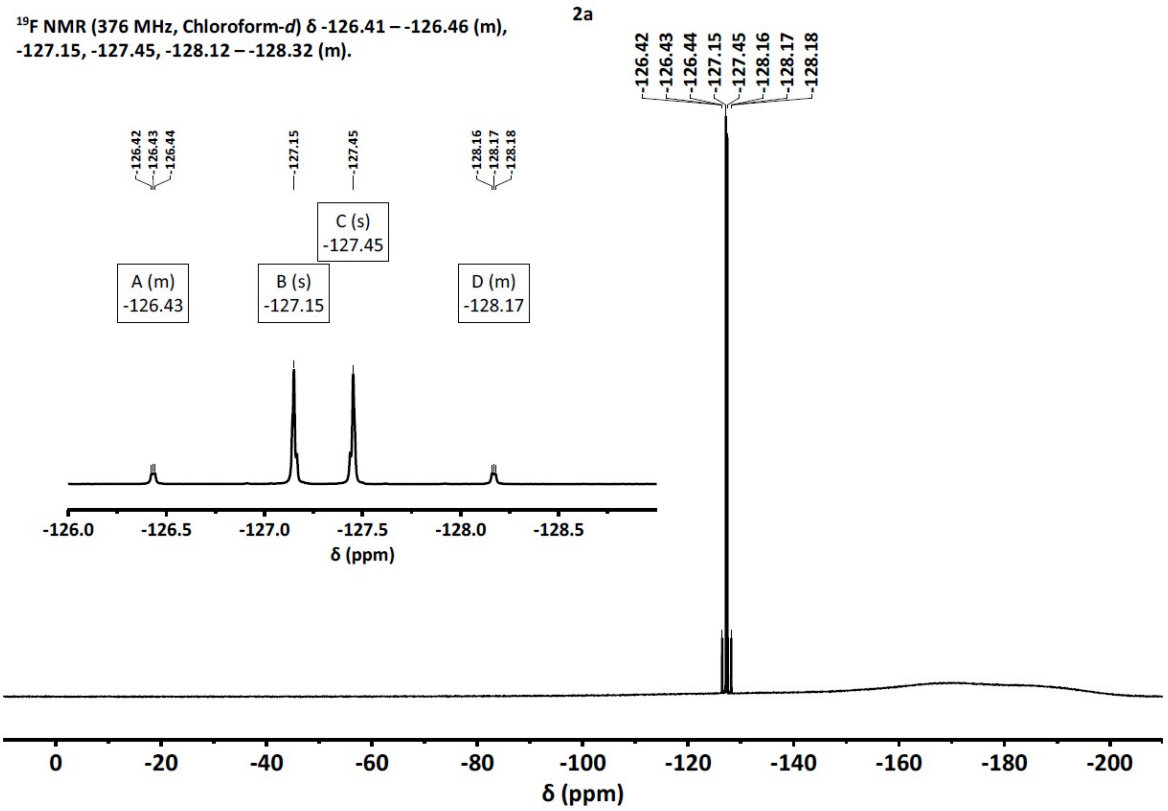

Figure S44. ^{19}F NMR spectrum for **2a**.

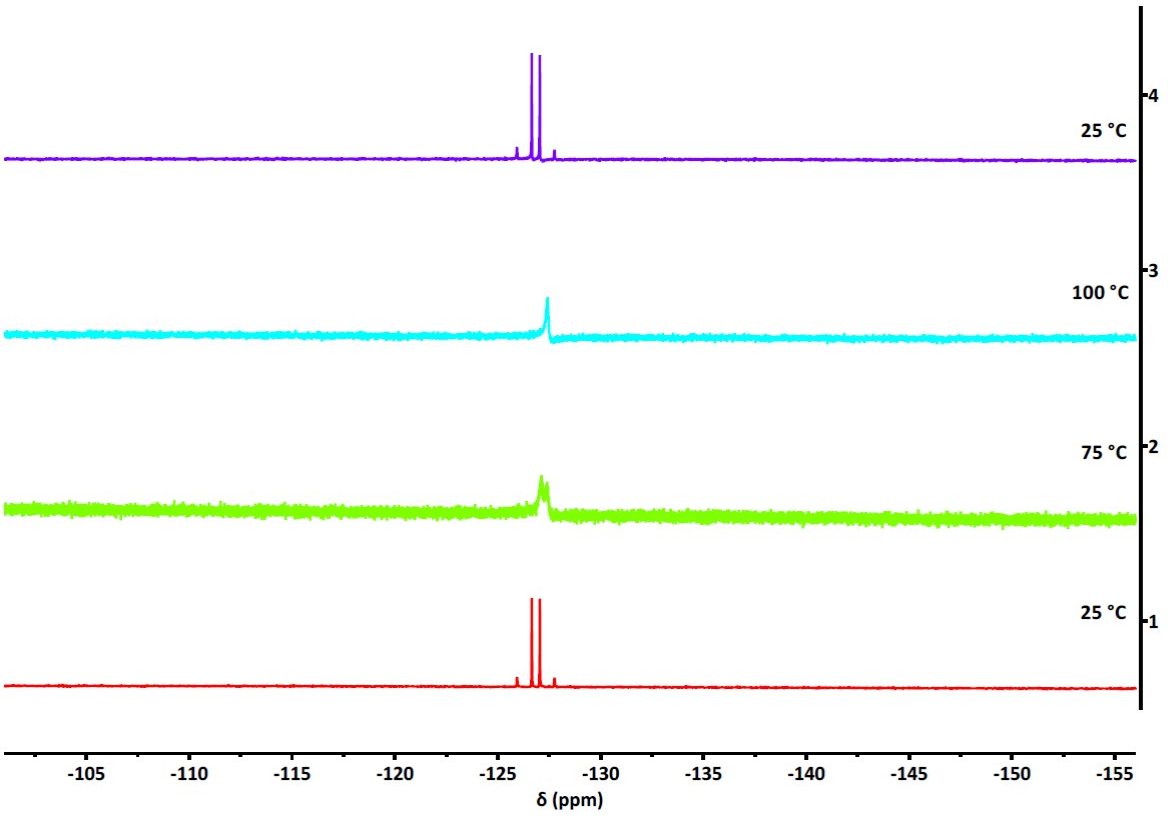

Figure S45. Variable temperature ^{19}F NMR spectra for **2a** in toluene-d_8.

^{13}C NMR*

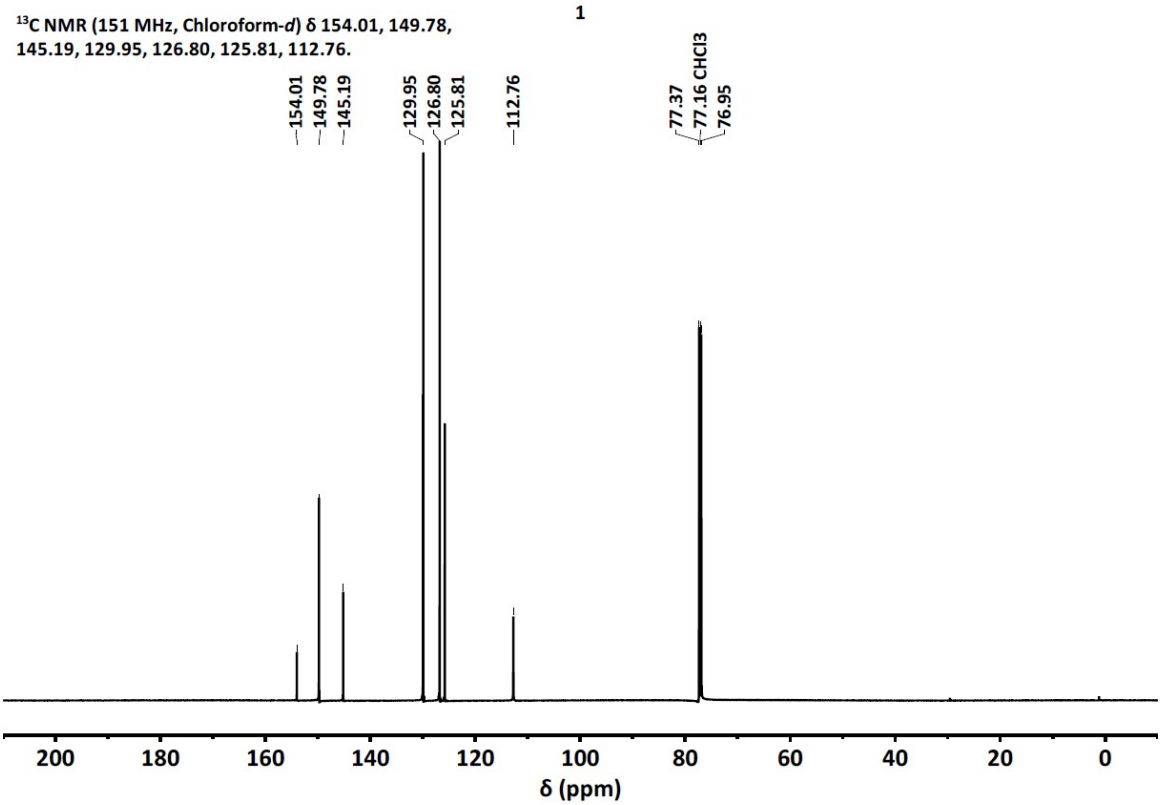

Figure S46. ^{13}C NMR spectrum for **1**.

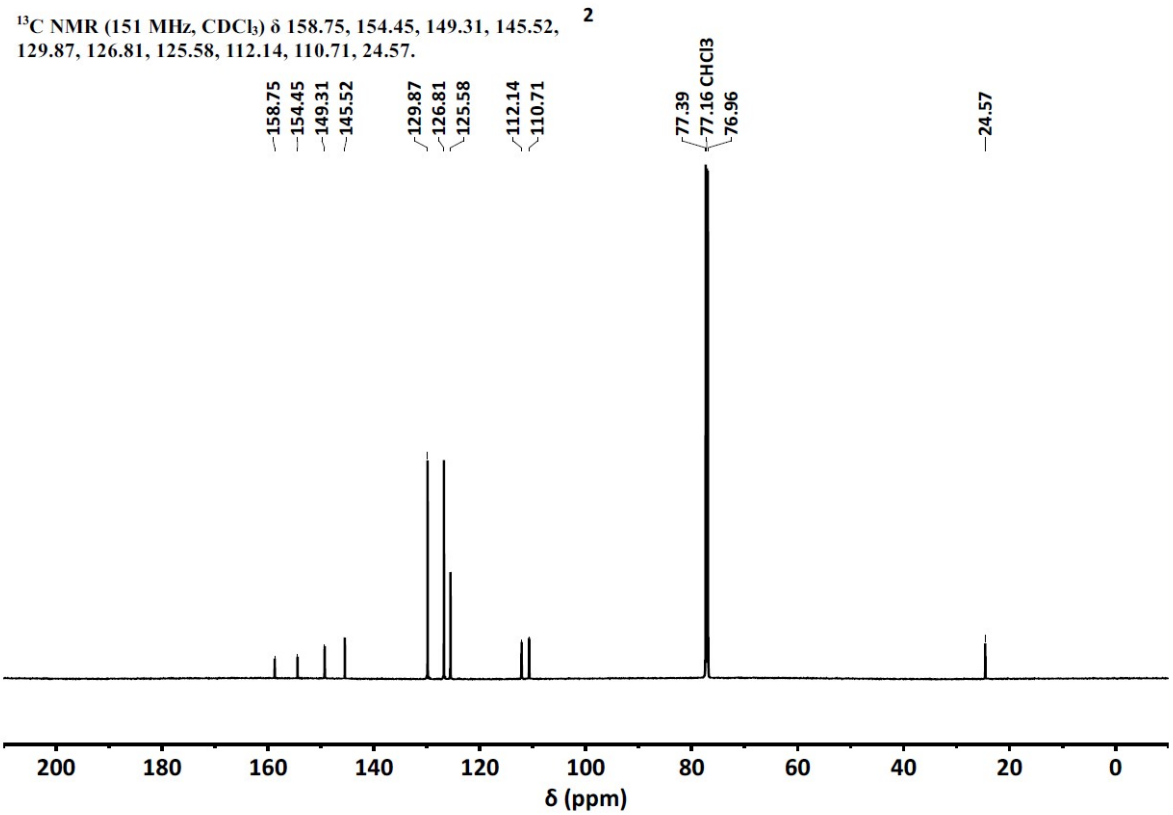

Figure S47. ^{13}C NMR spectrum for **2**.

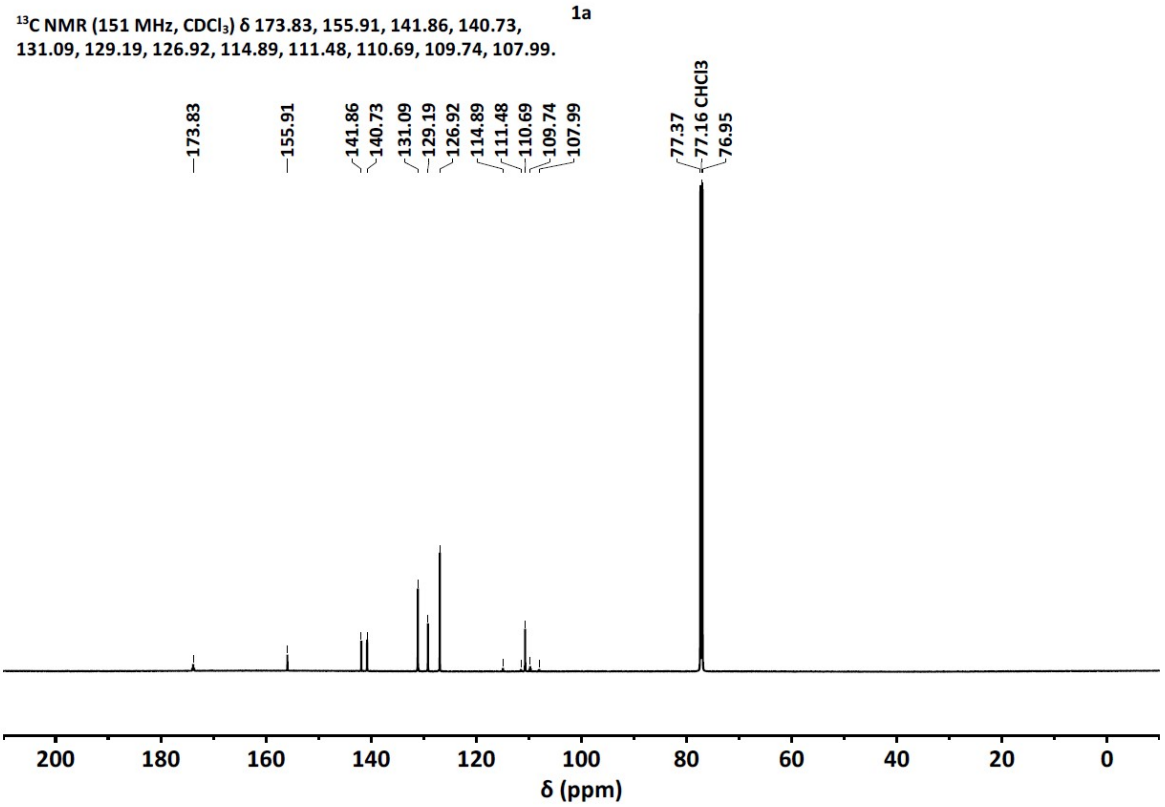

Figure S48. ^{13}C NMR spectrum for **1a**.

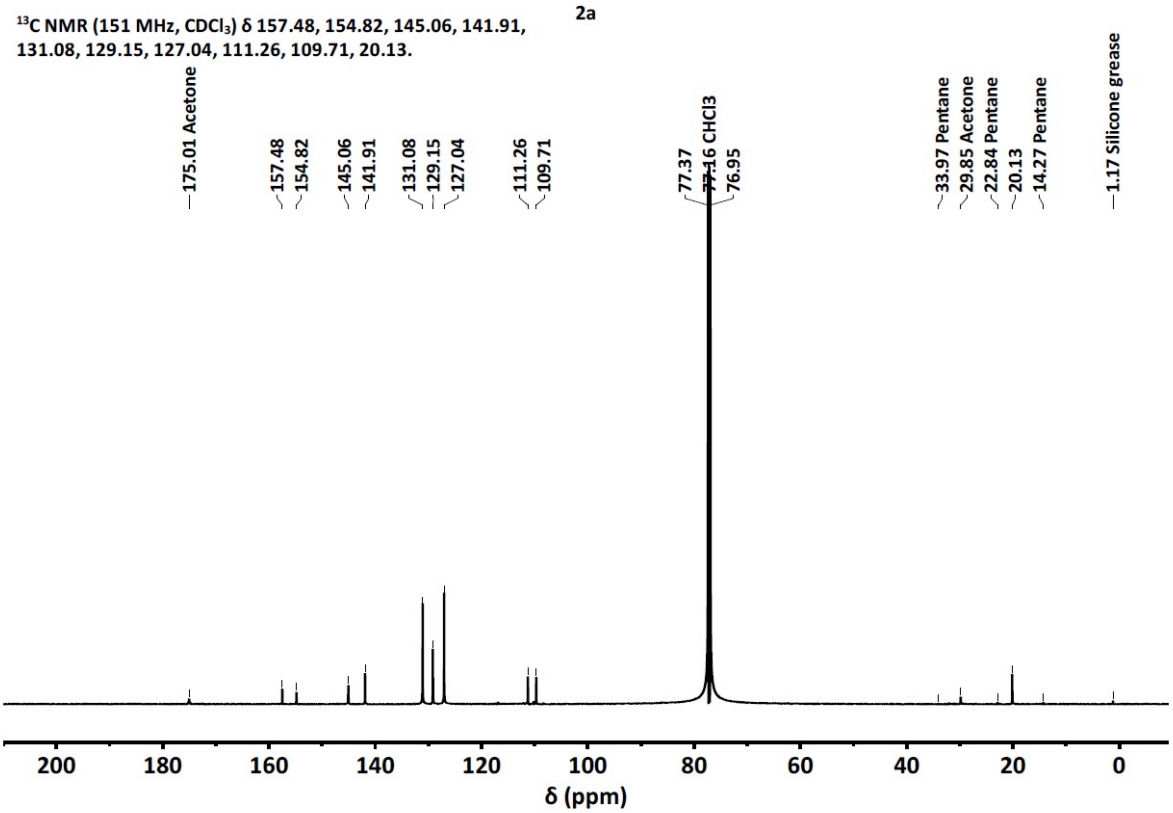

Figure S49. ^{13}C NMR spectrum for **2a**.

S13: Phosphorescence spectra

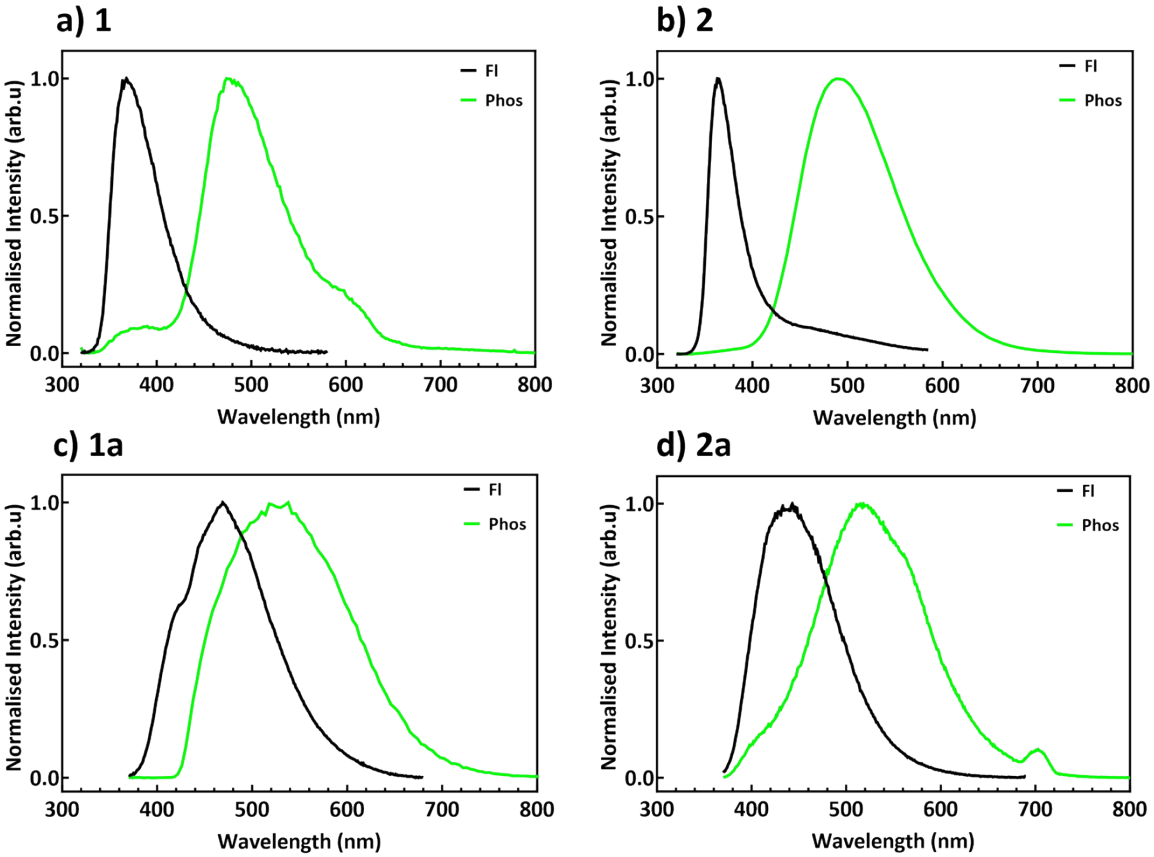

Figure S50. Overlay of fluorescence (black) and phosphorescence (green) spectra for crystalline forms of a) **1**, b) **2**, c) **1a**, and d) **2a**. Excitation wavelengths were set to 300 nm (**1** and **2**) or 350 nm (**1a** and **2a**). Fluorescence spectra are cut above double the excitation wavelength.

Table S15. Phosphorescence lifetime fitting parameters.

Compound	τ_1 ms	A1	τ_2 ms	A2	c	S.D.
1	0.246 ± 0.0	68.6703 ± 4.3	2.080 ± 0.1	49.2044 ± 1.7	1.0172 ± 0.3	0.3933
2	0.157 ± 0.0	82.1191 ± 3.6	1.469 ± 0.1	10.6449 ± 0.8	0.5116 ± 0.1	0.2709
1a	0.153 ± 0.0	24.5452 ± 2.0	2.350 ± 0.2	4.6937 ± 0.2	0.6504 ± 0.1	0.1444
2a	0.114 ± 0.0	13.3927 ± 2.1	1.231 ± 0.2	1.7331 ± 0.2	0.2087 ± 0.0	0.0721

Phosphoresecnce decays were fitted to the sum of two exponential terms,

$$f(t) = A_1\left(-\frac{t}{\tau_1}\right) + A_2\left(-\frac{t}{\tau_2}\right) + c$$

S14: Compression and shearing force experiments

The mechanical setup (Figure S51) is based on a cylindrical pestle (diameter = 20 mm) driven by a linear motor (Oriental Motor DRL60G-05B4M-KB) and a rotation motor (Oriental Motor AR46AK-H100-1). The crystalline powder sample is deposited on a pyrex glass window, and it can be subjected to pure compression or shearing stress that corresponds to a compression coupled with a rotation of the pestle. The crystalline powder is excited by a fibered UV light source (365 nm) placed at the bottom of the observation window. A CCD camera Retiga R3 equipped with an objective MVL7000 -18-108 mm EFL, f/2.5 (with a filter Thorlabs FESH0700) and a silver mirror (Thorlabs PFR14-P01 25x36x1 mm) placed at 45° under the optical window allow recording of fluorescence movies while mechanically stimulating the material. Force and torque values are recorded by a sensor (Futek MBA500 FSH00743) located between the linear and rotation motors.

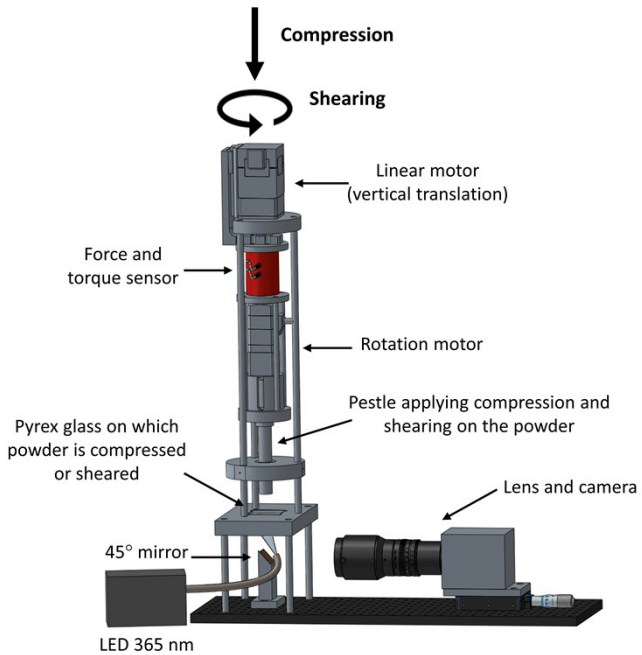

Figure S51. Schematic of the setup used for quantitative experiments under mechanical stimuli.

For the pure compression experiments, vertical compressions are controlled by a displacement speed of the pestle of 0.002 mm/s. For the shearing experiments, a piece of non-fluorescent paper is attached to the pestle with double-sided tape to shear the powder sample without scratching the glass. Compression ramps are applied by controlling the vertical force until 100 N at a speed of 0.25 N/s and rotation of the pestle is simultaneously performed at 0.3 RPM. Torque and vertical force values are recorded every second by the inhouse Agnes software of LMS (Solid Mechanics Laboratory, Ecole Polytechnique). During these compression and shearing experiments, movies are recorded via Ocular software by selecting the "Daylight" mode, an exposure time of 300 ms and a frame interval of 1 s for compression experiments and 2 s for shearing experiments. Three pure compression experiments and three shearing experiments were performed for both **1a** and **2a**.

Image Colourimetric Analysis

First, the raw movies, recorded in RGB colour space by the camera, are converted into HSV (hue, saturation and value) colour space using the appropriate set of mathematical equations (step 1 in Fig. S52). In HSV colour space, all the colour information is contained in the hue parameter, H, whereas saturation and value parameters express respectively purity and intensity of the colour. A lower magnitude of H indicates a more red-shifted colour. The H coordinate was then extracted from each pixel of the first and last images of the movies and the corresponding H histograms were plotted in blue and green, respectively (step 2 in Figure S52).

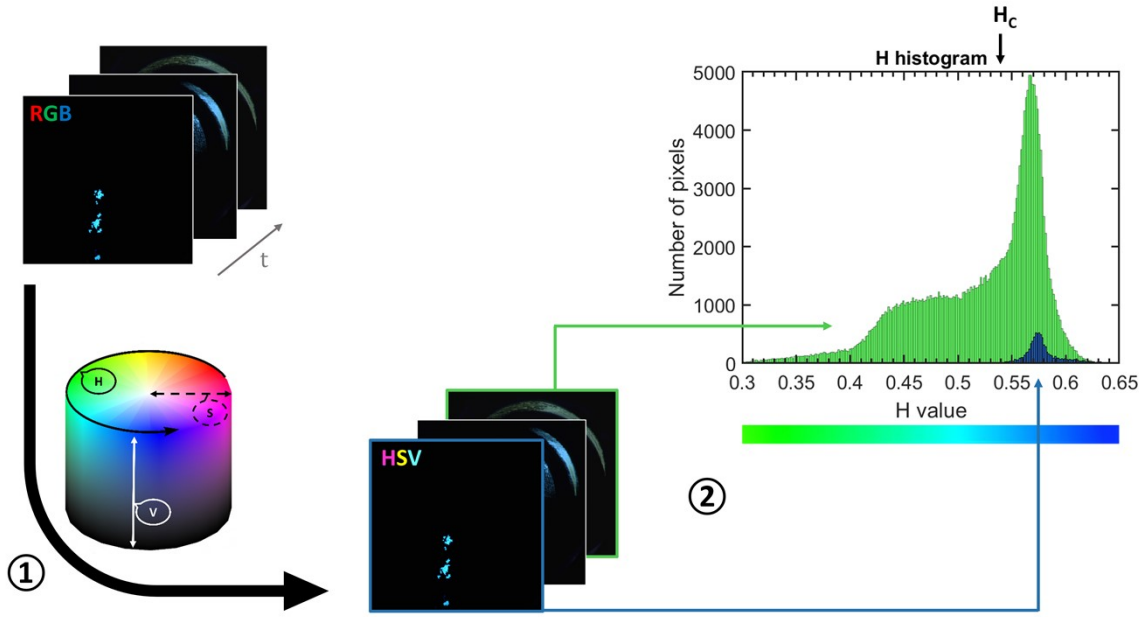

Figure S52. Colourimetric analysis flowchart for a shearing experiment on compound **1a**.

According to the H histograms before mechanical stimulation (in blue), the H coordinates of blue fluorescence are initially centered around 0.57 and 0.61 for **1a** and **2a**, respectively (Figure 8). After pure compression (in green), green pixels appear to have lower H values in the [0.51-0.55] and [0.44-0.57] intervals for **1a** and **2a**, respectively. In the case of the shearing experiments, a second distribution can be observed at lower H values after mechanical stimulation, due to the spreading of the powder on the glass slide. As a consequence, critical values of H, named H_c, were respectively determined at 0.54 and 0.56 for **1a** and **2a** to properly detect the appearing green pixels. In the following steps, all the pixels having a $H<H_c$ are counted as green and are thus considered as having undergone a mechanically-induced transformation.

Relating fluorescence colour change to the applied compression force

For the pure compression experiments, the fluorescence colour change has been expressed as the ratio of shifting blue pixels over the total fluorescent pixels (in %), which is defined as follows:

$$Ratio = \frac{Number\ of\ detected\ pixels\ (green)}{Number\ of\ total\ fluorescent\ pixels\ (blue + green)}$$

For **2a** the initial ratio begins at 0% whereas for **1a** it begins at ≈1.5%, meaning that this amount of material is already detected as green. This trend, which is observed over all the pure compression experiments, is probably due to the better separation of hue coordinate between the initial blue fluorescence and the green one for **2a** than for **1a**. Then, the compressive force at which the ratio starts to increase is considered the force threshold required to induce the **MFC** transition. To determine it precisely, the curves are fitted by a set of two straight lines, and the intersection between the horizontal line and the oblique one is taken as the compressive force threshold.

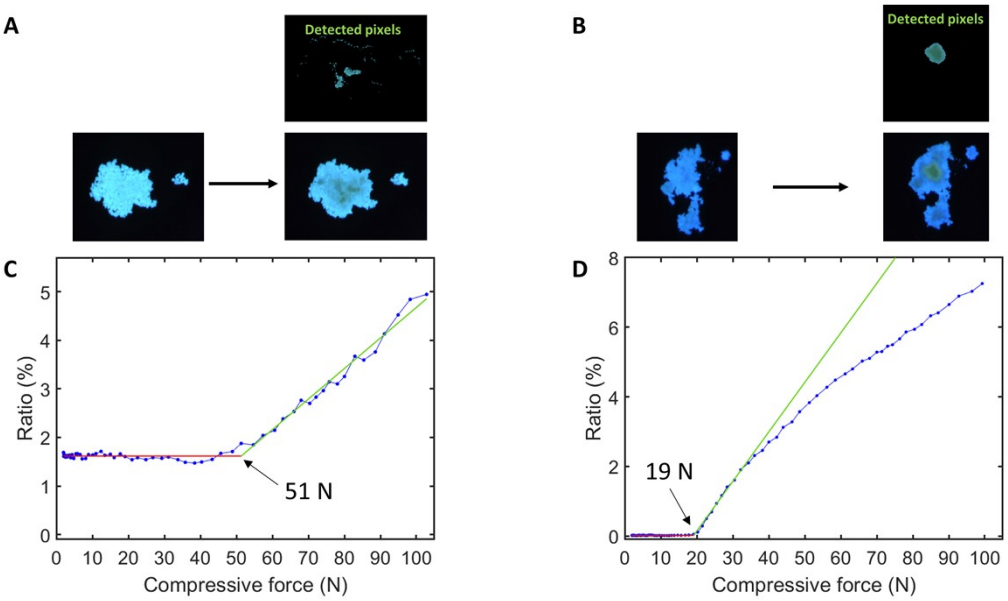

Figure S53. First and last images of the movies as well as last image after detection of shifting green pixels for one of the three pure compression experiments on (A) **1a** and (B) **2a**. Corresponding plots of ratio vs compressive force for (C) **1a** and (D) **2a** with identification of the force threshold required to induce the **MFC** transition.

Table S16. Compression force and shearing stress thresholds for all the experiments performed on **1a** and **2a**.

	1a	**2a**
Pure compression experiments (N)	51	13
	51	31
	55	19
Shearing experiments (kPa)	20.6	4.8
	10.1	6.7
	5.1	4.7

Analysis of the Shearing Force Experiments

Shearing experiments are performed by applying a ramp of vertical force from 0 to 100 N, combined with a rotation of the pestle.

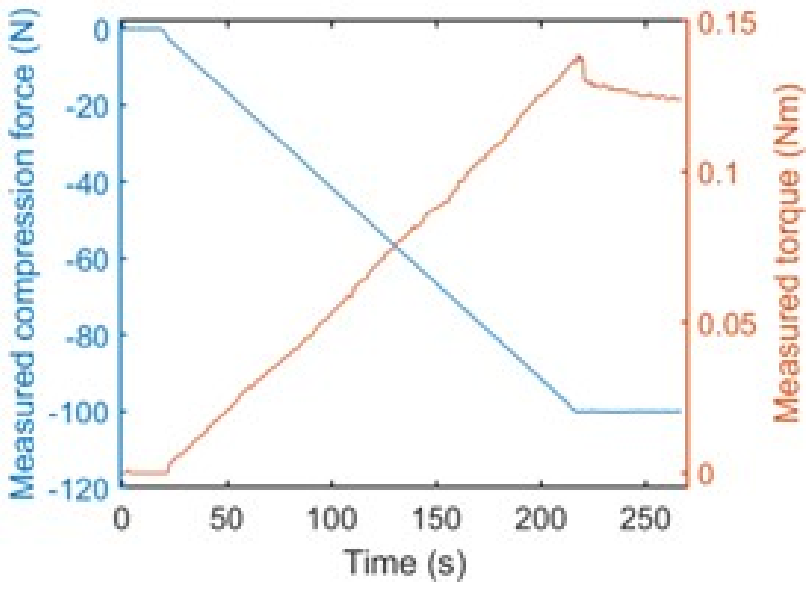

Figure S54. Plot of the measured compression force (blue) and torque (orange) versus the time of the movie for a typical shearing experiment.

As previously shown, the shear stress that locally induces an **MFC** response, *S* (in Pa), can be expressed as a function of the pixel distance to the pestle center *r* and measure torque *C* as in the following equation:

$$S(r) = r \times \frac{2C}{\pi R^4}$$

with *R* the pestle radius.

Finally, plotting all the local shearing stresses including **MFC** against time allows the determination of the shearing threshold as the lowest local shearing at which a pixel is detected as green, as shown in Figure S55.

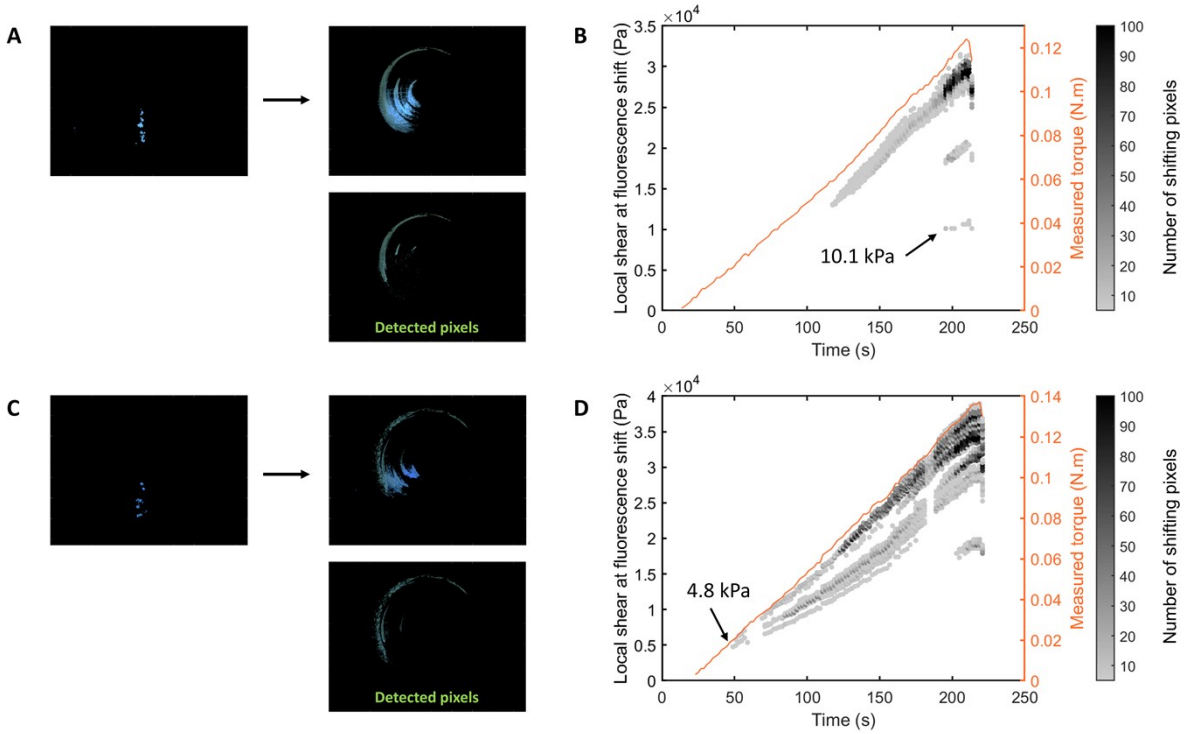

Figure S55. First and last images of the movies as well as last image after detection of shifting green pixels for one of the three shearing experiments on (A) **1a** and (C) **2a**. Corresponding plots of local shear at fluorescence shift versus time of the movie for (B) **1a** and (D) **2a** with identification of the shear threshold required to induce the **MFC** transition.

S15: Fluorescence lifetime imaging confocal microscopy

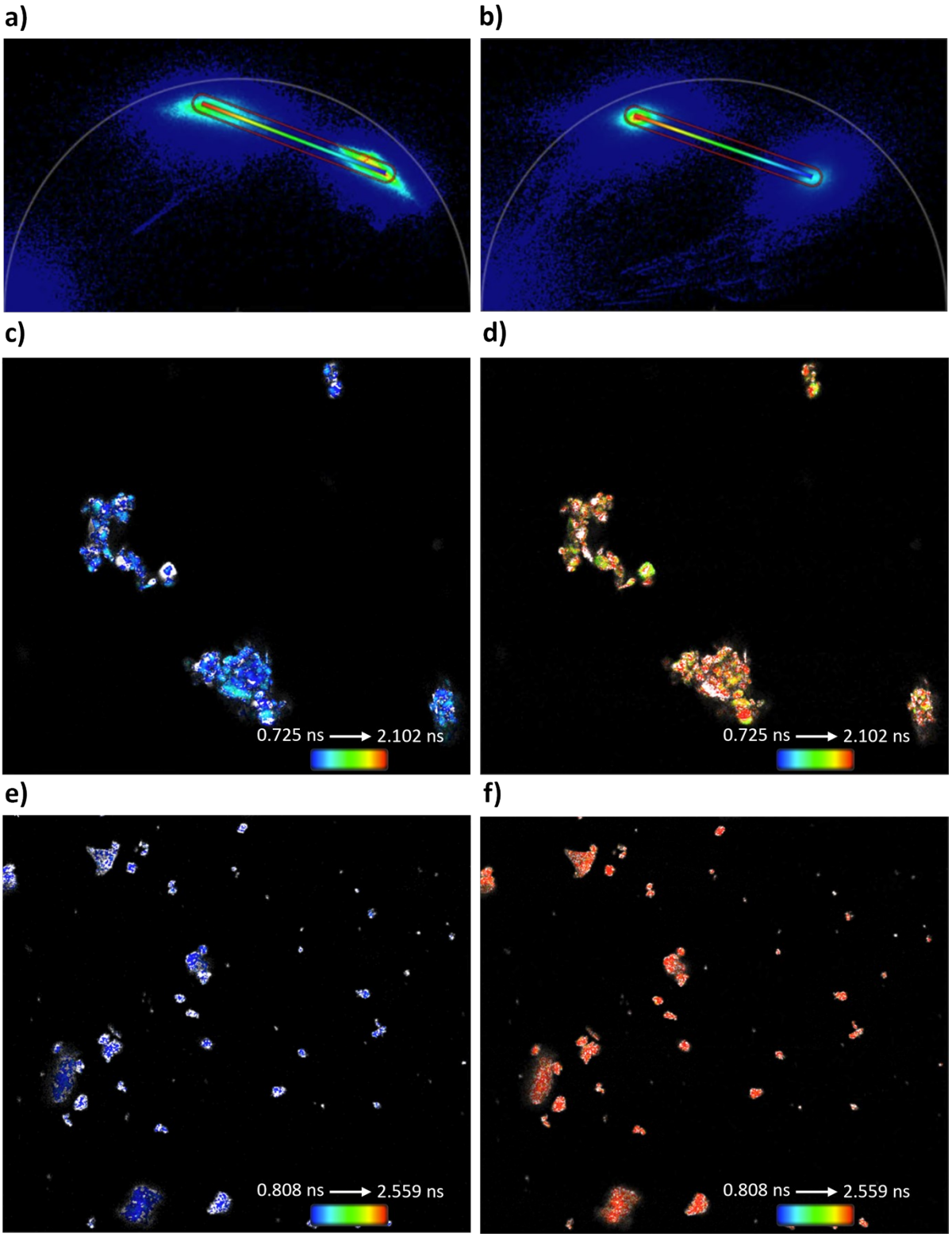

Figure S56. Phasor plots for a) **1a**-C 2, b) **1a**-G 2. FLIM mapping for c) **1a**-C 2 with blue band pass 401-450 nm, d) identical region of **1a**-C 2 with green band pass 480-530 nm, e) **1a**-G 2 with blue pass band, f) identical region of **1a**-G 2 with green pass band.

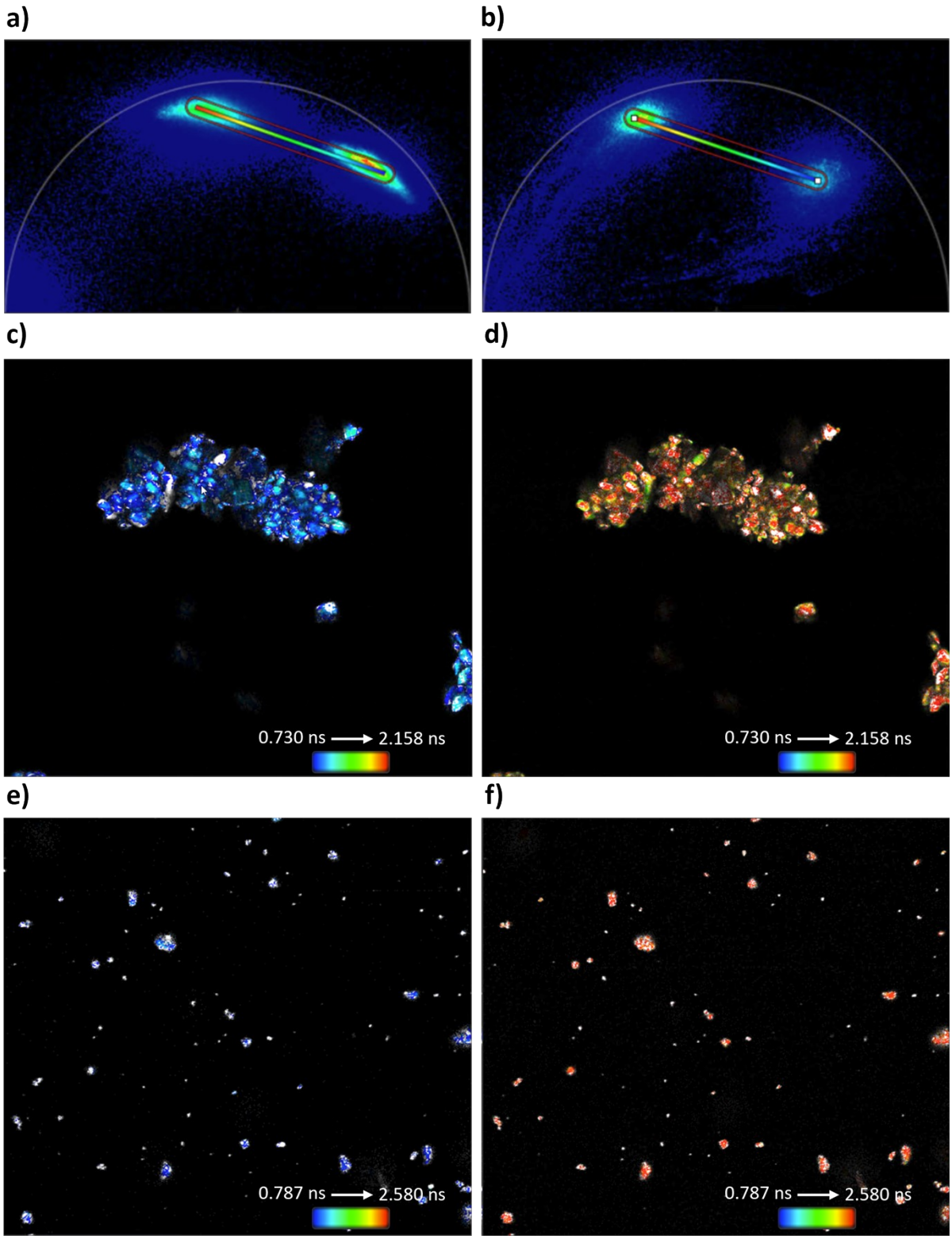

Figure S57. Phasor plots for a) **1a**-C 3, b) **1a**-G 3. FLIM mapping for c) **1a**-C 3 with blue band pass 401-450 nm, d) identical region of **1a**-C 3 with green band pass 480-530 nm, e) **1a**-G 3 with blue pass band, f) identical region of **1a**-G 3 with green pass band.

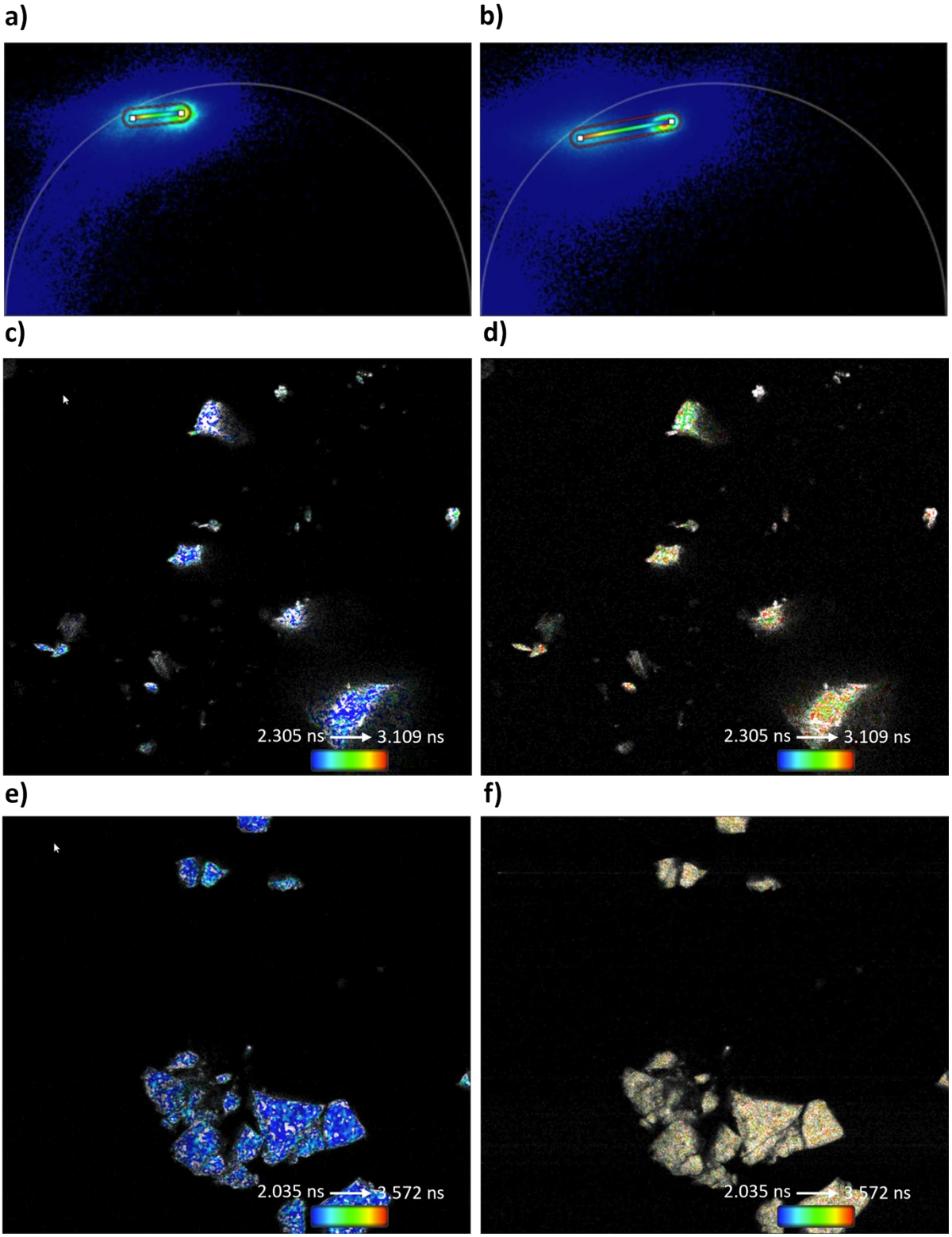

Figure S58. Phasor plots for a) **2a**-C 2, b) **2a**-G 2. FLIM mapping for c) **2a**-C 2 with blue band pass 401-450 nm, d) identical region of **2a**-C 2 with green band pass 480-530 nm, e) **2a**-G 2 with blue pass band, f) identical region of **2a**-G 2 with green pass band.

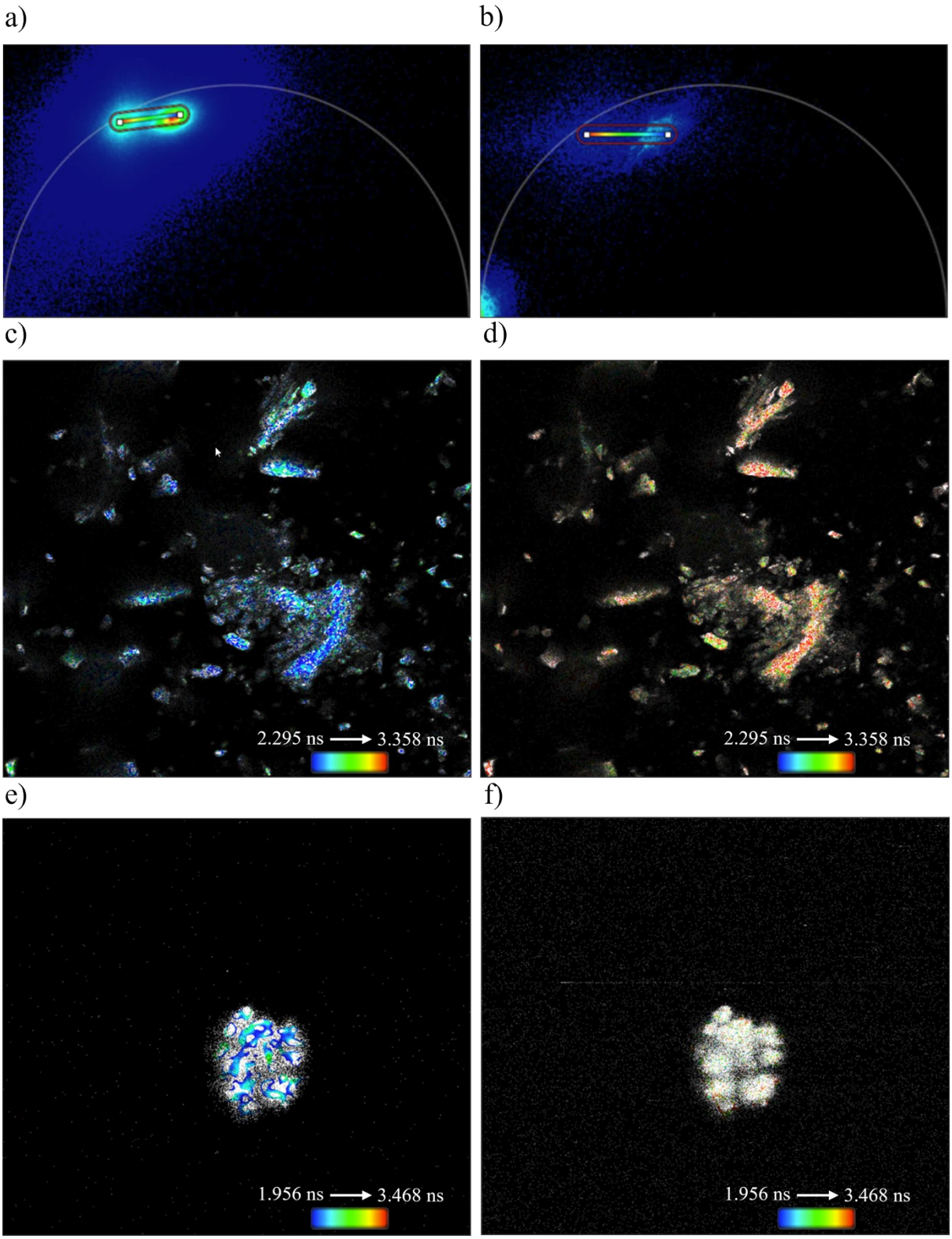

Figure S59. Phasor plots for a) **2a**-C 3, b) **2a**-G 3. FLIM mapping for c) **2a**-C 3 with blue band pass 401-450 nm, d) identical region of **2a**-C 3 with green band pass 480-530 nm, e) **2a**-G 3 with blue pass band, f) identical region of **2a**-G 3 with green pass band.

S16: Quantum chemical calculations

Ground state molecular orbitals

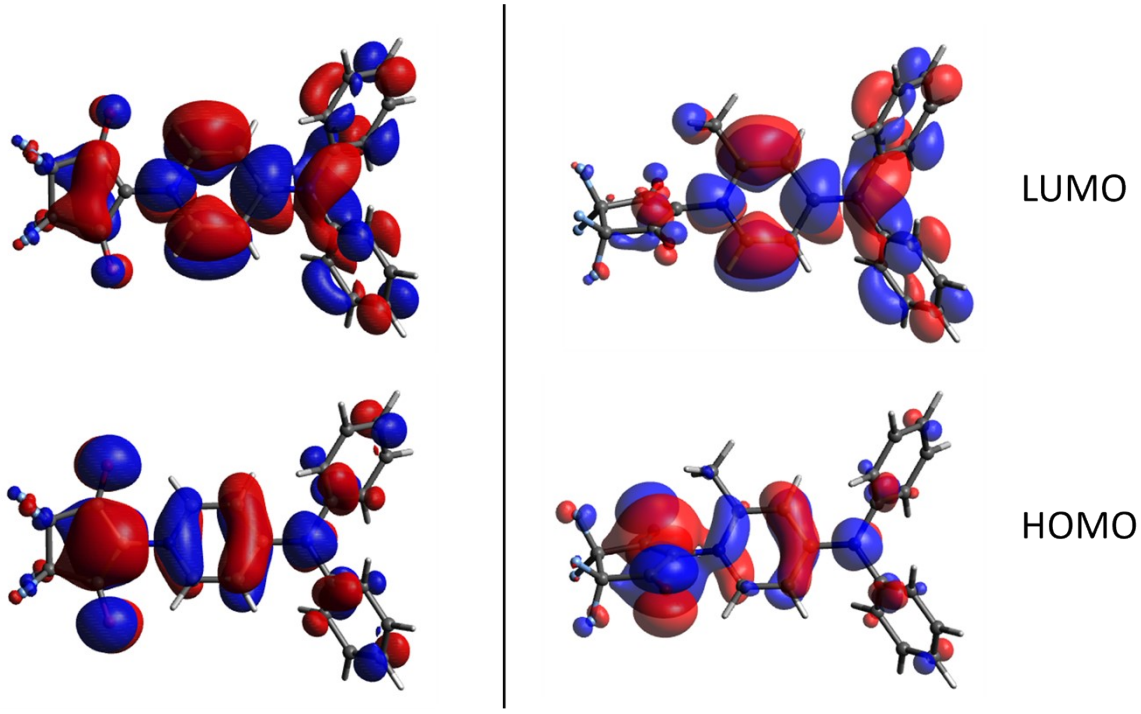

Figure S60. ωB97X/def2-TZVP orbitals (plotted with Avogadro) for **1a** and **2a** (isosurface value 0.02).

Calculated absorbance and emission energies

Table S17. Calculated transition energies at the TD-ωB97X/def2-TZVP level of theory for **1a** in the gas phase.

Compound	Absorbance **nm (cm^{-1})**	Emission **nm (cm^{-1})**
1a	288 (34722)	400 (25000)
2a	297 (33670)	443 (22573)

1a: C_P-N_1 Bond Rotation Scan

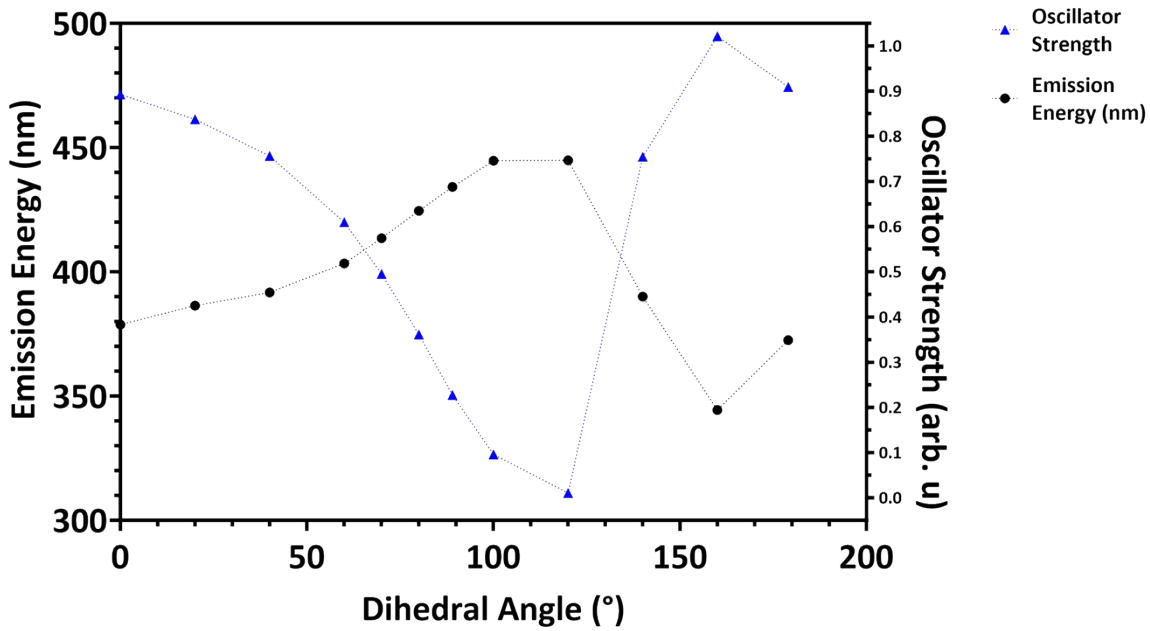

Figure S61. Emission wavelength (nm) and oscillator strength vs the dihedral angle describing a rotation around the C_P-N_1 bond in **1a** based on a relaxed surface scan of the S_1 state at the TD-ωB97X/def2-TZVP level of theory.

Table S18. Emission energy and oscillator strengths as a function of rotation around C_{13}-N_1 bond conducted at the TD-ωB97X/def2-TZVP level of theory.

Dihedral Angle **°**	Em E **nm**	Oscillator Strength
0	378.8	0.8925
20	386.4	0.8378
40	391.7	0.7563
60	403.4	0.6098
70	413.5	0.4955
80	424.6	0.3612
89	434.2	0.2276
100	444.7	0.0961
120	444.9	0.0104
140	390.0	0.7548
160	344.4	1.0215
179	372.5	0.9091

S17: FT-IR spectra (neat)

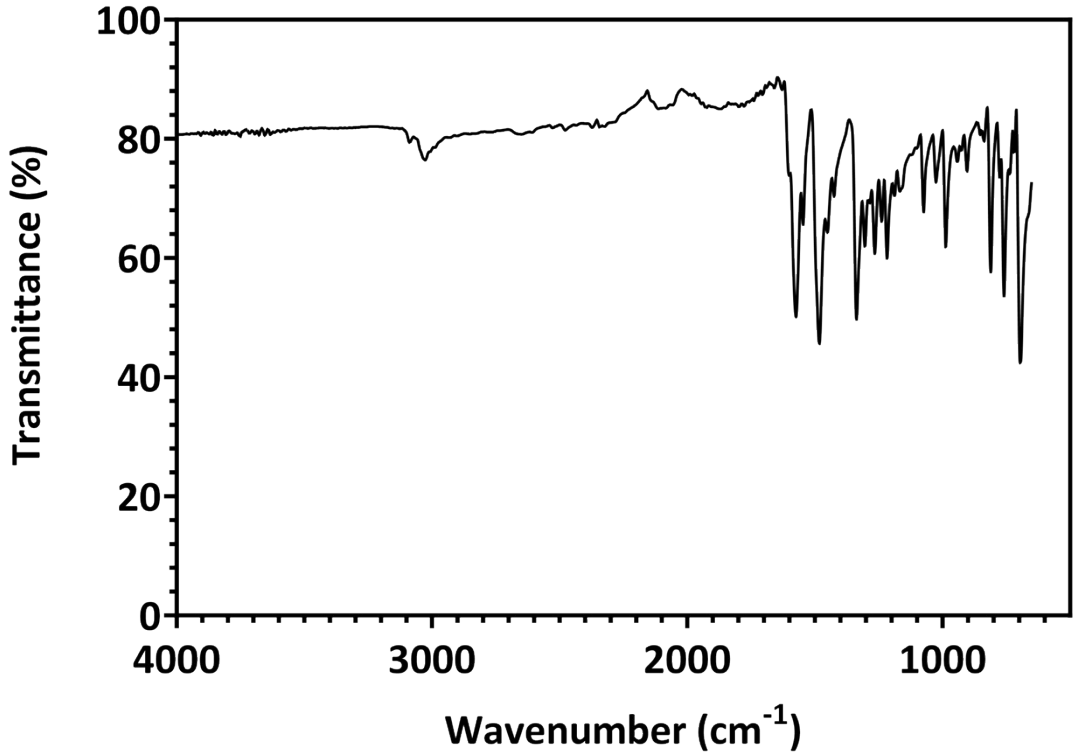

Figure S62. FT-IR spectrum of **1**.

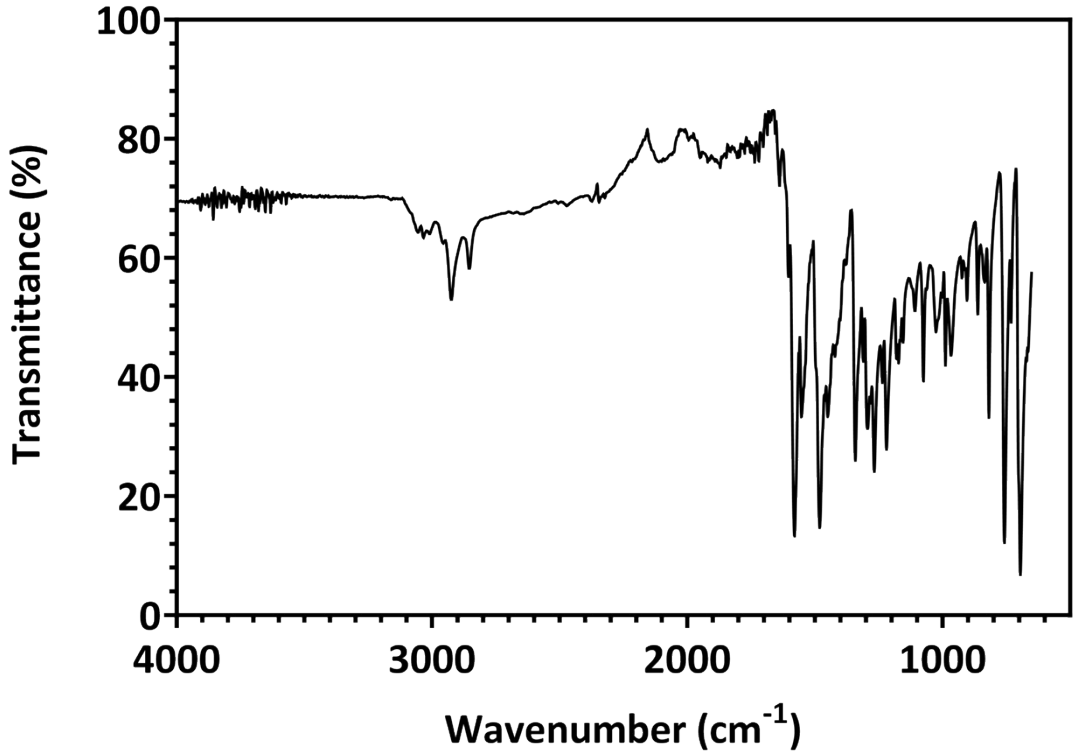

Figure S63. FT-IR spectrum of **2**.

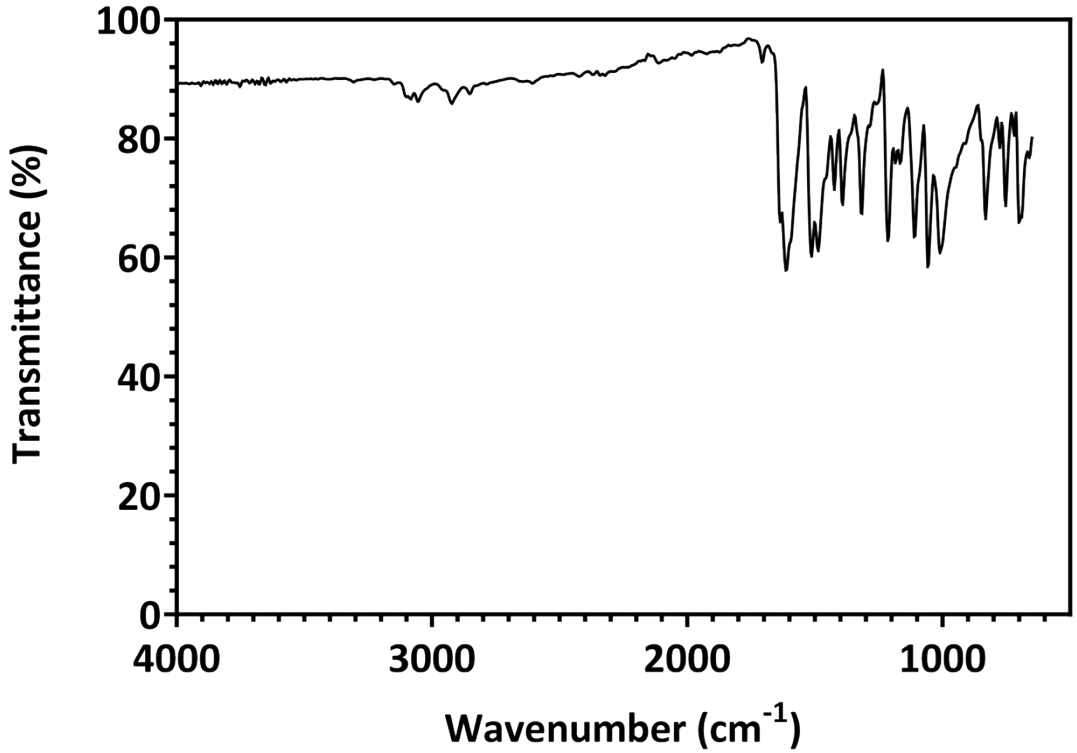

Figure S64. FT-IR spectrum of **1a**.

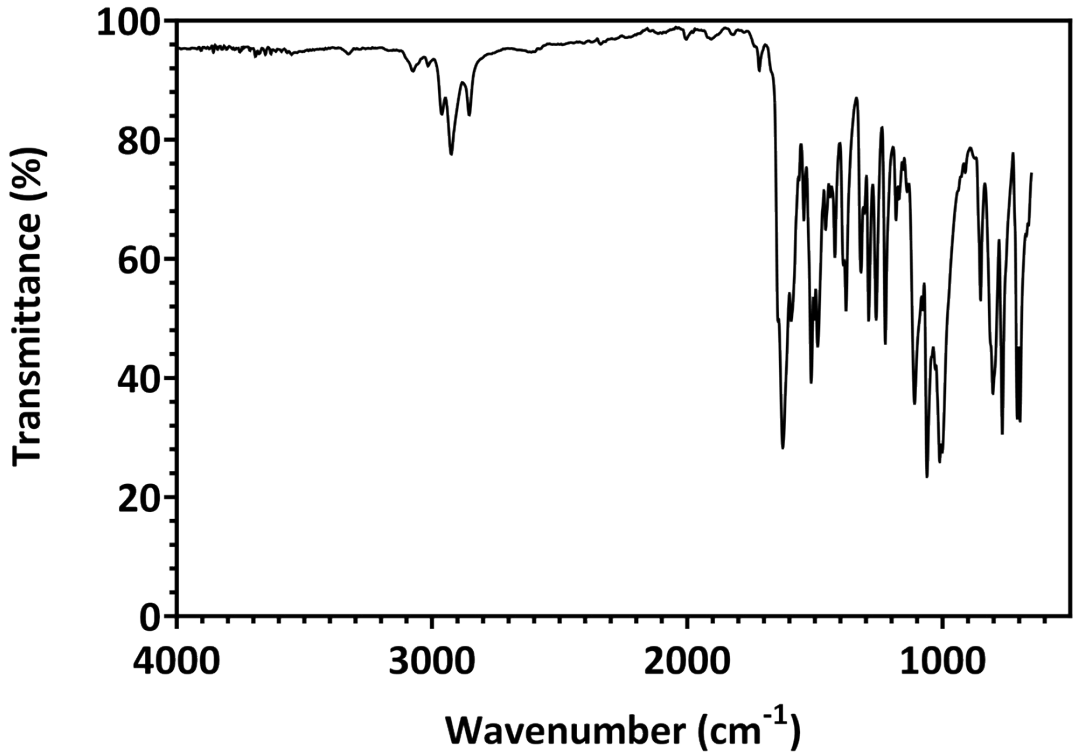

Figure S65. FT-IR spectrum of **2a**.

S18: References

1. J. Gamboa Varela, A. De Chatterjee, P. Guevara, V. Ramirez, A. J. Metta-Magaña, D. Villagrán, A. Varela-Ramirez, S. Das and J. E. Nuñez, *J. Biol. Inorg. Chem.*, 2014, **19**, 967-979.
2. P. W. McDonald and C. Ritchie, *Chem. Commun.*, 2024, **60**, 3051-3054.
3. CrysAlisPRO, Oxford Diffraction /Agilent Technologies UK Ltd, Yarnton, England.
4. O. V. Dolomanov, L. J. Bourhis, R. J. Gildea, J. A. K. Howard and H. Puschmann, *J. Appl. Crystallogr.*, 2009, **42**, 339-341.
5. P. Le Magueres, E. W. Reinheimer, M. Meyer, A. Jones and D. Kucharczyk, *Acta Crystallographica Section A*, 2018, **74**, a468.
6. G. Sheldrick, *Acta Crystallographica Section A*, 2015, **71**, 3-8.
7. G. Sheldrick, *Acta Crystallographica Section C*, 2015, **71**, 3-8.
8. L. Merrill and W. A. Bassett, *Review of Scientific Instruments*, 1974, **45**, 290-294.
9. S. A. Moggach, D. R. Allan, S. Parsons and J. E. Warren, *J. Appl. Crystallogr.*, 2008, **41**, 249-251.
10. G. J. Piermarini, S. Block, J. D. Barnett and R. A. Forman, *Journal of Applied Physics*, 1975, **46**, 2774-2780.
11. G. M. Sheldrick, *Journal*, 1996.
12. R. P. Cox, H. F. Higginbotham, B. A. Graystone, S. Sandanayake, S. J. Langford and T. D. M. Bell, *Chem. Phys. Lett.*, 2012, **521**, 59-63.
13. P. R. Spackman, M. J. Turner, J. J. McKinnon, S. K. Wolff, D. J. Grimwood, D. Jayatilaka and M. A. Spackman, *J. Appl. Crystallogr.*, 2021, **54**, 1006-1011.
14. C. F. Mackenzie, P. R. Spackman, D. Jayatilaka and M. A. Spackman, *IUCrJ*, 2017, **4**, 575-587.
15. M. J. Frisch, G. W. Trucks, H. B. Schlegel, G. E. Scuseria, M. A. Robb, J. R. Cheeseman, G. Scalmani, V. Barone, G. A. Petersson, X. L. H. Nakatsuji, M. Caricato, A. V. Marenich, J. Bloino, B. G. Janesko, R. Gomperts, B. Mennucci, H. P. Hratchian, J. V. Ortiz, A. F. Izmaylov, J. L. Sonnenberg, D. Williams-Young, F. Ding, F. Lipparini, F. Egidi, J. Goings, B. Peng, A. Petrone, T. Henderson, D. Ranasinghe, V. G. Zakrzewski, J. Gao, N. Rega, G. Zheng, W. Liang, M. Hada, M. Ehara, K. Toyota, R. Fukuda, J. Hasegawa, M. Ishida, T. Nakajima, Y. Honda, O. Kitao, H. Nakai, T. Vreven, K. Throssell, J. A. Montgomery, Jr., J. E. Peralta, F. Ogliaro, M. J. Bearpark, J. J. Heyd, E. N. Brothers, K. N. Kudin, V. N. Staroverov, T. A. Keith, R. Kobayashi, J. Normand, K. Raghavachari, A. P. Rendell, J. C. Burant, S. S. Iyengar, J. Tomasi, M. Cossi, M., J. M. Millam, M. Klene, C. Adamo, R. Cammi, J. W. Ochterski, R. L. Martin, K. Morokuma, O. Farkas, J. B. Foresman and D. J. Fox, 2016.
16. J.-D. Chai and M. Head-Gordon, *J. Chem. Phys.*, 2008, **128**, 084106.
17. L. Goerigk and S. Grimme, *J. Chem. Phys.*, 2010, **132**, 184103; M. Casanova-Páez and L. Goerigk, *J. Chem. Phys.*, 2020, **153**, 064106.
18. F. Weigend and R. Ahlrichs, *Phys. Chem. Chem. Phys.*, 2005, **7**, 3297-3305.